Summer 2015

Reliability-based design optimization of composite wind turbine blades for fatigue life under wind load uncertainty

Weifei Hu
University of Iowa

RELIABILITY-BASED DESIGN OPTIMIZATION OF COMPOSITE WIND TURBINE BLADES FOR FATIGUE LIFE UNDER WIND LOAD UNCERTAINTY

by

Weifei Hu

A thesis submitted in partial fulfillment
of the requirements for the Doctor of
Philosophy degree in Mechanical Engineering
in the Graduate College of
The University of Iowa

August 2015

Thesis Supervisors: Professor Kyung K. Choi
Associate Professor Olesya I. Zhupanska
Assistant Professor James H.J. Buchholz

Graduate College
The University of Iowa
Iowa City, Iowa

CERTIFICATE OF APPROVAL

PH.D. THESIS

This is to certify that the Ph.D. thesis of

Weifei Hu

has been approved by the Examining Committee
for the thesis requirement for the Doctor of Philosophy
degree in Mechanical Engineering at the August 2015 graduation.

Thesis Committee:

Kyung K. Choi, Thesis Supervisor

Olesya I. Zhupanska, Thesis Supervisor

James H.J. Buchholz, Thesis Supervisor

Patrick B. Butler

Pablo M. Carrica

Ganesh Rajagopalan

Hiroyuki Sugiyama

ACKNOWLEDGMENTS

The broad scope of this study could not have been well integrated into this thesis without scientific supervision from my three advisors. I would like to first thank my advisor, Professor Kyung K. Choi, who has taught me not only the state-of-the-art reliability theories, but also how to dig out problems and find the best solution. His rigorous research attitude, high academic requirements, and continuous inspiration have guided me in my Ph.D. pursuit. I also would like to thank my co-advisors, Professor Olesya I. Zhupanska and Professor James H.J. Buchholz, for their constant encouragement and advice in composite material and wind turbine aerodynamics, respectively.

Special thanks to my previous and current colleagues. As my senior and good friend, Dr. Hyunkyoo Cho provided so much help by sharing his great ideas for my research. Dr. Nicholas Gaul kindly helped with software development and many fruitful discussions. Dr. Ed Hardee shared his expertise in mechanical structural analysis. Dr. Ikjin Lee and Dr. Liang Zhao gave me many good suggestions in the early stages of my research. I had a very good time working with Ms. Minyeong Moon and Mr. Sangjune Bae in the same group. Ms. Deborah Hampton and Ms. Jenny Simpson provided enormous help in my research life at CCAD. Ms. Melanie Laverman helped edit many of my papers as well as this thesis.

The examination committee members are greatly thanked for their dedication to the examination of the thesis.

This research is primarily supported by the Iowa Alliance Wind Innovation and Novel Development (IAWIND) 09-IPF-15 and NSF EPSCoR project EPS-1101284. These supports are greatly appreciated.

Finally I want to deeply thank my parents, sister, and Tingting, who are always giving me support and love.

ABSTRACT

The objectives of this study are (1) to develop an accurate and efficient fatigue analysis procedure that can be used in reliability analysis and reliability-based design optimization (RBDO) of composite wind turbine blades; (2) to develop a wind load uncertainty model that provides realistic uncertain wind load for the reliability analysis and the RBDO process; and (3) to obtain an optimal composite wind turbine blade that satisfies target reliability for durability under the uncertain wind load. The current research effort involves: (1) developing an aerodynamic analysis method that can effectively calculate detailed wind pressure on the blade surface for stress analysis; (2) developing a fatigue failure criterion that can cope with non-proportional multi-axial stress states in composite wind turbine blades; (3) developing a wind load uncertainty model that represents realistic uncertain wind load for fatigue reliability of wind turbine systems; (4) applying the wind load uncertainty model into a composite wind turbine blade and obtaining an RBDO optimum design that satisfies a target probability of failure for a lifespan of 20 years under wind load uncertainty.

In blade fatigue analysis, resultant aerodynamic forces are usually applied at the aerodynamic centers of the airfoils of a blade to calculate stress/strain. However, in reality the wind pressures are applied on the blade surface. A wind turbine blade is often treated as a typical beam-like structure for which fatigue life calculations are limited in the edge-wise and/or flap-wise direction(s). Using the beam-like structure, existing fatigue analysis methods for composite wind turbine blades cannot cope with the non-proportional multi-axial stress states that are endured by wind turbine blades during operation. Therefore, it is desirable to develop a fatigue analysis procedure that utilizes detailed wind pressures as wind loads and considers non-proportional multi-axial stress states in fatigue damage calculation. In this study, a 10-minute wind field realization, determined by a 10-minute mean wind speed V_{10} and a 10-minute turbulence intensity I_{10}, is first simulated using Veers' method. The simulated wind field is used for aerodynamic

analysis. An aerodynamic analysis method, which could efficiently generate detailed quasi-physical blade surface pressures, has been developed. The generated pressures are then applied on a high-fidelity 3-D finite element blade model for stress and fatigue analysis. The fatigue damage calculation considers the non-proportional multi-axial complex stress states. A detailed fatigue damage contour, which indicates the fatigue failure locally, can be obtained using the developed fatigue analysis procedure. As the 10-minute fatigue analysis procedure is deterministic in this study, the calculated 10-minute fatigue damage is determined by V_{10} and I_{10}. It is necessary to clarify that the rotational speed of the wind turbine blade is assumed to be constant (12.1 rpm) and the pitch angle is fixed to be 0 degree for different wind conditions, since the rotational speed control and pitch angle control have not been considered in this study.

For predicting the fatigue life of a wind turbine, a fixed Weibull distribution is widely used to determine the percentage of time the wind turbine experiences different mean wind speeds during its life-cycle. Meanwhile, fixed turbulence intensities are often used based on the designed wind turbine types. These simplifications, i.e., fixed Weibull distribution and fixed turbulence intensities, ignore the realistic uncertain wind load when designing a reliable wind turbine system. In the real world, both the mean wind speed and turbulence intensity vary constantly over one year, and their annual distributions are different at different locations and in different years. Thus, it is necessary to develop a wind load uncertainty model that can provide a realistic uncertain wind load for designing reliable wind turbine systems. In this study, 249 groups of measured wind data, collected at different locations and in different years, are used to develop a dynamic wind load uncertainty model. The dynamic wind load uncertainty model consists of annual wind load variation and wind load variation in a large spatiotemporal range, i.e., at different locations and in different years. The annual wind load variation is represented by the joint probability density function of V_{10} and I_{10}. The wind load variation in a large spatiotemporal range is represented by the probability density functions of five

parameters, C, k, a, b, and τ, which determine the joint probability density function of V_{10} and I_{10}.

In order to obtain the RBDO optimum design efficiently, a deterministic design optimization (DDO) procedure of a composite wind turbine blade has been first carried out using averaged percentage of time (probability) for each wind condition. A wind condition is specified by two terms: 10-minute mean wind speed and 10-minute turbulence intensity. In this research, a probability table, which consists of averaged probabilities corresponding to different wind conditions, is referred as a mean wind load. The mean wind load is generated using the dynamic wind load uncertainty model. During the DDO process, the laminate thickness design variables are tailored to minimize the total cost of composite materials while satisfying the target fatigue lifespan of 20 years. It is found that, under the mean wind load condition, the fatigue life of the initial design is only 0.0004 year. After the DDO process, even though the cost at the DDO optimum design is increased by 31.5% compared to that at the initial design, the predicted fatigue life at the DDO optimum design is significantly increased to 19.9995 years. Reliability analyses of the initial design and the DDO optimum design have been carried out using the wind load uncertainty model and Monte Carlo simulation. The reliability analysis results show that the DDO procedure reduces the probability of failure from 100% at the initial design to 49.9% at the DDO optimum design considering only wind load uncertainty. In order to satisfy the target 2.275% probability of failure, it is necessary to further improve the fatigue reliability of the composite wind turbine blade by RBDO.

Reliability-based design optimization of the composite wind turbine blade has been carried out starting at the DDO optimum design. Fatigue hotspots for RBDO are identified among the laminate section points, which are selected from the DDO optimum design. Local surrogate models for 10-minute fatigue damage have been created at the selected hotspots. Using the local surrogate models, both the wind load uncertainty and manufacturing variability has been included in the RBDO process. It is found that the

probability of failure is 50.06% at the RBDO initial design (DDO optimum design) considering both wind load uncertainty and manufacturing variability. During the RBDO process, the normalized laminate thickness design variables are tailored to minimize the total cost of composite materials while satisfying the target 2.275% probability of failure. The obtained RBDO optimum design reduces the probability of failure from 50.06% at the DDO optimum design to 2.28%, while increasing the cost by 3.01%.

PUBLIC ABSTRACT

This research aims to design fatigue-reliable and cost-effective composite wind turbine blades to reduce the cost of wind energy. In order to achieve this goal, several challenges have been taken on, including development of an accurate fatigue analysis procedure, development of a realistic wind load uncertainty model, and development of an optimum blade design that minimizes cost and satisfies the reliability requirement under uncertain wind load.

The fatigue analysis procedure developed in this research calculates the detailed 10-minute fatigue damage of a composite wind turbine blade under a wind condition that is specified by two terms: 10-minute mean wind speed and 10-minute turbulence intensity. The former is an average wind speed, and the latter represents wind speed fluctuation over a period of 10 minutes.

To calculate fatigue damage in the long term, a joint distribution of the 10-minute mean wind speed and the 10-minute turbulence intensity is used to account for the variable wind load over one year. Furthermore, a wind load uncertainty model is developed to account for annual wind load variation and wind load variation during different years and at different locations.

Using the wind load uncertainty model, a reliability analysis method considering wind load certainty is developed. In order to design a blade for a 20-year fatigue life, a deterministic design optimization procedure without considering wind load uncertainty is first developed. Reliability-based design optimization is then implemented to further reduce the probability of fatigue failure considering wind load uncertainty. Finally, the optimum blade design is obtained.

TABLE OF CONTENTS

LIST OF TABLES

LIST OF FIGURES

LIST OF ABBREVIATIONS AND SYMBOLS

a	Shape Parameter of Gamma Distribution
a	Random Vector Containing 20 Random Variables a
ASTM	American Society for Testing and Materials
b	Scale Parameter of Gamma Distribution
b	Random Vector Containing 20 Random Variables b
BEM	Blade Element Momentum
$c(u,v;\theta)$	Copula Density Function
c^{QQ1}	Coefficient of Variation of Composite Material QQ1
c^{P2B}	Coefficient of Variation of Composite Material P2B
C	Scale Parameter of Weibull Distribution
C	Random Vector Containing 20 Random Variables C
$C(\mathbf{d})$	Normalized Total Cost of Composite Materials at a Design **d** in DDO
$C(\boldsymbol{\mu})$	Normalized Total Cost of Composite Materials at a Design **μ** in RBDO
C_p	Original Wind Pressure Coefficient
C_p^*	Modified Wind Pressure Coefficient
C_l	Life Force Coefficient
C_d	Drag Force Coefficient
C_m	Moment Force Coefficient
Coh	Coherence Function
CoV	Coefficient of Variation
CDF	Cumulative Distribution Function
CFD	Computational Fluid Dynamics
CLD	Constant Life Diagram
$Cost^0$	Initial Cost of Composite Materials
$Cost^{DDO}$	Composite Material Cost of the DDO Optimum Design
d_i	ith Design Variable in DDO

d_i^0	Initial Value of *i*th Design Variable
d	Design Vector
$\mathbf{d}^L$	Lower Bound of Design Variable Vector **d**
$\mathbf{d}^U$	Upper Bound of Design Variable Vector **d**
D_{10}	10-Minute Fatigue Damage
$D_{10}^{i,j}$	10-Minute Fatigue Damage Corresponding to (i, j) Wind Condition
D_{1year}	One-Year Fatigue Damage
D_{20year}	Twenty-Year Fatigue Damage
DDO	Deterministic Design Optimization
DoE	Design of Experiment
DOE	U.S. Department of Energy
DRM	Dimension Reduction Method
E_1	Longitudinal Young's Modulus
E_2	Transversal Young's Modulus
f_{I10}	Probability Density Function of 10-Minute Turbulence Intensity
f_{V10}	Probability Density Function of 10-Minute Mean Wind Speed
$f_{\Sigma 10}$	Probability Density Function of 10-Minute Standard Deviation of Wind Speed
f_{VI}	Joint Probability Density Function of 10-Minute Mean Wind Speed and 10-Minute Turbulence Intensity
$f_{\mathbf{X}}(\mathbf{x})$	Probability Density Function of a Random Vector **X**
$F_{Xi}(x_i)$	Cumulative Distribution Function of X_i
FAST	Fatigue, Aerodynamics, Structures, and Turbulence
FE	Finite Element
FEA	Finite Element Analysis
FORM	First-Order Reliability Method
$G(\mathbf{X})$	(Deterministic) Performance Measure

HAWT	Horizontal Axis Wind Turbine
i_{10}	10-Minute Turbulence Intensity (Realization)
I_{10}	10-Minute Turbulence Intensity (Random Variable)
I_{low}	Lower Bound of 10-Minute Turbulence Intensity
I_{upp}	Upper Bound of 10-Minute Turbulence Intensity
$I_{\Omega_F}(\cdot)$	Indicator Function
I-RBDO	Iowa Reliability-Based Design Optimization (Code)
IEC	International Electrotechnical Commission
k	Shape Parameter of Weibull Distribution
$\mathbf{k}$	Random Vector Containing 20 Random Variables k
l	Natural Logarithm of Likelihood Function
L	Likelihood Function
m_i	Mass of Panel(s) Linked to *i*th Design Variable in DDO
m_i^0	Initial Mass of Panel(s) Linked to *i*th Design Variable in DDO
M_i^0	Mass of *i*th Part at the RBDO Initial Design
MCS	Monte Carlo Simulation
MLE	Maximum Likelihood Estimate
MPP	Most Probable Point
MSU	Montana State University
N_{ij}	Number of Allowable Cycle
NACA	National Advisory Committee for Aeronautics
NC	Number of Constraints
NDV	Number of Design Variables
$NMCS$	Number of Monte Carlo Simulation Samples
NREL	National Renewable Energy Laboratory
NRMSE	Normalized Root Mean Square Error
P_F	Probability of Failure = Reliability Output

P_F^{Tar}	Target Probability of Failure, Target Reliability Output
P_k	Dynamic Wind Pressure at *k*th Blade Section
$P_{VI}^{i,j}$	Probability Value Corresponding to (*i*, *j*) Wind Condition
$\bar{P}_{VI}^{i,j}$	Mean Probability Value Corresponding to (*i*, *j*) Wind Condition
PDF	Probability Density Function
PMA	Performance Measure Approach
PSD	Power Spectral Density
R	Stress Ratio
RBDO	Reliability-Based Design Optimization
RIA	Reliability Index Approach
RMS	Root Mean Square
$s_{\mu_i}^{(1)}$	First-Order Score Function
S	Power Spectral Density Function or Shear Strength
S	Power Spectral Density Matrix
SNL	Sandia National Laboratories
SORM	Second-Order Reliability Method
SQP	Sequential Quadratic Programming
t_i	Realization of Laminate Thickness Random Variable
T_i	Laminate Thickness Random Variable
U-Space	Independent Standard Normal Space
v_{10}	10-Mintue Mean Wind Speed (Realization)
V_{10}	10-Minute Mean Wind Speed (Random Variable)
V_{hub}	Hub Height Wind Speed
V_{low}	Lower Bound of 10-Minute Mean Wind Speed
V_{upp}	Upper Bound of 10-Minute Mean Wind Speed
x	Realization of Random Vector **X**
X	Random Vector

X	Random Variable
X_T	Longitudinal Tensile Strength
X_C	Longitudinal Compressive Strength
Y_T	Transversal Tensile Strength
Y_C	Transversal Compressive Strength
γ	Log-Location Parameter of Log-Logistic Distribution
δ	Log-Scale Parameter of Log-Logistic Distribution
θ	Correlation Coefficient for Copula
μ	Mean of Random Variable
$\boldsymbol{\mu}$	Mean of Random Vector
ν_{12}	Poisson's Ratio
ρ	Density
σ_{ij}	Stress Component
σ_{10}	10-Minute Standard Deviation of Wind Speed (Realization)
σ	Standard Deviation
Σ_{10}	10-Minute Standard Deviation of Wind Speed (Random Variable)
τ	Kendall's Tau of Correlated Random Variables
$\boldsymbol{\tau}$	Random Vector Containing 20 Random Variables τ
Ω_F	Failure Domain

CHAPTER 1

INTRODUCTION

This study presents new methods in reliability-based design optimization (RBDO) of composite wind turbine blades for fatigue life under wind load uncertainty. First, a 10-minute fatigue analysis procedure, which includes wind field simulation, aerodynamic analysis, stress analysis using finite element analysis (FEA), and fatigue damage evaluation based on fatigue test data, is developed. In the 10-minute fatigue analysis procedure, the simulated wind field is determined by a 10-minute mean wind speed and a 10-minute turbulence intensity. The simulated wind field is used in the aerodynamic analysis, which efficiently calculates wind pressure on a wind turbine blade surface for FEA. Through FEA, the wind pressure results in non-proportional multi-axial complex stress states in the wind turbine blade, which has been considered in the 10-minute fatigue analysis. The result of the 10-minute fatigue analysis, the 10-minute fatigue damage, is a deterministic function of the 10-minute mean wind speed and the 10-minute turbulence intensity. In order to investigate the reliability analysis and RBDO of composite wind turbine blades for a designed lifespan, e.g., 20 years, it is necessary to consider an uncertain wind load. Thus, a dynamic wind load uncertainty model is developed to take account of annual wind load variation and wind load variation in a large spatiotemporal range, i.e., in different years and at different locations. Based on the developed wind load uncertainty model, a mean wind load is generated and applied in the deterministic design optimization (DDO) of a composite wind turbine blade. Assuming the mean wind load continues for 20 years, the DDO optimum design satisfies the constraint of the 20-year fatigue lifespan. However, the reliability analysis results of the DDO optimum design under the wind load uncertainty show that the probability of fatigue failure is around 50%, which does not satisfy the target reliability requirement. Thus, starting at the DDO optimum design, RBDO of the composite wind turbine blade is

then carried out to design a cost-effective wind turbine blade, which satisfies the target reliability requirement.

In Section 1.1, the background and motivation of this study are presented. Section 1.2 provides the objectives of the proposed research, and Section 1.3 describes the organization of this thesis.

1.1 Background and Motivation

1.1.1 Reliability-Based Design Optimization

Reliability-based design optimization has been well developed to obtain reliable and cost-effective designs of many engineering problems under various uncertainties. One of the applications is RBDO of fatigue-sensitive structures for which engineers would like to evaluate an accurate fatigue lifespan. By applying RBDO to the fatigue-sensitive structures, their design could then be fine-tuned to reduce needless costs while satisfying the target reliability of fatigue performance. Therefore, as an expensive component in large wind turbine systems, designing fatigue-reliable wind turbine blades is one of the most necessary tasks in wind energy business. A cost-effective design of the blades reduces the initial investment, while a fatigue-reliable design saves maintenance cost of the wind turbine systems. Hence, RBDO can achieve both the reduction of initial investment and maintenance cost.

Reliability-based design optimization is an optimization method based on reliability analysis. In each design iteration, RBDO requires reliability analysis of performance measures. Reliability analysis methods can be classified into two groups: (1) sensitivity-based methods and (2) sampling-based methods. The representative sensitivity-based methods include the first-order reliability method (FORM) (Hasofer and Lind, 1974; Tu *et al.*, 1999; Haldar and Mahadevan, 2000; Tu *et al.*, 2001), the second-order reliability method (SORM) (Hohenbichler and Rackwitz, 1988; Breitung, 1984), and the dimension reduction method (DRM) (Rahman and Wei, 2006; Lee *et al.*, 2010).

The FORM and SORM approximate a performance measure at the most probable point (MPP) using first- and second-order Taylor series expansion, respectively, and the DRM approximates a multi-dimensional performance function with a sum of lower-dimensional functions to calculate the probability of failure. In order to find the MPP, the sensitivity (gradient) of performance function needs to be calculated. However, for many engineering applications, e.g., fatigue of wind turbine blades, accurate sensitivities of performance functions are not available. Therefore, in such applications, the sensitivity-based methods, which require the sensitivities of performance functions to find the MPP, cannot be directly used. On the other hand, the sampling-based methods do not require the sensitivity of performance function to calculate the probability of failure. Instead, the sampling-based methods directly calculate the probability of failure using Monte Carlo simulation (MCS). However, the sampling-based methods could be computationally inefficient because the MCS may require thousands of analyses of a performance function.

According to the reliability analysis methods, RBDO can be performed using sensitivity-based reliability analysis and sampling-based reliability analysis. Common sensitivity-based RBDO methods incorporate probabilistic constraints that can be evaluated using (1) the reliability index approach (RIA) and (2) the performance measure approach (PMA). The MPP in the RIA represents the probability of failure at the current design, while the MPP in the PMA represents the target probability of failure (Tu *et al.*, 1999). Both sensitivity-based RBDO methods require the design sensitivity of a probabilistic constraint at the MPP. The design sensitivities of probabilistic constraints require the sensitivity of the corresponding performance functions. Thus, the disadvantage of sensitivity-based reliability analysis methods, i.e., requiring sensitivity of performance function, still exists in the sensitivity-based RBDO methods. In order to handle complicated engineering problems, e.g., fatigue reliability of composite wind turbine blades, sampling-based RBDO methods are more appropriate because they do not

require sensitivity of performance measure. Moreover, the design sensitivity of probabilistic constraints has been developed for sampling-based RBDO without requiring sensitivity of performance measure (Lee *et al.*, 2011a; Lee *et al.*, 2011b). Due to the expense of MCS, which is used to estimate the probability of failure in sampling-based RBDO, surrogate models are often used to reduce computational cost. A challenge when using sampling-based RBDO in this study is developing an accurate surrogate model to replace complicated, nonlinear, and implicit fatigue damage analysis.

1.1.2 Fatigue Analysis of Composite Wind Turbine Blades

As the rated power of horizontal axis wind turbines (HAWT) increases into multi-MW-size, both the initial investment and future maintenance cost of wind turbines increase significantly. Thus, it is of critical importance to design a reliable and cost-effective blade, which is a key component of the wind turbine system, to sustain its mission for a lifespan of 20 years. Therefore, RBDO of modern composite wind turbine blades against fatigue failure becomes one of the challenging topics in wind energy nowadays. However, appropriate RBDO cannot be performed if it is not accompanied with an accurate fatigue analysis method for composite wind turbine blades.

Fatigue analysis of composite wind turbine blades basically includes fatigue load calculation, blade stress/strain analysis, and composite fatigue analysis. The actual loads applied on a wind turbine consist of gravitational load; aerodynamic loads; inertia loads, including centrifugal and gyroscopic effects; and operational loads due to braking, yawing, blade pitch control, etc. Among these loads, the aerodynamic loads have a significant influence on fatigue of the wind turbine blade because it is the aerodynamic loads that drive the wind turbine to function over the entire lifespan.

The current approaches for wind turbine aerodynamics include the simple blade element momentum (BEM) method, intermediate complex theories such as the vortex and panel methods, and the computational fluid dynamics (CFD) method (Hansen *et al.*,

2006; Li *et al.*, 2012; Li *et al.*, 2015). The BEM method is currently a very common tool to achieve rapid simulations for the standard sets of calculations; thus, it is widely used in both academia and industry (Moriarty and Hansen, 2005). Grujicic *et al.* calculated the wind pressure by a 2-D aerodynamic analysis code, which solves the flow equations over an airfoil by implementing the boundary integral method, and directly applied the calculated wind pressure in the quasi-static structural analysis of a finite element (FE) blade model (Grujicic *et al.*, 2010). However, the wind pressure calculated by Grujicic *et al.* did not consider the rotational effect of the wind turbine rotor. Griffith and Ashwill first calculated resultant aerodynamic forces at the aerodynamic centers using NREL's FAST (Jonkman and Buhl, 2005) and then applied the aerodynamic forces to nodes near aerodynamic centers in the FE model (Griffith and Ashwill, 2011). This strategy easily connects the aerodynamic forces and FE model; however, it is not clear how best to transform loads from the aerodynamic centers to the structure of a 3-D blade. The CFD could calculate the detailed wind pressure along the blade surface. However, computational time for CFD is a significant hurdle that prevents CFD from being used in stochastic design calculations. In this study, an aerodynamic analysis method, which could efficiently generate detailed quasi-physical blade surface pressures, has been developed.

For blade stress/strain analysis, a composite wind turbine blade is often treated as a typical beam-like structure (Griffith and Ashwill, 2011; Ronold *et al.*, 1999; Ronold and Christensen, 2001; Kong *et al.*, 2005; Kong *et al.*, 2006). From simple beam theory, explicit equations have been applied to calculate the stress/strain of wind turbine blades as a function of wind loads. For example, Fossum *et al.* calculated the normal strain as a function of flapwise and edgewise bending moments and axial force (Fossum *et al.*, 2013). Winterstein and Veers described fatigue stress in terms of the root mean square (RMS) of the instantaneous stress, which was assumed to be an exponential function of wind speed (Winterstein and Veers, 2000). Ronold *et al.* calculated the stress range at the

root as a ratio between moment range and section modulus, while the moment range was calculated as a function of 10-minute mean wind speed and other parameters (Ronold *et al.*, 1999; Ronold *et al.*, 2001). Instead of predicting the fatigue life directly, Kong *et al.* (Kong *et al.*, 2005; Kong *et al.*, 2006) evaluated whether or not the fatigue life requirement was satisfied by comparing the calculated maximum stress and the allowable fatigue stress using Spera's empirical equation (Spera, 1998). Experimentally measured wind loads have also been used in the blade structural analysis (Ragan and Manuel, 2007; Veers and Winterstein, 1997). One S-N curve was applied to calculate fatigue life in the edge-wise and flap-wise directions of the blade (Griffith and Ashwill, 2011). Even though the computational time of the above methods is small, there are three shortcomings:

(1) The fatigue damage/life may not be investigated at a specific location on the wind turbine blade. The detailed fatigue damage/life contour of the blade may not be obtainable.

(2) It needs to obtain stress/moment measurements to validate or generate the functional forms, or to fit a regression model. Thus, it is not appropriate for the early stages of blade design, since those measured data are usually not available.

(3) Only limited S-N curves were used to calculate the allowable number of fatigue loads. Thus, the multi-axial complex stress states of the blade under complex loading conditions may not be considered in the fatigue analysis.

In contrast, a full 3-D FE model could provide detailed fatigue analysis and indicate the fatigue failure at a specific location on the wind turbine blade. With the ever-increasing computational capability, full-scale blade modeling for stress/strain analysis has become a trend in the design, manufacture, and evaluation of wind turbine blades (Veers *et al.*, 2003). Previous research has emphasized the necessity for improved and detailed fatigue life modeling for reliable and optimal blade design (OPTIMAT BLADES, 2006; Mishnaevsky *et al.*, 2012).

Using the obtained stress/strain of wind turbine blades, the composite fatigue analysis is carried out to evaluate the fatigue damage. Due to the complex and variable loading conditions, composite wind turbine blades bear non-proportional multi-axial complex stress states of variable amplitude and mean. Multi-axial fatigue failure criteria have been developed to take multi-axial fatigue into account for composite materials (Hashin and Rotem, 1973; Fujii and Lin, 1995; Philippidis and Vassilopoulos, 2002; Philippidis and Vassilopoulos, 2004; Vassilopoulos and Keller, 2011; Sun *et al.*, 2012; Puck *et al.*, 2002; Wei and Forte, 2010). However, most of the existing methods in the literature concentrate mainly on the introduction and validation of fatigue failure criteria suitable for constant-amplitude multi-axial proportional stress fields without addressing the problem of life prediction under irregular load spectra. In addition, limited experimental data and design guidelines addressing the complex stress state effect on the fatigue behavior of composite materials are available for non-proportional multi-axial loading. Harris stated that although there were techniques to cope with non-proportional multi-axial fatigue in metallic materials, no such theoretical or experimental studies were available for anisotropic composite materials (Harris, 2003). Liu and Mahadevan proposed a unified multi-axial fatigue damage model for isotropic and anisotropic materials and validated the model under proportional multi-axial stress within composite laminates (Liu and Mahadevan, 2007). In the absence of techniques that could solve non-proportional multi-axial complex stress efficiently, composite wind turbine blades are treated by state-of-the-art design codes (e.g., IEC, 2005; Germanischer Lloyd, 2010), as a typical beam-like structure in which fatigue life calculations are limited in considering the normal stress component in the beam axis direction (Griffith and Ashwill, 2011; Ronold *et al.*, 1999; Jonkman and Buhl, 2005; Ronold and Christensen, 2001; Fossum *et al.*, 2013; Vassilopoulos, 2010). However, the transverse and shear stresses in the wind turbine blade should be considered because their great influence on fatigue damage/life

has been demonstrated in off-axis loading of glass fiber composites, which have proportional stress components (Philippidis and Vassilopoulos, 2002).

1.1.3 Wind Load Uncertainty

It is difficult to accurately predict reliability for the fatigue damage/life of composite wind turbine blades due to various uncertainties from material properties, the manufacturing process, and external loads. Among those uncertainties, wind load uncertainty is the most significant source of uncertainty affecting the fatigue reliability of wind turbine blades. Hence, a better understanding of the wind load uncertainty could facilitate the design of wind turbine blades that are more reliable than those designed without correctly considering the wind load uncertainty.

In order to consider the wind load uncertainty, partial safety factors have been introduced in wind turbine standards (IEC, 2005; Germanischer Lloyd, 2010). Researchers applied the partial safety factors on wind load for design of wind turbine blades (Ronold *et al.*, 1999; Ronold and Christensen, 2001; Kong *et al.*, 2005; Kong *et al.*, 2006). Although using the partial safety factors to account for the wind load uncertainty is convenient, the spatial and temporal wind load variation cannot be represented accurately. Another disadvantage of using the partial safety is that the produced design may be too conservative if unnecessary large safety factors are used.

A number of studies have also applied probabilistic models for mean wind speed to characterize the annual wind load variation (Ronold *et al.*, 1999; Ronold and Christensen, 2001; Shokrieh and Rafiee; 2006; Griffith and Ashwill, 2011; Manwell *et al.*, 2009; Burton *et al.*, 2001; Manuel *et al.*, 2001; Messac *et al.*, 2011; Carta *et al.*, 2009). One of the most widely used models is the two-parameter Weibull distribution, which is based on annual wind speed data. This distribution has been used to determine the percentage of time that the wind turbine experiences different mean wind speeds during its life cycle. Using this time percentage, the wind load and corresponding fatigue

damage can then be calculated for each mean wind speed. By accumulating the fatigue damage for each mean speed, the total damage and the fatigue life can be calculated based on the damage rules. However, by applying a fixed Weibull distribution, only deterministic fatigue life can be obtained because the assumed Weibull distribution is constant in different years. The fixed Weibull distribution based either on wind turbine standards (IEC, 2005; Germanischer Lloyd, 2010) or measured wind data over one year at a specific location cannot truly render the wind load uncertainty over a larger spatiotemporal range, for instance at different locations and in different years.

Besides the mean wind speed, the fluctuations in the wind speed about the short-term mean naturally have a major impact on the design loadings, as they are the source of extreme gust loads and a large part of the blade fatigue loading (Burton *et al.*,2011; Manwell *et al.*, 2009). However, very few turbulence intensities are used in reliability analysis of wind turbines. Only three deterministic turbulence intensity levels are used to classify different wind turbine designs in the International Electrotechnical Commission (IEC) standard (IEC, 2005). Noda and Flay applied a single turbulence intensity when simulating the wind turbine blade fatigue damage in a typical New Zealand site, by which different sites are classified as either low- or high-intensity turbulence sites (Noda and Flay, 1999). In reality, the turbulence intensity should follow a certain distribution at a specific site. For example, Ronold *et al.* assumed the turbulence intensity followed a lognormal distribution (Ronold *et al.*, 1999). Consequently, in order to facilitate the fatigue design of a wind turbine blade surviving under realistic uncertain wind load, both variations of wind speed and turbulence intensity have to be involved. Hu *et al.* identified the distribution of 10-minute turbulence intensity to be a log-logistic distribution and applied both the distributions of 10-minute mean wind speed and 10-minute turbulence intensity in reliability analysis of wind turbine blades for fatigue life (Hu *et al.*, 2012a).

As the wind load varies over a large spatiotemporal range, the wind turbines are expected to survive the uncertain wind load at different locations and in different years.

However, this level of wind load uncertainty has not been found in existing research or wind energy standards (IEC, 2005; Germanischer Lloyd, 2010). Fixed distribution for mean wind speed is still widely applied for fatigue life prediction, which assumes that the same mean wind speed distribution continues for the entire lifespan.

In summary, the RBDO of composite wind turbine blades under wind load uncertainty should (1) accurately calculate fatigue damage under a wide range of wind conditions so that the following reliability analysis and RBDO procedure can be confidently carried out using the fatigue analysis procedure, (2) include a wind load uncertainty model that considers realistic uncertain wind load for fatigue reliability analysis and RBDO, (3) efficiently carry out reliability analysis under wind load uncertainty to estimate the probability of fatigue failure for a given design, and (4) use the advanced RBDO method to develop a composite wind turbine blade design that satisfies the target reliability requirement and minimizes the cost.

1.2 Objectives of the Proposed Study

The first objective of this study is to propose the fatigue analysis procedure, which includes wind fields simulation, aerodynamic analysis, stress analysis by finite element analysis (FEA), and fatigue damage evaluation based on tested fatigue data. Using the proposed fatigue analysis procedure, a 10-minute fatigue damage is determined by a 10-minute mean wind speed and 10-minute turbulence intensity. In this procedure, two key aspects have been specifically studied. One is efficiently generating quasi-physical blade surface pressures for subsequent stress and fatigue analysis. The other is considering non-proportional multi-axial complex stress states when calculating 10-minute fatigue damage.

The second objective of this study is to propose a wind load uncertainty model that represents realistic uncertain wind load for fatigue reliability of wind turbines. There are 249 groups of wind data used for developing the wind load uncertainty model. The

proposed wind load uncertainty model considers annual wind load variation and wind load variation in a large spatiotemporal range. The annual wind load variation is represented by the joint probability density function (PDF) of 10-minute mean wind speed and 10-minute turbulence intensity. To accurately generate this joint PDF, the marginal PDF types and copula types for 10-minute mean wind speed, 10-minute turbulence intensity, and 10-minute standard deviation of wind speed are studied based on measured wind data. The wind load variation in a large spatiotemporal range is represented by the PDFs of five random parameters C, k, a, b, and τ, which determine the joint PDF of 10-minute mean wind speed and 10-minute turbulence intensity. The proposed wind load uncertainty model can be used for reliability analysis and RBDO of wind turbine components, e.g., blade, rotor hub, gears, bearings, etc.

The third objective is to design an optimal composite wind turbine blade that satisfies target reliability for durability under the uncertain wind load. The proposed wind load uncertainty model is first used to generate a mean wind load for a DDO procedure of the blade model. The purpose of DDO is to obtain a DDO optimum design, which may provide a good initial design to RBDO, so that less computational effort would be required in the following RBDO procedure. Reliability analyses of the initial design and the DDO optimum design are then carried out under wind load uncertainty. The reliability analysis results show that the probability of fatigue failure is reduced from 100% at the initial design to 49.9% at the DDO optimum design considering only wind load uncertainty. In order to satisfy the target reliability requirement, the RBDO of the blade starting at the DDO optimum design is studied using the Iowa Reliability-Based Design Optimization (I-RBDO) code.

1.3 Organization of Thesis

Chapter 2 proposes a fatigue analysis procedure that calculates a 10-minute fatigue damage determined by a 10-minute mean wind speed and a 10-minute turbulence

intensity. The fatigue analysis procedure is used as a deterministic fatigue damage calculation procedure in DDO, reliability analysis, and RBDO.

Chapter 3 proposes a wind load uncertainty model, which has been developed based on measured wind data. The wind load uncertainty model consists of the annual wind load variation and the wind load variation in a large spatiotemporal range, for example, in different years and at different locations. The wind load uncertainty model is used to generate a mean wind load for DDO and provide uncertain wind load for reliability analysis and RBDO.

Chapter 4 presents a DDO procedure to optimize the cost of composite materials used in composite wind turbine blades. For DDO, the mean wind load is generated based on the wind load uncertainty model. The DDO of a composite wind turbine blade is carried out. A DDO optimum design satisfying a lifespan constraint of 20 years is obtained under the assumption that the mean wind load continues for 20 years.

Chapter 5 presents a reliability analysis method for a given blade design under wind load uncertainty. The reliability analysis uses MCS to account for the wind load uncertainty. The reliability analyses of the initial design and the DDO optimum design obtained in Chapter 4 have been carried out.

Chapter 6 describes the detailed procedure of RBDO of composite wind turbine blades considering wind load uncertainty and manufacturing variability. The RBDO procedure starts at the DDO optimum design and applies local surrogate models of 10-minute fatigue damage at each iteration and line search. An RBDO optimum design has been obtained to satisfy the target reliability requirement and minimize the cost.

Chapter 7 provides the conclusions of this study and recommendations for future research.

CHAPTER 2

FATIGUE ANALYSIS OF COMPOSITE WIND TURBINE BLADES

This chapter presents a fatigue analysis procedure that includes wind field simulation, aerodynamic analysis, stress analysis by finite element analysis (FEA), and fatigue damage evaluation based on tested fatigue data. In Section 2.1, the wind field simulation method is explained. An approach to calculate aerodynamic wind pressure for FEA is introduced in Section 2.2. Section 2.3 presents fatigue damage calculation of large composite wind turbine blades considering non-proportional multi-axial complex stress states. A high-fidelity finite element (FE) blade model is used in the fatigue analysis procedure.

2.1 Wind Field Simulation

State-of-the-art assessment of the fatigue damage of wind turbines concentrates on load cycles that are found within simulated or measured 10-minute period (Griffith and Ashwill, 2011; Burton *et al.*, 2011; Manwell and Mcgown, 2009, Grujicic *et al.*, 2010; Ragan and Manuel, 2007; Veers and Winterstein, 1997; Hu *et al.*, 2012a; Moriarty *et al.*, 2004; Hu *et al.*, 2013a; Söker and Kensche, 2004). In this Chapter, a 10-minute period is also considered as a basic time period for fatigue analysis. A 10-minute wind field is first generated based on 10-minute mean wind speed V_{10} and 10-minute turbulence intensity I_{10}. The 10-minute turbulence intensity is a measure of the turbulent severity of wind speed in 10 minutes. It is defined as the ratio of the standard deviation of wind speed to the mean of wind speed, determined from measured data of wind speed in 10 minutes (IEC 61400-1, 2005; Burton *et al.*, 2011; Manwell *et al.*, 2009) as

$$I_{10} = \frac{\Sigma_{10}}{V_{10}} \tag{2.1}$$

where Σ_{10} is the standard deviation of wind speed in 10 minutes.

The proposed fatigue analysis procedure utilizes Veers' method (Veers, 1988) to simulate a 3-D wind field with a prescribed power spectral density (PSD) function and a coherence function. In this study, the PSD function is a function of both V_{10} and I_{10}, and the coherence function is a function of V_{10}. Veers' method is based on a general random process simulation method developed by Shinozuka and Jan (Shinozuka and Jan, 1972). The basic approach of this method is to simulate wind speed time series at discrete points in a plane perpendicular to the mean wind direction and to propagate the time series in the mean wind direction at the mean wind speed. The basic algorithm is briefly given below (Veers, 1988; Hansen, 2008; Burton *et al.*, 2011).

The spectral properties of the wind speed fluctuations can be described by a spectral matrix **S**. If the number of points in space is *NP*, **S** is an *NP* × *NP* matrix. The diagonal terms S_{jj} in **S** represent the PSD at point *j*, *j* = 1, 2, …, *NP*. The off-diagonal terms in spectral matrix **S** can be defined in terms of the PSDs and the coherence function, Coh_{jk}, by

$$S_{jk}\left(f_m\right) = Coh_{jk}\left(f_m, \Delta r_{jk}, U_{jk}\right)\sqrt{S_{jj}\left(f_m\right)S_{kk}\left(f_m\right)} \tag{2.2}$$

where f_m is the center frequency of each discrete frequency band, *m* = 1, 2, …, *M* / 2, and *M* is number of discrete time moments in the simulated time series. The coherence, Coh_{jk}, is a function of frequency, f_m, distance between points *j* and *k*, Δr_{jk}, and mean wind speed at points *j* and *k*, U_{jk} . In this case, the spectral matrix **S** can be written as the product of a lower triangular matrix **H** (*NP* × *NP* matrix) and the transpose of its complex conjugate $\mathbf{H}^*$.

$$\mathbf{S}\left(f_m\right) = \mathbf{H}\left(f_m\right)\mathbf{H}^{*T}\left(f_m\right) \tag{2.3}$$

Because **S** is real, **H** must also be real, and **H**=**H***. The nonzero entries in **H** matrix can be computed through the following recursive formulae.

$$
\begin{aligned}
H_{11} &= S_{11}^{1/2} \\
H_{21} &= S_{21} / H_{11} \\
H_{22} &= \left(S_{22} - H_{21}^2 \right)^{1/2} \\
H_{31} &= S_{31} / H_{11} \\
&\vdots \\
H_{jk} &= \left(S_{jk} - \sum_{l=1}^{k-1} H_{jl} H_{kl} \right) / H_{kk} \\
H_{kk} &= \left(S_{kk} - \sum_{l=1}^{k-1} H_{kl}^2 \right)^{1/2}
\end{aligned}
\tag{2.4}
$$

The complex Fourier coefficients **v** (*NP* × 1 vector) are calculated by multiplying the weight matrix **H** with a white-noise vector **X** (*NP* × *NP* matrix). Each entry of **v** is calculated as

$$
v_j\left(f_m\right) = \sum_{k=1}^{j} H_{jk}\left(f_m\right) X_{kk}\left(f_m\right) = \sum_{k=1}^{j} H_{jk}\left(f_m\right) e^{i\theta_{km}} \tag{2.5}
$$

where $j = 1, 2, \ldots, NP$. The real and imaginary components of $v_j(f_m)$ are calculated as

$$
\begin{aligned}
\mathrm{Re}\left[v_j\left(f_m\right) \right] &= \sum_{k=1}^{j} H_{jk}\left(f_m\right) \cos\left(\theta_{km}\right) \\
\mathrm{Im}\left[v_j\left(f_m\right) \right] &= \sum_{k=1}^{j} H_{jk}\left(f_m\right) \sin\left(\theta_{km}\right)
\end{aligned}
\tag{2.6}
$$

which can be transformed to an amplitude $Amp_j(f_m)$ and a phase $\Phi_j(f_m)$ by

$$
\begin{aligned}
Amp_j\left(f_m\right) &= \sqrt{\mathrm{Re}\left[v_j\left(f_m\right) \right]^2 + \mathrm{Im}\left[v_j\left(f_m\right) \right]^2} \\
\tan \Phi_j\left(f_m\right) &= \frac{\mathrm{Im}\left[v_j\left(f_m\right) \right]}{\mathrm{Re}\left[v_j\left(f_m\right) \right]}
\end{aligned}
\tag{2.7}
$$

Finally, the time histories at the point *j* can be computed as

$$
U_j\left(t\right) = \bar{U} + 2\sum_{m=1}^{M/2} Amp_j\left(f_m\right) \cos\left[2\pi f_m t - \Phi_j\left(f_m\right) \right] \tag{2.8}
$$

where each discrete frequency is defined as $f_m = m / T$. T is the total simulation time, and m varies between 1 and $M / 2$, where M is the number of discrete time moments in the

simulated time series. The simulated wind field realizations in this study are generated by TurbSim (Jonkman, 2009a).

In conclusion, the simulated wind field realization is determined by a specific PSD function and a coherence function, which are functions of 10-minute mean wind speed V_{10} and 10-minute turbulence intensity I_{10}. Thus, essentially, the simulated wind field by the Veers' method is determined by V_{10} and I_{10}. Commonly used spectral models and spatial coherence models are list in Table 2.1 and Table 2.2, respectively (IEC 61400-1, 2005; Jonkman, 2009a). Table 2.1 provides explanation of symbols used in the IEC Kaimal Model, which has been applied in the wind field simulation in this study. For explanation of symbols used in other spectral models, please refer to the references (IEC 61400-1, 2005; Jonkman, 2009a). The coherence function for the IEC spectral model in TurbSim is selected as the coherence function in this study.

Table 2.1 Commonly Used Spectral Models

IEC Kaimal Model	$$S_K(f)=\frac{4\sigma_K^2 L_k/\overline{u}_{hub}}{\left(1+6fL_k/\overline{u}_{hub}\right)^{5/3}},\quad K=u,v,w$$ where f is the cyclic frequency; σ_K is the wind speed standard deviation in K direction; u, v, and w are wind speed in longitudinal, transverse, and vertical directions, respectively; $\bar{u}_{hub}$ is the mean wind speed at hub height. L_k is an integral scale parameter, which is determined by $$L_k=\begin{cases}8.10\Lambda_U, & K=u\\ 2.70\Lambda_U, & K=v\\ 0.66\Lambda_U, & K=w\end{cases}$$ where the turbulence scale parameter, $\Lambda_U = 0.7\cdot\min(60\ m, \text{hub height})$. The relationships between the standard deviations are defined to be $$\sigma_v=0.8\sigma_u$$ $$\sigma_w=0.5\sigma_u$$ The standard deviation in longitudinal direction is calculated as $$\sigma_u=V_{10}\cdot I_{10}$$
IEC Von Karman Isotropic Model	$$S_u(f)=\frac{4\sigma_u^2 L/\overline{u}_{hub}}{\left(1+71\left(fL/\overline{u}_{hub}\right)^2\right)^{5/6}}$$ $$S_K(f)=\frac{2\sigma_K^2 L/\overline{u}_{hub}}{\left(1+71\left(fL/\overline{u}_{hub}\right)^2\right)^{11/6}}\left(1+189\left(fL/\overline{u}_{hub}\right)^2\right),\quad \text{for } K=v,w$$
RisØ Smooth-Terrain Model	$$S_K(f)=UStar^2\frac{s_{1,K}\left(\frac{z}{\overline{u}\phi_M}\right)\left(\frac{\phi_E}{\phi_M}\right)^{2/3}}{1.0+s_{2,K}\left(\frac{fz}{\overline{u}\phi_M}\right)^{5/3}},\quad K=u,v,w$$
NREL National Wind Technology Center Model	$$S_K(f)=\sum_{i=1}^{NumPeaks_K} p_{i,K}S_{K,SMOOTH}\left(F_{i,K}f\right)$$
NREL Great Plains Low-Level Jet Model	$$S_K(f)=\frac{u_*^2}{UStar^2}\sum_{i=1}^{NumPeaks_K} p_{i,K}S_{K,SMOOTH}\left(F_{i,K}f\right)$$

Table 2.2 Commonly Used Spatial Coherence Models

Coherence for IEC Spectral Models	The coherence function for the *u*-component of the IEC spectral models is defined as $$Coh_{i,j} = \exp\left(-a\sqrt{\left(\frac{fr}{\overline{u}_{hub}}\right)^2 + \left(0.12\frac{r}{L_c}\right)^2} \right)$$ where *f* is frequency; *r* is the distance between points *i* and *j*; *a* is the coherence decrement; $\overline{u}_{hub}$ is the mean wind speed at hub height; L_c is a coherence scale parameter. For IEC 61400-1 3rd Ed., *a* and L_c are defined as $$a = 12$$ $$L_c = 5.67\min\left(60\text{ m, hub height}\right)$$ TurbSim defines the coherence for the *v* and *w* components as $$Coh_{i,j} = \begin{cases} 1 & i = j \\ 0 & i \neq j \end{cases}$$
Coherence for Non-IEC Spectral Models	For *u*, *v*, and *w* wind speed components $$Coh_{i,j_K} = \exp\left(-a_K\left(\frac{r}{z_m}\right)^{CohExp}\sqrt{\left(\frac{fr}{\overline{u}_m}\right)^2 + \left(b_K r\right)^2} \right)$$

2.2 Aerodynamic Wind Load Calculation

The simulated 10-minute wind field realization is used for the aerodynamic wind load calculation. The aerodynamic code AeroDyn (Moriarty and Hansen, 2005) includes the Beddoes-Leishman dynamic stall model (Leishman and Beddoes, 1989), Prandtl's tip loss and Glauert correction (Glauert, 1935), and hub loss on empirically determined sectional force coefficients. Moreover, it employs the classic blade element momentum (BEM) theory and the generalized dynamic wake model to calculate the effect of the wake on the turbine rotor aerodynamics. However, since the input force coefficients to AeroDyn are empirically based, it can only provide the resultant aerodynamic forces and moments at each aerodynamic center of discrete blade sections, not the pressure distribution on the blade surface. When these concentrated forces and moments are

applied to a detailed stress analysis by finite element analysis (FEA) (e.g., Hu *et al.*, 2013b), two problems could potentially occur. One is that the effect of pressure on the blade surface is ignored. The other is that, when using concentrated forces in FEA, local stress concentration will occur. On the other hand, XFOIL (Drela and Youngren, 2001) can calculate the pressure distribution on the airfoil using a potential flow solver. However, XFOIL is not expected to be accurate in the prediction of stall because of the presence of separated, unsteady, and 3-D flows in rotating coordinate systems (Giovanni *et al.*, 2011).

In order to take advantage of the two existing well-known codes (AeroDyn and XFOIL) while overcoming their drawbacks for the present application, the original wind pressure distribution obtained from XFOIL can be modified to match the aerodynamic coefficients calculated from AeroDyn. It is assumed that this will not accurately replicate the true pressure distribution on the wing since the XFOIL solution does not take into account effects such as dynamic stall and blade rotation. It is expected that the fatigue analysis will not be sensitive to the specific local pressure distribution and that this method will allow the AeroDyn-predicted force coefficients to be determined using a quasi-physical pressure distribution. As discussed for future work by Bottasso *et al.* (Bottasso *et al.*, 2014), reconstructing the chord-wise pressure distribution using assumed shapes from experimental measurements or from numerical models such as XFOIL is a more realistic way of representing aerodynamic loads. Due to the complexity of involving the aero-elastic effect in the current modified wind pressure, the blade is un-deformed when calculating the aerodynamic wind load for fatigue analysis within AeroDyn. The modified wind pressure involving the aero-elastic effect would be included in future work.

The pressure coefficient distribution on the circumference of the airfoil is assumed to be modified as

$$C_p^*(x) = \left(c_0 + c_1 x + c_2 x^2\right) C_p(x) \tag{2.9}$$

where x is the coordinate point along the chord length (see Figure 2.2(a)), $C_p(x)$ is the original pressure distribution obtained from XFOIL, and c_0, c_1, and c_2 are the three coefficients to be determined by matching the lift, drag, and moment coefficients, respectively, to the values computed by AeroDyn. The lift, drag, and moment coefficients are calculated by directly integrating the surface pressure coefficients computed using XFOIL, respectively, as

$$C_l = L/q = \oint C_p d\bar{x} \approx \left(\sum_i^n C_{pi}\Delta x_i\right)\cos\alpha + \left(\sum_i^n C_{pi}\Delta y_i\right)\sin\alpha \tag{2.10}$$

$$C_d = D/q = \oint -C_p d\bar{y} \approx \left(\sum_i^n C_{pi}\Delta x_i\right)\sin\alpha - \left(\sum_i^n C_{pi}\Delta y_i\right)\cos\alpha \tag{2.11}$$

$$\begin{aligned} C_m = M/q &= \oint -C_p\left[\left(x - x_{ref}\right)dx + \left(y - y_{ref}\right)dy\right] \\ &\approx \sum_i^n -C_{pi}\left[\left(x_i - x_{ref}\right)\Delta x_i + \left(y_i - y_{ref}\right)\Delta y_i\right] \end{aligned} \tag{2.12}$$

where $\bar{x} = x\cos\alpha + y\sin\alpha$, $\bar{y} = y\cos\alpha - x\sin\alpha$, n is the number of discrete airfoil panels determined by XFOIL, (x_{ref}, y_{ref}) defines the aerodynamic center of the normalized airfoil, and C_{pi} is the original pressure coefficient at ith discrete panel. Substituting the modified pressure coefficient from Eq. (2.9) into Eqs. (2.10) - (2.12), the modified lift, drag, and moment coefficients can be expressed, respectively, as

$$\begin{aligned} C_l^* &= \oint C_p^* d\bar{x} = \oint\left[\left(c_0 + c_1 x + c_2 x^2\right)C_p\right]d\bar{x} \\ &\approx \left[\sum_i^n \left(c_0 + c_1 x_i + c_2 x_i^2\right)C_{pi}\Delta x_i\right]\cos\alpha + \left[\sum_i^n \left(c_0 + c_1 x_i + c_2 x_i^2\right)C_{pi}\Delta y_i\right]\sin\alpha \end{aligned} \tag{2.13}$$

$$\begin{aligned} C_d^* &= \oint -C_p^* d\bar{y} \approx \left(\sum_i^n C_{pi}^*\Delta x_i\right)\sin\alpha - \left(\sum_i^n C_{pi}^*\Delta y_i\right)\cos\alpha \\ &= \left[\sum_i^n \left(c_0 + c_1 x_i + c_2 x_i^2\right)C_{pi}\Delta x_i\right]\sin\alpha - \left[\sum_i^n \left(c_0 + c_1 x_i + c_2 x_i^2\right)C_{pi}\Delta y_i\right]\cos\alpha \end{aligned} \tag{2.14}$$

$$C_m^* = \oint -C_p^* \left[\left(x - x_{ref} \right) dx + \left(y - y_{ref} \right) dy \right] \approx \sum_i^n -C_{pi}^* \left[\left(x_i - x_{ref} \right) \Delta x_i + \left(y_i - y_{ref} \right) \Delta y_i \right]$$
$$= \sum_i^n -\left[\left(c_0 + c_1 x_i + c_2 x_i^2 \right) C_{pi} \right] \left[\left(x_i - x_{ref} \right) \Delta x_i + \left(y_i - y_{ref} \right) \Delta y_i \right] \quad (2.15)$$

where C_{pi}^* is the modified pressure coefficient at the *i*th discrete panel.

Equations (2.13) to (2.15) can be simplified as the following matrix equation:

$$\begin{bmatrix} K_{l1} & K_{l2} & K_{l3} \\ K_{d1} & K_{d2} & K_{d3} \\ K_{m1} & K_{m2} & K_{m3} \end{bmatrix} \begin{bmatrix} c_0 \\ c_1 \\ c_2 \end{bmatrix} = \begin{bmatrix} C_l^* \\ C_d^* \\ C_m^* \end{bmatrix} \quad (2.16)$$

where the linear coefficients K_{ij} ($i = l, d, m$ indicating lift, drag, and moment, respectively; $j = 1, 2, 3$) are functions of angle of attack α, original pressure coefficient obtained from XFOIL C_{pi}, and coordinates of points on the airfoil (x, y). The explicit forms of K_{ij} are derived as

$$K_{l1} = \cos\alpha \sum_i^n C_{pi} \Delta x_i + \sin\alpha \sum_i^n C_{pi} \Delta y_i \quad (2.17)$$

$$K_{l2} = \cos\alpha \sum_i^n x_i C_{pi} \Delta x_i + \sin\alpha \sum_i^n x_i C_{pi} \Delta y_i \quad (2.18)$$

$$K_{l3} = \cos\alpha \sum_i^n x_i^2 C_{pi} \Delta x_i + \sin\alpha \sum_i^n x_i^2 C_{pi} \Delta y_i \quad (2.19)$$

$$K_{d1} = \sin\alpha \sum_i^n C_{pi} \Delta x_i - \cos\alpha \sum_i^n C_{pi} \Delta y_i \quad (2.20)$$

$$K_{d2} = \sin\alpha \sum_i^n x_i C_{pi} \Delta x_i - \cos\alpha \sum_i^n x_i C_{pi} \Delta y_i \quad (2.21)$$

$$K_{d3} = \sin\alpha \sum_i^n x_i^2 C_{pi} \Delta x_i - \cos\alpha \sum_i^n x_i^2 C_{pi} \Delta y_i \quad (2.22)$$

$$K_{m1} = \sum_i^n C_{pi} \left[\left(x_{ref} - x_i \right) \Delta x_i + \left(y_{ref} - y_i \right) \Delta y_i \right] \quad (2.23)$$

$$K_{m2} = \sum_{i}^{n} x_i C_{pi} \left[\left(x_{ref} - x_i \right) \Delta x_i + \left(y_{ref} - y_i \right) \Delta y_i \right] \tag{2.24}$$

$$K_{m3} = \sum_{i}^{n} x_i^2 C_{pi} \left[\left(x_{ref} - x_i \right) \Delta x_i + \left(y_{ref} - y_i \right) \Delta y_i \right] \tag{2.25}$$

By equating the modified lift, drag, and moment coefficients with the corresponding coefficients calculated from the AeroDyn analysis, coefficients c_0, c_1, and c_2 can be calculated. Consequently, the modified blade surface pressure distribution can be obtained by substituting c_0, c_1, and c_2 into Eq. (2.9). The above calculation procedure has to be repeated for all the blade sections and at each angle of attack experienced by each blade section in the AeroDyn simulation.

As a case study, the 5-MW NREL reference wind turbine blade (Jonkman *et al.*, 2009b) is used to carry out the above surface pressure modification incorporating both AeroDyn and XFOIL. Figure 2.1 shows the relationships between aerodynamic coefficients and angle of attack at blade section 12, which is indicated in Figure 2.3(a). The asterisks that are directly obtained from the AeroDyn analysis show that the aerodynamic coefficients are not deterministic functions of angle of attack but are scattered, as shown in Figure 2.1. Because fatigue analysis cannot afford the computational time for each individual realization, this study does not consider the variation of aerodynamic force coefficients at one angle of attack. Instead, a fifth-order polynomial regression model is used to fit the coefficient data obtained from AeroDyn in a least-square sense. The polynomial regression model (crosses in Figure 2.1) is overlapped by aerodynamic coefficients integrated from modified wind pressure (circles in in Figure 2.1). The coincidence between the polynomial model from AeroDyn data and the integrated result from the modified pressure verifies that the modified pressure can produce the same aerodynamic force coefficients as those obtained from AeroDyn.

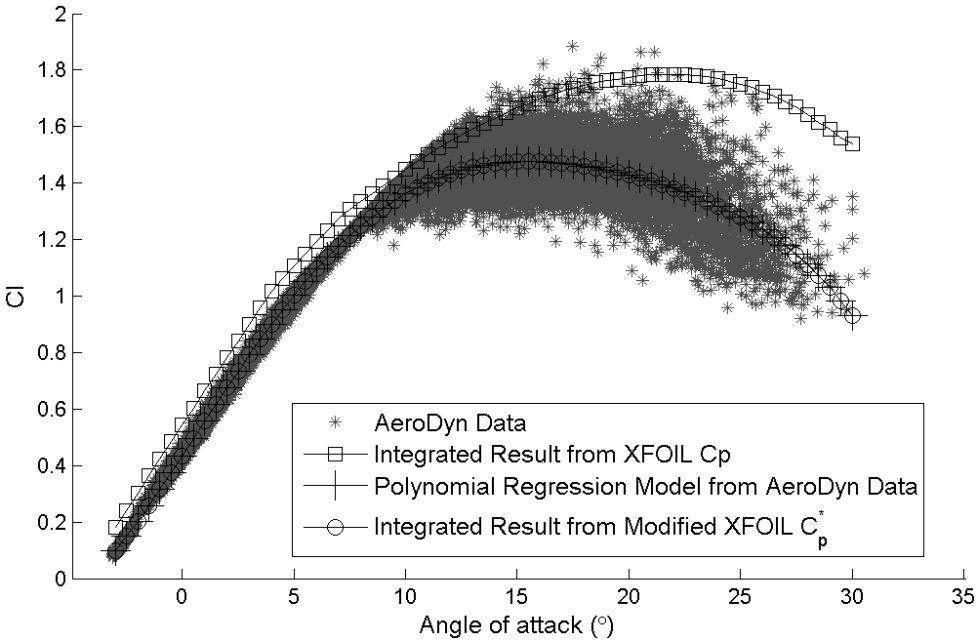

(a) Lift coefficient and angle of attack

Figure 2.1 Relationship between Aerodynamic Coefficients and Angle of Attack at Blade Section 12

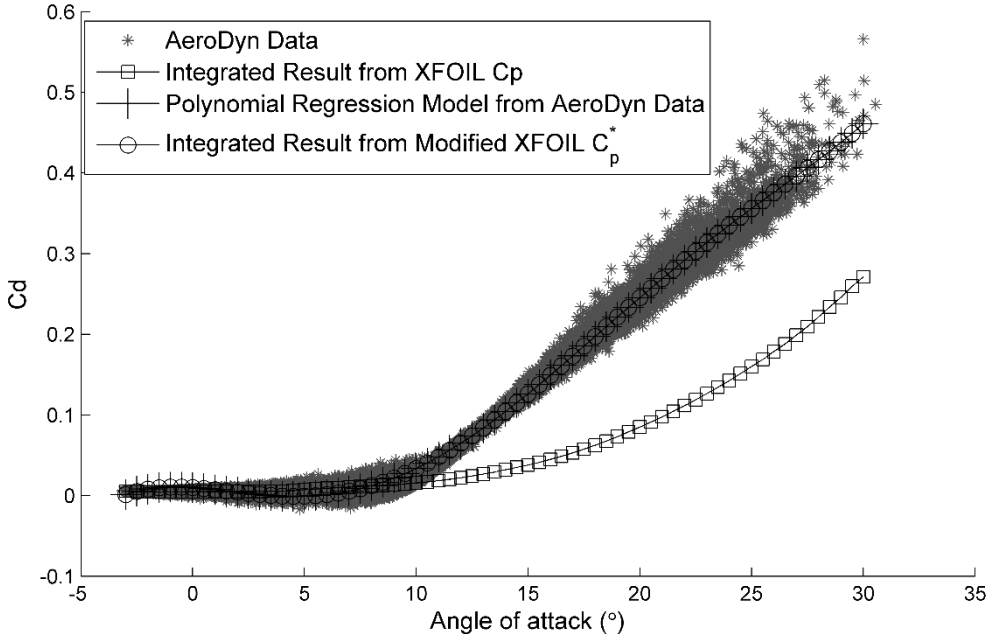

(b) Drag coefficient and angle of attack

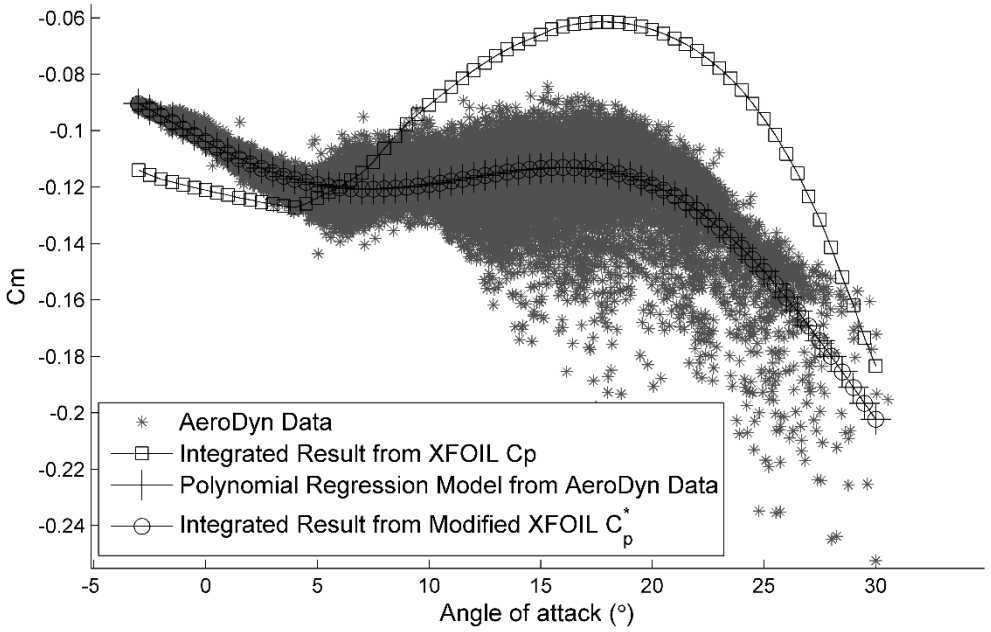

(c) Moment coefficient and angle of attack

Figure 2.1 Relationship between Aerodynamic Coefficients and Angle of Attack at Blade Section 12 (Continued)

In total, 283 groups of modified wind pressure coefficients corresponding to 17 blade sections have been obtained. A comparison of the original and modified wind pressure coefficient distribution at blade section 12, which is under a 4 degree angle of attack, is shown in Figure 2.2. Figure 2.2(a) shows the normalized airfoil NACA64-A17 section used in blade section 12. In Figure 2.2(b), the dash-dotted line and solid line show the original wind pressure coefficient distribution on the upper curve and the lower curve of the airfoil, respectively. The original wind pressure distribution was directly calculated from XFOIL. The circled line in Figure 2.2(b) represents the modified wind pressure coefficient distribution. As shown in Figure 2.2(b), the basic form of the pressure distribution is retained. However, there is a clear difference near the leading edge of the suction side of the airfoil. It is worth noting that the difference between the original and modified pressure distribution may vary at different locations, at other angles of attack, and for other airfoils.

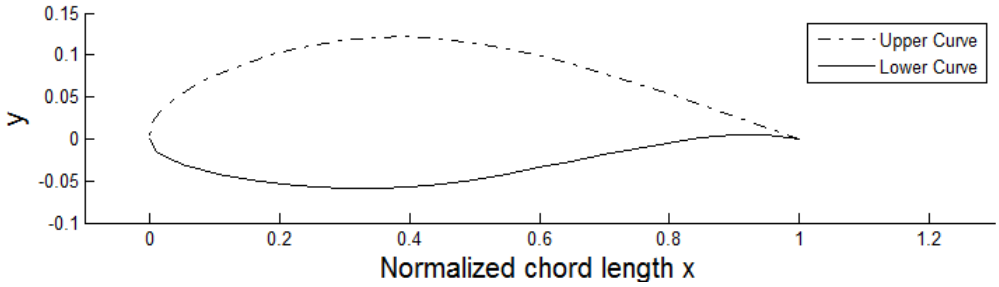

(a) Airfoil NACA64-A17 used at blade section 12

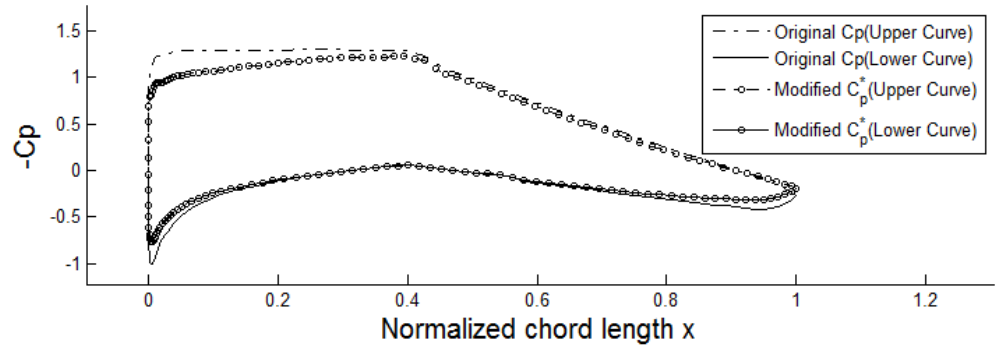

(b) Comparison of original and modified wind pressure coefficient distribution at blade section 12, which is under a 4 degree angle of attack

Figure 2.2 Airfoil NACA64-A17 Used at Blade Section 12 and Wind Pressure Comparison

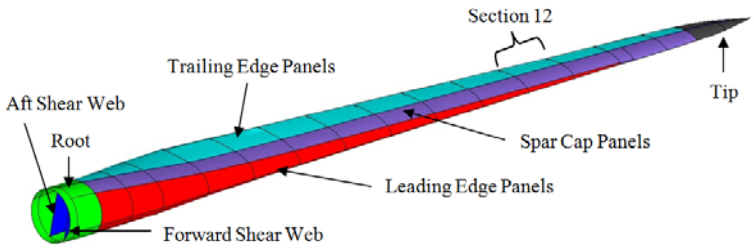

(a) Blade geometry

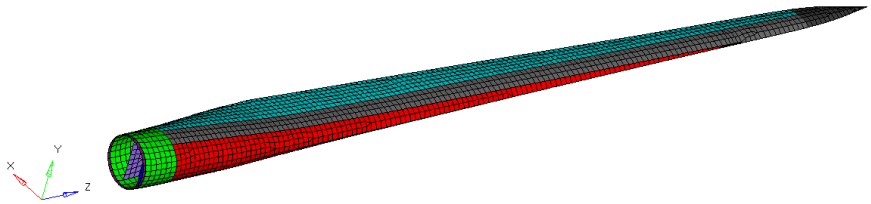

(b) Blade mesh

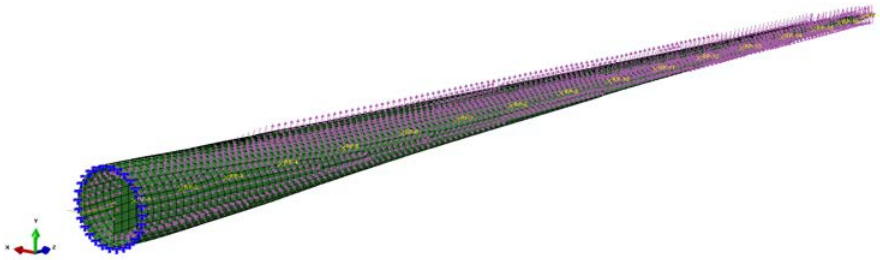

(c) Modified wind pressure coefficients applied on outer surface of the blade

Figure 2.3 Current Wind Turbine Blade Model

2.3 Fatigue Damage Evaluation

2.3.1 Parametric Blade Modeling

A composite blade considered in this study is similar to the 5-MW NREL reference wind turbine composite blade (Jonkman *et al.*, 2009b). The aerodynamic properties, e.g., airfoil type, chord length, and twist angle, are the same, but the material properties and laminate schedules are different from those of the NREL blade. At the same time, the materials distribution is such that mass distribution in a span-wise direction is similar to the NREL blade. A refined blade geometry model (Figure 2.3(a)) was generated in Pro/E (Pro/ENGINEER, 2009) by connecting 34 airfoils, which smooth the transition from section to section and reduce the stress concentration. The blade is composed of seven parts, which are the root, forward shear web, aft shear web, leading edge, spar cap, trailing edge, and tip (see Figure 2.3(a)). The forward shear web, aft shear web, leading edge, and trailing edge consist of sandwich panels, in which composite laminates are laid at both the top and bottom surfaces and a foam core is laid in the middle. Other parts are made of composite laminates. The meshed model (Figure 2.3(b)) generated by HyperMesh (HyperWorks, 2012) was imported into Abaqus (ABAQUS/CAE, 2011), which implements layered shell elements for FEA. For aerodynamic wind load application, the blade is divided into 17 sections in the spanwise direction. Each section possesses the same aerodynamic property as the 5-MW NREL blade model. Thus, the modified wind pressure coefficient distributions obtained in the studied case in Section 2.2 can be applied at the outer surface of each blade section (Figure 2.3(c)).

Table 2.3 lists the elastic properties, ultimate strength, and density data for the materials used in the blade. Composite materials QQ1 and P2B are selected from the SNL/MSU/DOE Composite Material Fatigue Database (Mandell and Smaborsky, 2014). QQ1 is a glass-fiber-reinforced epoxy laminate that consists of Vantico TDT 177-155

Epoxy Resin, Saertex U14EU920-00940-T1300-100000 0's, and VU-90079-00830-01270-000000 45's fabrics (Mandell and Smaborsky, 2014). P2B is a carbon/glass-hybrid-fiber-reinforced epoxy laminate that consists of Newport carbon NB307-D1-34-600 G300 prepreg 0° and glass NB307-D1-7781-497A for ±45° (Mandell and Smaborsky, 2014). CorecellTM M-Foam M200 (Corecell M-Foam, URL: http://www.gurit.com/gurit-corecell-m.aspx) is selected as the core material in the sandwich panels. The QQ1, P2B, and foam core are treated as homogeneous and orthotropic layers when constructing the laminate schedule, as explained below.

Table 2.3 Material Properties of Composite Materials and Foam Core

Material property	QQ1	P2B	Foam
Longitudinal Young's modulus E_1 (GPa)	33.1	101	0.334
Transversal Young's modulus E_2 (GPa)	17.1	8.86	0.334
Poisson's ratio ν_{12}	0.27	0.22	0.33
Shear modulus G_{12} (GPa)	6.29	6.37	0.098
Shear strength S (MPa)	141	137	2.95
Longitudinal tensile strength X_T (MPa)	843	1546	4.29
Longitudinal compressive strength X_C (MPa)	687	1047	4.40
Transversal tensile strength Y_T (MPa)	149	80	4.29
Transversal compressive strength Y_C (MPa)	274	240	4.40
Density ρ (kg/m^3)	1919	1570	200

The laminate schedule for each panel was developed by referring to available blade models (Griffith and Ashwill, 2011; Jonkman *et al.*, 2009b). The objective is to generate a blade model that has a mass distribution similar to that of the 5-MW NREL reference wind turbine blade in the span-wise direction. Table 2.4 provides the detailed

laminate schedule, which includes material types, layer thicknesses, and layer orientations. The thickness of each QQ1 layer is assumed to be 4 mm, while the thickness of each P2B layer is assumed to be 2.5 mm. The isotropic foam layer has a thickness of 36 mm and is placed in the middle of the sandwich panels. The distributed blade sectional mass and each part's mass information are given in Table 2.5. A comparison of the mass distribution between the blade model and the 5-MW NREL reference blade (Jonkman *et al.*, 2009b) is shown in Figure 2.4. It can be seen that the masses per unit length of the root and aerodynamic blade sections are very close to those of the 5-MW NREL reference blade model. The parametric blade model can easily tailor the laminate thickness design variables, which will be used in DDO (Chapter 4) and RBDO (Chapter 6).

Table 2.4 Laminate Schedule for the Blade Model

Section ID	Blade Span	Root		Forward Shear Web		Aft Shear Web		Tip	
		QQ1		QQ1/Foam/QQ1		QQ1/Foam/QQ1		QQ1	
		T (mm)	O (°)	T (mm)	O (°)	T (mm)	O (°)	T (mm)	O (°)
1	0.022	28	$[\pm 45/+45/\overline{-45}]_S$	8/36/8	$[0_2]/0/[0_2]$	8/36/8	$[0_2]/0/[0_2]$		
2	0.067			8/36/8	$[0_2]/0/[0_2]$	8/36/8	$[0_2]/0/[0_2]$		
3	0.111			8/36/8	$[0_2]/0/[0_2]$	8/36/8	$[0_2]/0/[0_2]$		
4	0.167			8/36/8	$[0_2]/0/[0_2]$	8/36/8	$[0_2]/0/[0_2]$		
5	0.233			8/36/8	$[0_2]/0/[0_2]$	8/36/8	$[0_2]/0/[0_2]$		
6	0.300			8/36/8	$[0_2]/0/[0_2]$	8/36/8	$[0_2]/0/[0_2]$		
7	0.367			8/36/8	$[0_2]/0/[0_2]$	8/36/8	$[0_2]/0/[0_2]$		
8	0.433			8/36/8	$[0_2]/0/[0_2]$	8/36/8	$[0_2]/0/[0_2]$		
9	0.500			8/36/8	$[0_2]/0/[0_2]$	8/36/8	$[0_2]/0/[0_2]$		
10	0.567			8/36/8	$[0_2]/0/[0_2]$	8/36/8	$[0_2]/0/[0_2]$		
11	0.633			8/36/8	$[0_2]/0/[0_2]$	8/36/8	$[0_2]/0/[0_2]$		
12	0.700			8/36/8	$[0_2]/0/[0_2]$	8/36/8	$[0_2]/0/[0_2]$		
13	0.767			8/36/8	$[0_2]/0/[0_2]$	8/36/8	$[0_2]/0/[0_2]$		
14	0.833					8/36/8	$[0_2]/0/[0_2]$		
15	0.889					8/36/8	$[0_2]/0/[0_2]$		
16	0.933					8/36/8	$[0_2]/0/[0_2]$	8	[±45]
17	0.978							8	[±45]

Table 2.4 Laminate Schedule for the Blade Model (Continued)

Section ID	Blade Span	Leading Edge Panels QQ1/Foam/QQ1		Trailing Edge Panels QQ1/Foam/QQ1		Spar Cap Panels P2B	
		T (mm)	O (°)	T (mm)	O (°)	T (mm)	O (°)
1	0.022						
2	0.067	8/36/8	$[\pm 45]/0/[\mp 45]$	8/36/8	$[\pm 45]/0/[\mp 45]$	15	$[\pm 45/-45]_S$
3	0.111	8/36/8	$[\pm 45]/0/[\mp 45]$	8/36/8	$[\pm 45]/0/[\mp 45]$	15	$[\pm 45/-45]_S$
4	0.167	12/36/12	$[\pm 45/45]/0/[45/\mp 45]$	8/36/8	$[\pm 45]/0/[\mp 45]$	25	$[(\pm 45)_2/45]_S$
5	0.233	8/36/8	$[\pm 45]/0/[\mp 45]$	8/36/8	$[\pm 45]/0/[\mp 45]$	25	$[(\pm 45)_2/45]_S$
6	0.300	4/36/4	$[45]/0/[-45]$	4/36/4	$[45]/0/[-45]$	25	$[(\pm 45)_2/45]_S$
7	0.367	4/36/4	$[45]/0/[-45]$	4/36/4	$[45]/0/[-45]$	25	$[(\pm 45)_2/45]_S$
8	0.433	4/36/4	$[45]/0/[-45]$	4/36/4	$[45]/0/[-45]$	25	$[(\pm 45)_2/45]_S$
9	0.500	4/36/4	$[45]/0/[-45]$	4/36/4	$[45]/0/[-45]$	25	$[(\pm 45)_2/45]_S$
10	0.567	4/36/4	$[45]/0/[-45]$	4/36/4	$[45]/0/[-45]$	20	$[\pm 45]_{2S}$
11	0.633	4/36/4	$[45]/0/[-45]$	4/36/4	$[45]/0/[-45]$	15	$[\pm 45/45]_S$
12	0.700	4/36/4	$[45]/0/[-45]$	4/36/4	$[45]/0/[-45]$	10	$[\pm 45]_S$
13	0.767	4/36/4	$[45]/0/[-45]$	4/36/4	$[45]/0/[-45]$	10	$[\pm 45]_S$
14	0.833			4/36/4	$[45]/0/[-45]$	10	$[\pm 45]_S$
15	0.889			4/36/4	$[45]/0/[-45]$	10	$[\pm 45]_S$
16	0.933						
17	0.978						

Note: Blade Span - Normalized distance from center of each section to root boundary, T - Thickness of layers, O - Orientation of layers. Orientation angles are measured positive counterclockwise relative to the default shell local directions, which are projected from the global rectangular Cartesian coordinate system of the blade.

Table 2.5 Distributed Blade Mass

Section ID	Section Width (m)	Section Mass (ton)	BMassDen (kg/m)	Part Name	Part Mass (ton)
1	2.7333	2.0380	745.6291	Root	1.5246
2	2.7333	1.6483	603.0344	Forward Shear Web	2.1122
3	2.7333	1.5611	571.1488	Aft Shear Web	2.4529
4	4.1000	2.4718	602.8756	Tip	0.2230
5	4.1000	2.0328	495.7976	Leading Edge Panels	2.4673
6	4.1000	1.4220	346.8200	Trailing Edge Panels	5.7002
7	4.1000	1.2988	316.7907	Spar Cap Panels	4.0180
8	4.1000	1.1972	292.0105	Total Mass (ton)	18.4981
9	4.1000	1.0975	267.6793		
10	4.1000	0.9171	223.6918		
11	4.1000	0.7514	183.2579		
12	4.1000	0.5874	143.2674		
13	4.1000	0.5221	127.3410		
14	4.1000	0.4365	106.4681		
15	2.7333	0.2622	95.9165		
16	2.7333	0.1950	71.3273		
17	2.7333	0.0590	21.5856		
Note: BMassDen - blade mass density.					

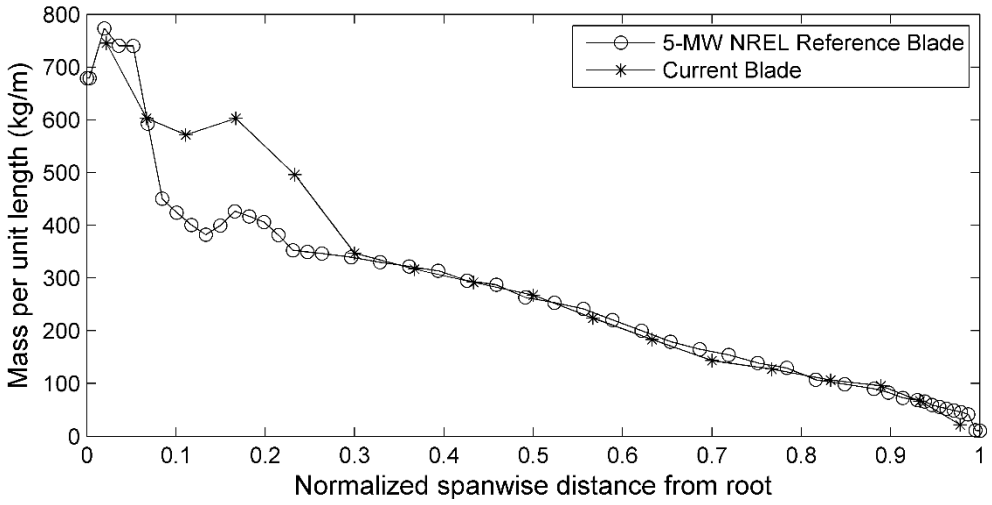

Figure 2.4 Comparison of Blade Mass Distribution

2.3.2 Stress Calculation

For stress calculation, the modified wind pressure coefficient distributions (Section 2.2) are selected as wind load cases based on the mean angles of attack of blade sections. For example, if the mean angle of attack of blade section 12 under a wind condition, i.e., V_{10} and I_{10}, is 3.6 degrees and the closest angle of attack with available modified wind pressure coefficient distribution is 4 degrees (Figure 2.2(b)), then the modified wind pressure coefficient distribution for the 4 degree angle is selected for blade section 12 as a wind load case. The selected wind load cases are then applied on the outer surface of 17 blade sections (Figure 2.3(c)). In addition to the wind load, gravity load and centrifugal load are included in FEA using Abaqus. The rotational speed, which is assumed to be constant (12.1 rpm) for different wind conditions, is used to calculate the centrifugal load. Shell elements S4 and S3R are used to calculate plane stress components. Six degrees of freedom of the root boundary are fixed in FEA. Matlab

(MATLAB, 2012) scripts are developed to extract the resulting stress components, and the full stress time series are calculated as

$$\sigma_{ij}(t) = \sum_{k=1}^{17} P_k(t)\sigma_{ij,Wk} + \sigma_{ij,G}(t) + \sigma_{ij,C}(t) \tag{2.26}$$

where $\sigma_{ij}(t)$ denotes superposed time series of a stress component, $P_k(t)$ is the dynamic wind pressure history calculated by AeroDyn at blade section k, $\sigma_{ij,Wk}$ is the stress components for wind load at blade section k, $\sigma_{ij,G}(t)$ is the stress history due to the gravity load, and $\sigma_{ij,C}(t)$ is the stress history due to the centrifugal load. All stress results are in the principal material coordinates.

In this study, the stress distributions as well as fatigue damage have been studied at section points, which indicate specific locations through laminate thickness. Thus multiple section points are associated with one finite element (FE) node (see Figure 2.5(b)). A combination of node ID and section point ID, named *node-section point*, is used to identify the stress, fatigue, and probability of failure at specific location of the blade. For example, node 2797-section point 1 indicates the first section point associated with the node 2797 as shown in Figure 2.5.

It is found that the stress is piece-wise linearly varied through laminate thickness, which is consistent with the classical laminate theory of composite materials. Extreme stresses occur at either the top or bottom section points of layers with the same orientation. As an example, a randomly selected node 2797 at the root, which has 7 layers with a stacking sequence of $[\pm 45/+45/\overline{-45}]_S$ (see Table 2.4), is shown in Figure 2.5. Three section points are uniformly distributed in each layer. Longitudinal stress component σ_{11} through laminate thickness at node 2797 under a load case is illustrated. As shown in Figure 2.5(c), the maximum σ_{11} occurs at section point 1, which is the bottom section point of the +45° layers, and the minimum σ_{11} occurs at section point 18, which is the top section point of the −45° layers.

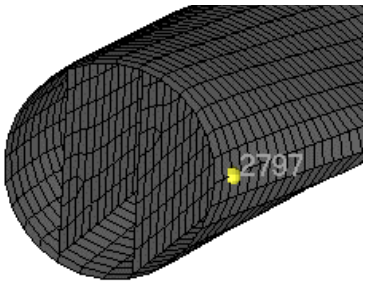

(a) Node 2797 on the blade root

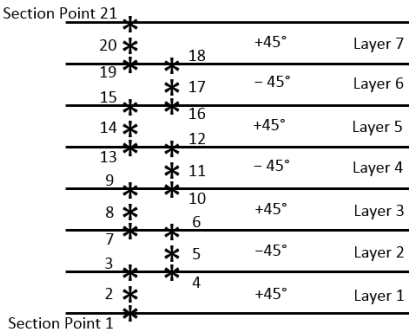

(b) Section points of node 2797

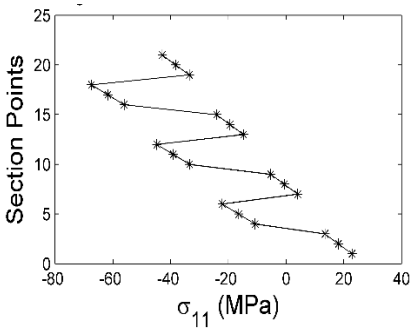

(c) σ_{11} of section points of node 2797

Figure 2.5 Demonstration of Stress Analysis through Laminate Thickness

2.3.3 Non-proportional Multi-axial Fatigue Damage Calculation

The stress time series obtained in Section 2.3.2 reveal that the blade bears non-proportional multi-axial complex stress states of variable amplitude and mean. The differentiation between proportional and non-proportional cyclic loadings is described by Nussbaumer *et al.* (Nussbaumer *et al.*, 2011). The non-proportional stresses usually result from the action of at least two loadings that vary non-proportionally with time in a different manner. The non-proportionality of stresses in wind turbine blades is due to the fact that the wind load, gravity load, and centrifugal load vary non-proportionally with time. As an illustration, stress histories of longitudinal normal stress σ_{11}, transverse normal stress σ_{22}, and shear stress σ_{12} of node 2797-section point 1 (Figure 2.5) are provided in Figure 2.6. The ratio between any two of the three stress components in Figure 2.6 is not constant with time.

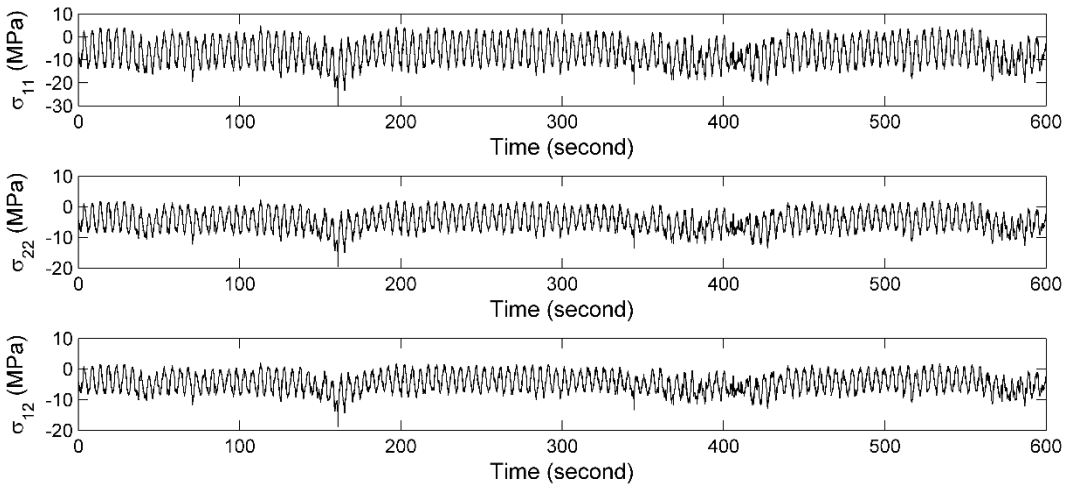

Figure 2.6 Time Series of Stress Components at Node 2797-Section Point 1

In order to rationally count cycles for current non-proportional multi-axial complex stress states, the time moments for the stress reversal, i.e., peak or valley, for each of the stress components, are recorded first. Then the stress states (σ_{11}, σ_{22}, σ_{12}) at the recorded time moments are selected for cycle counting. Since the rainflow cycle counting breaks the cycle sequence, it could not count cycles for non-proportional stress time series. In order to have cycle-by-cycle fatigue analyses, a range-mean counting method (ASTM, 2005) is applied to count all the half cycles. The stress path from one stress state to the immediately following stress state is defined as one half cycle. According to the Tsai-Hill criterion (Jones, 1999), a multi-axial fatigue damage index caused in a half cycle under a stress level (σ^i_{11}, σ^i_{22}, σ^i_{12}) is computed as (Liu and Mahadevan, 2005)

$$D^i = 0.5\sqrt{\frac{1}{\left(N^i_{11}\right)^2}+\frac{1}{\left(N^i_{22}\right)^2}+\frac{1}{\left(N^i_{12}\right)^2}+\frac{1}{N^i_{11}N^i_{22}}} \tag{2.27}$$

where N^i_{11},N^i_{22}, and N^i_{12} are the number of allowable cycles under pure stress components σ^i_{11}, σ^i_{22}, and σ^i_{12}, respectively. The coefficient 0.5 indicates the half cycle.

2.3.4 Probabilistic S-N Curves and Constant Life Diagrams

In this study, the number of allowable cycles N_{ij} is calculated based on the S-N curve. The S-N curve equation is expressed as

$$\sigma^a_{ij} = s_{ij}N^{-1/k_{ij}}_{ij} \tag{2.28}$$

where N_{ij} is the number of cycles to failure, and s_{ij} and k_{ij} are fatigue strength coefficients corresponding to a stress ratio R. The stress ratio R equals the ratio of the minimum cyclic stress to the maximum cyclic stress. The fatigue strength coefficients used to construct S-N curves and constant life diagrams (CLDs) are statistically treated to represent a 95% survival probability with a confidence level of 95% (ASTM, 2004). The 95% lower bound of S-N curve and CLD is used for the fatigue analysis. The

probabilistic S-N curve of P2B material in the longitudinal direction under stress ratio *R* = 10 is illustrated in Figure 2.7.

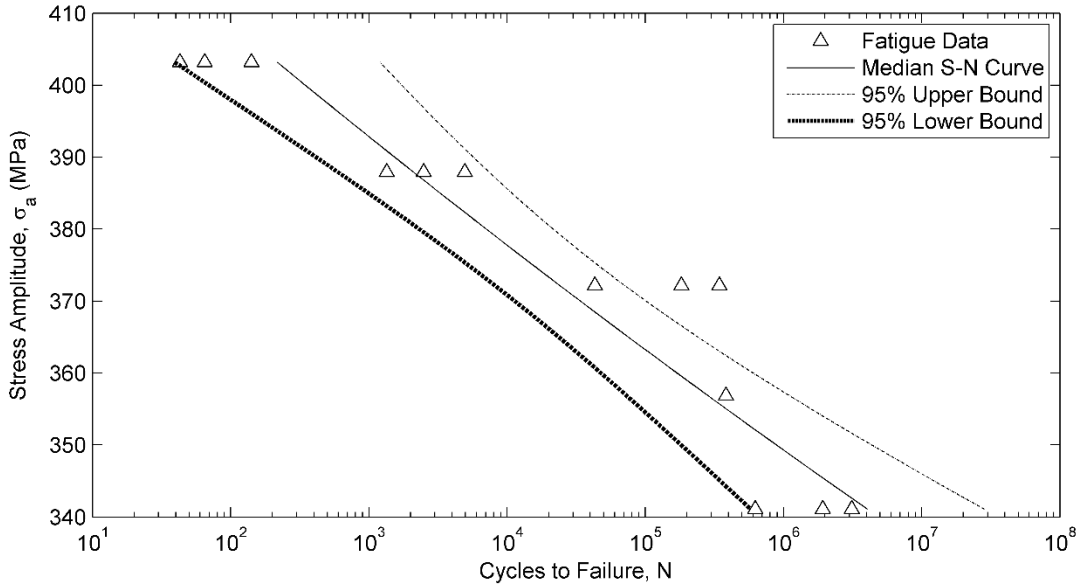

Figure 2.7 Probabilistic S-N Curves of P2B in Longitudinal Direction under *R*=10

The S-N curves under arbitrary stress ratio are calculated by using CLD (Vassilopoulos and Keller, 2011). In order to derive S-N curves for each stress component, three CLDs corresponding to three stress components are necessary. Fatigue test data for QQ1 and P2B materials, including stress amplitudes and numbers of cycles tested in longitudinal and transverse directions (Mandell and Samborsky, 2014), are used to generate the S-N curves corresponding to tested stress ratios 10, −2, −1, −0.5, 0.1, 0.5, and 0.7. By utilizing the generated S-N curves, piecewise linear CLDs of QQ1 and P2B are constructed. Figure 2.8 shows CLDs, corresponding to 10^2, 10^3, 10^4, 10^5, 10^6, 10^7, and 10^8 allowable numbers of stress cycles, for QQ1 and P2B materials in both the

longitudinal and transverse directions. As the allowable numbers of stress cycles increase, the corresponding stress mean and amplitude decrease. It is also worth noting that the 95% lower bound results in more conservative fatigue resistance, and the fatigue resistance of P2B is larger than that of QQ1 in the longitudinal direction, but smaller in the transverse direction. For both P2B and QQ1, the fatigue resistance in the longitudinal direction is much larger than that in the transverse direction.

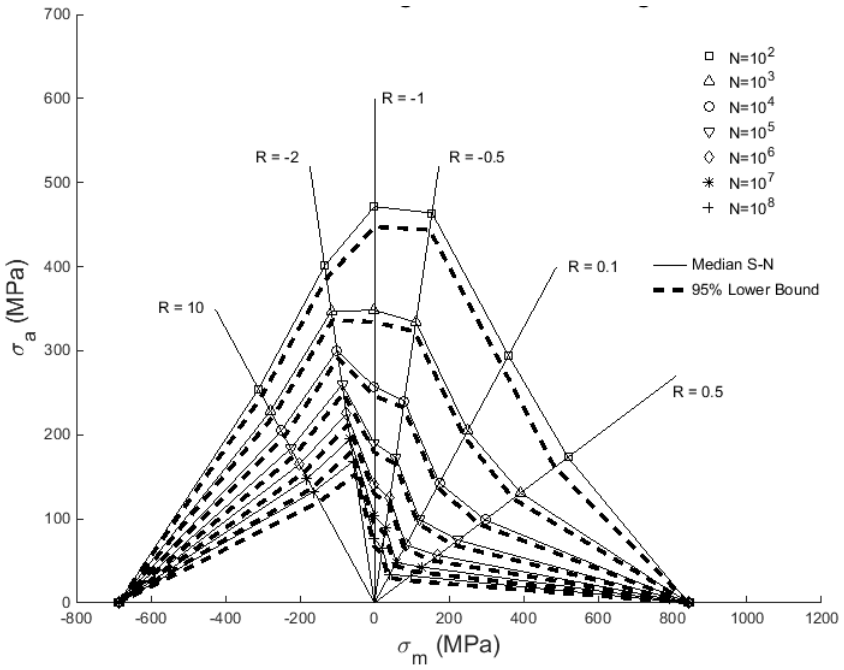

(a) Probabilistic constant life diagrams of QQ1 in longitudinal direction

Figure 2.8 Probabilistic Constant Life Diagrams of QQ1 and P2B in Longitudinal and Transverse directions

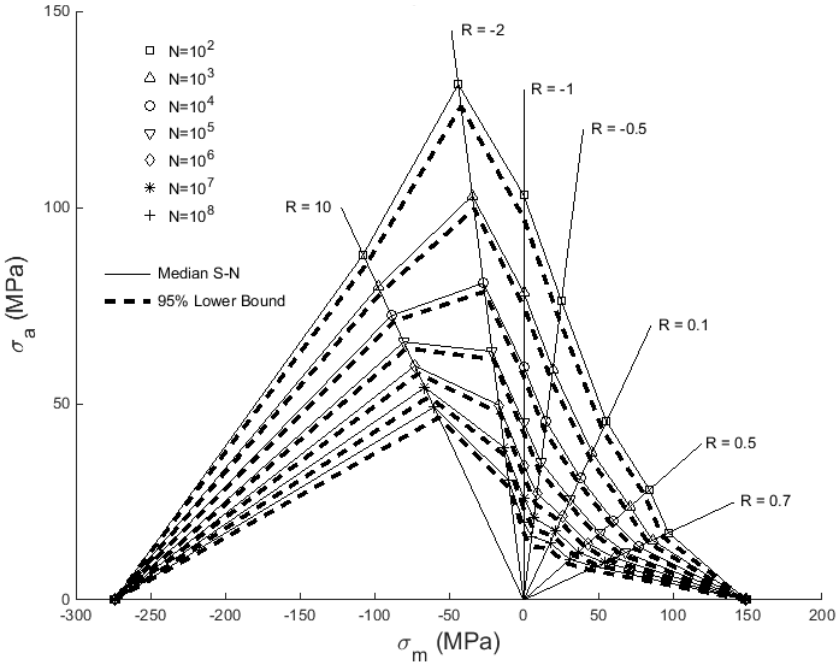

(b) Probabilistic constant life diagrams of QQ1 in transverse direction

Figure 2.8 Probabilistic Constant Life Diagrams of QQ1 and P2B in Longitudinal and Transverse Directions (Continued)

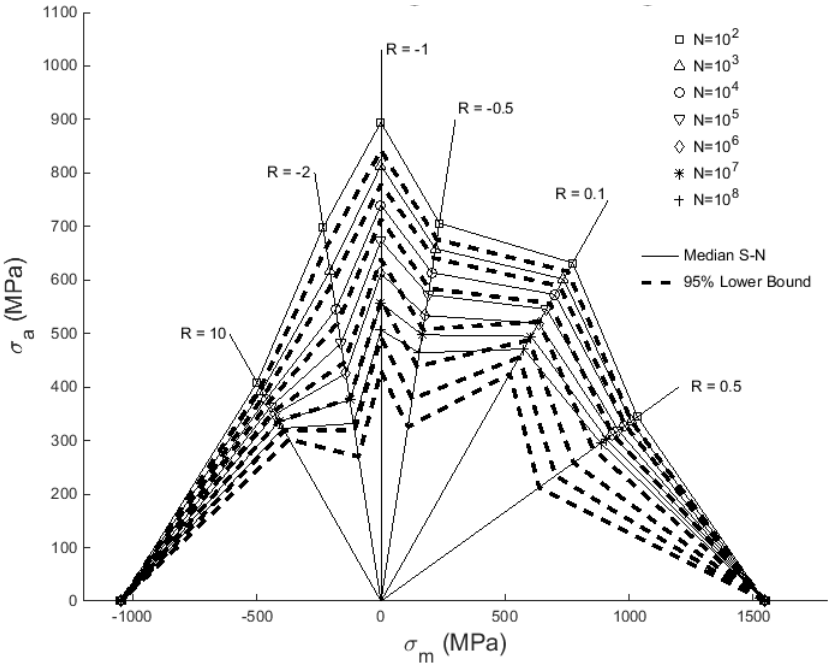

(c) Probabilistic constant life diagrams of P2B in longitudinal direction

Figure 2.8 Probabilistic Constant Life Diagrams of QQ1 and P2B in Longitudinal and Transverse Directions (Continued)

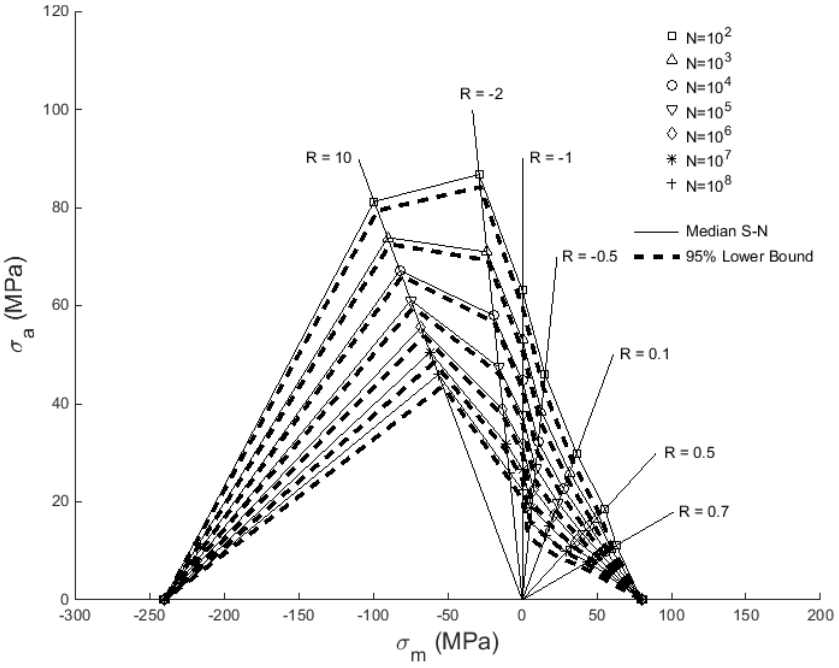

(d) Probabilistic constant life diagrams of P2B in transverse direction

Figure 2.8 Probabilistic Constant Life Diagrams of QQ1 and P2B in Longitudinal and Transverse Directions (Continued)

In order to account for the fatigue effect due to shear stress, CLD in the shear direction is necessary. However, fatigue test data for QQ1 and P2B in the shear direction are not available in the literature. To overcome a lack of test data for shear fatigue strength of composite materials, Philippidis and Vassilopoulos showed that shear fatigue strength values, which are calculated as 1/2.2 of the fatigue strength of a flat coupon cut off-axis at 45° and loaded uniaxially, adequately fit most of the experimental data (Philippidis and Vassilopoulos, 2002). Liu and Mahadevan considered the average value of the S-N curve slopes corresponding to the longitudinal and transverse directions tests as the slope of the S-N shear fatigue curve (Liu and Mahadevan, 2005). In this study, the shear fatigue strength is approximated by dividing the average fatigue strength in the

longitudinal and transverse directions by a constant. The constant is calculated based on static strength in three directions as shown in Table 2.3. In order to calculate this constant, two ratios are calculated first: the first ratio between the average of static tensile strength in the longitudinal and transverse directions and the static shear strength, and the second ratio between the average of static compressive strength in the longitudinal and transverse directions and the static shear strength. Then the average of these two ratios is used as the constant for constructing CLD for shear stress. The calculated constants for QQ1 and P2B are 3.4628 and 5.3157, respectively. The purpose of the shear strength approximation is to guarantee that the shear stress mean is equal to the static shear strength when the stress amplitude is zero in CLD. The calculated CLD of QQ1 and P2B in the shear direction is shown in Figure 2.9.

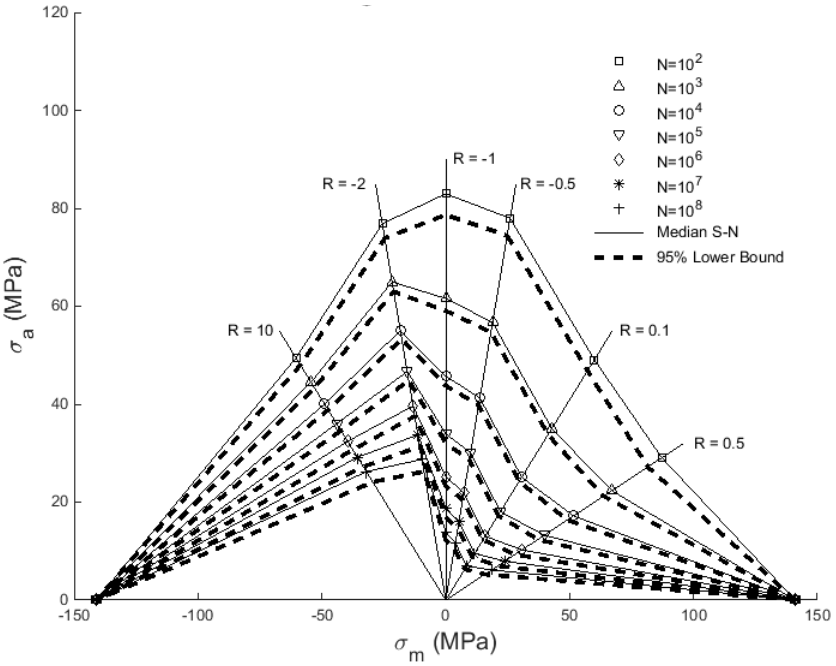

(a) Probabilistic constant life diagrams of QQ1 in shear direction

Figure 2.9 Probabilistic Constant Life Diagrams of QQ1 and P2B in Shear Direction

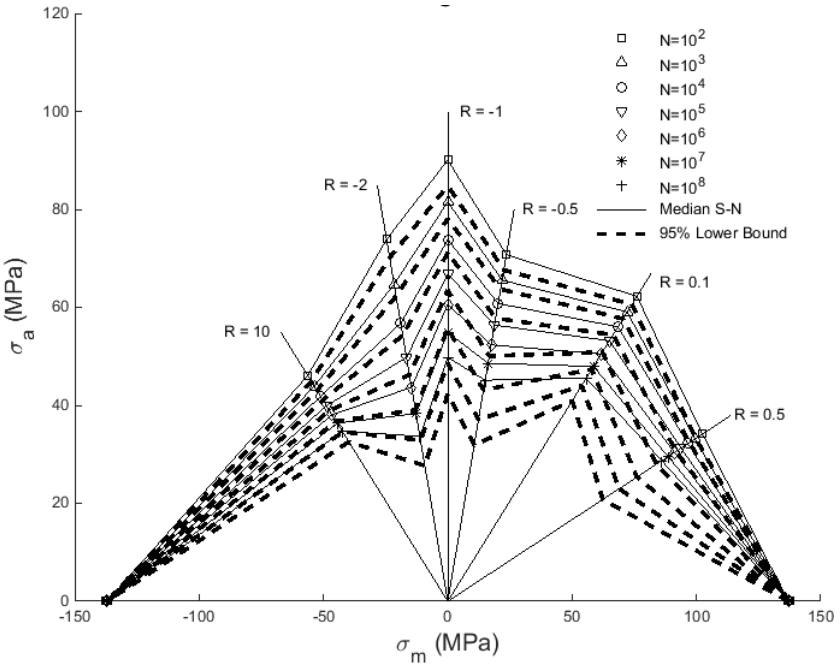

(b) Probabilistic constant life diagrams of P2B in shear direction

Figure 2.9 Probabilistic Constant Life Diagrams of QQ1 and P2B in Shear Direction (Continued)

2.3.5 Fatigue Damage Accumulation

The next step in the fatigue analysis is estimation of the fatigue damage accumulation, which is inherently nonlinear under variable-amplitude non-proportional multi-axial loading. The nonlinear damage accumulation methods for composite materials available in the literature (e.g., Gamstedt and Sjögren, 2002; Van Paepegem and Degrieck, 2002; Found and Quaresimin, 2003) are based on the experimental studies of specific laminated composite specimens under simple uniaxial loading conditions. Moreover, the applicability of these methods to different composite material systems and multi-axial loading conditions has not been established yet. At the same time, the most widely used method to predict fatigue damage of wind turbine blades assumes linear

damage accumulation (IEC 61400-1, 2005; Germanischer Lloyd, 2010). Fossum *et al.* assumed that Miner's sum gives close predictions when constant life diagrams tailored to fatigue experimental data are used (Fossum *et al.*, 2013). The fatigue damage in 10-minute simulation is accumulated using Miner's rule and Eq. (2.27) as

$$D_{10} = \sum_{i=1}^{n} D^i = 0.5 \sum_{i=1}^{n} \sqrt{\frac{1}{\left(N_{11}^i\right)^2} + \frac{1}{\left(N_{22}^i\right)^2} + \frac{1}{\left(N_{12}^i\right)^2} + \frac{1}{N_{11}^i N_{22}^i}} \tag{2.29}$$

where n is the total number of half cycles. This damage accumulation model is used in the present work.

The developed fatigue analysis procedure for composite wind turbine blades is summarized in Figure 2.10. In this study, the 10-minute fatigue damage D_{10} is essentially determined by a 10-minute mean wind speed V_{10} and a 10-minute turbulence intensity I_{10}, as shown in Figure 2.10. A 10-minute wind field is first generated based on V_{10} and I_{10}. Using the 10-minute wind field, the aerodynamic wind load in 10 minutes is calculated. Applying the aerodynamic wind load, the 10-minute fatigue damage is calculated for each node-section point on the blade FE model.

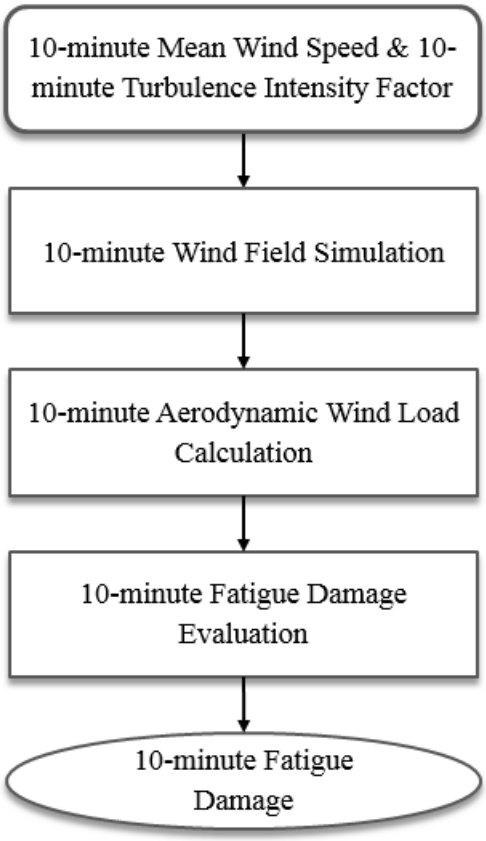

Figure 2.10 Ten-minute Fatigue Analysis Procedure

This chapter provides a 10-minute fatigue analysis procedure using a 10-minute mean wind speed V_{10} and a 10-minute turbulence intensity I_{10}. In reality, both the V_{10} and I_{10} are varying over a long time period, e.g., one year. Thus, the wind load is uncertain due to the varied V_{10} and I_{10}. In order to study the fatigue reliability of wind turbine blades in designed lifespan, the uncertain wind load has to be properly taken into account. Chapter 3 will address the issue of the wind load uncertainty.

CHAPTER 3

DYNAMIC WIND LOAD UNCERTAINTY MODEL

A dynamic wind load uncertainty model has been developed based on measured wind data. The wind load uncertainty model involves both the annual wind load variation and the wind load variation in a large spatiotemporal range, for example, in different years and at different locations. The annual wind load variation is represented by the joint probability density function (PDF) of 10-minute mean wind speed V_{10} and 10-minute turbulence intensity I_{10}. The wind load variation in a large spatiotemporal range is represented by the distributions of five marginal distribution and correlation parameters C, k, a, b, and τ, which determine the joint PDF of V_{10} and I_{10} as described in this chapter. The basic structure of the developed wind load uncertainty model is simply shown in Figure 3.1. The outline of this chapter is as follows. Section 3.1 presents the annual wind load variation by using the joint PDF of V_{10} and I_{10}. Section 3.2 provides the wind load variation in a large spatiotemporal range by using the PDFs of C, k, a, b, and τ. Discussion of a study case using the developed wind load uncertainty model is given in Section 3.3.

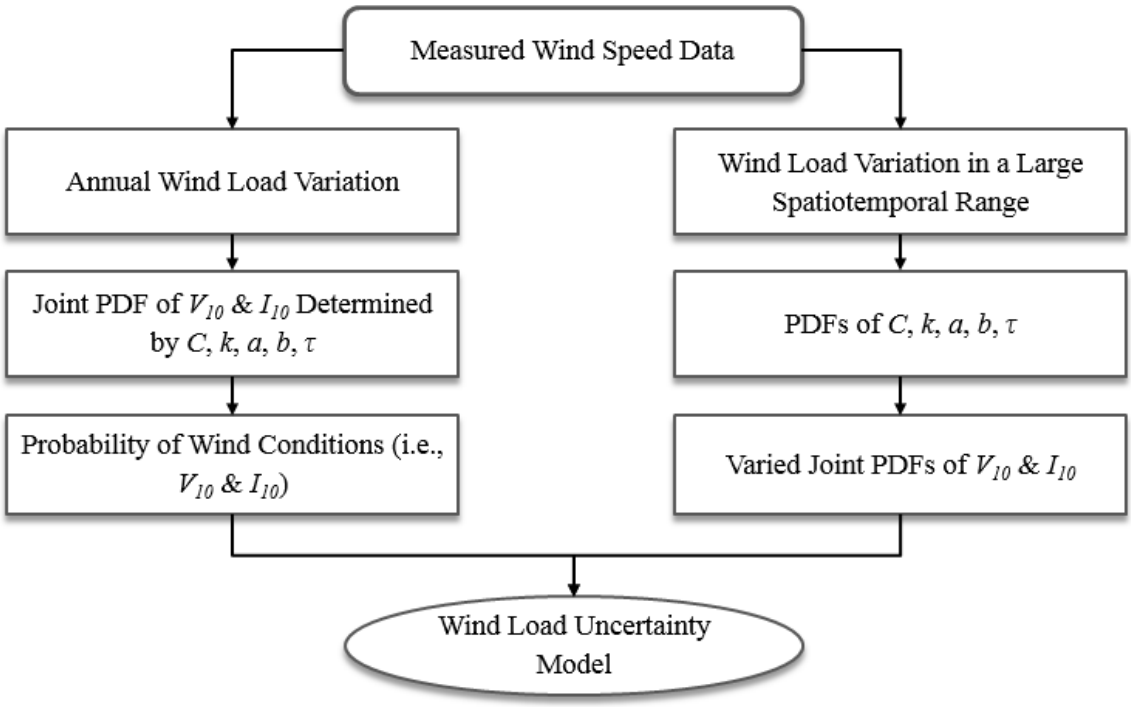

Figure 3.1 Developed Wind Load Uncertainty Model

3.1 Annual Wind Load Variation

In this study, the annual wind load variation means that the wind load under different wind conditions, which are determined by V_{10} and I_{10}, is varying due to the frequency of occurrence of the individual wind conditions in one year and at one location. The variable wind load is often represented by the variation of 10-minute mean wind speed, V_{10}, in the state-of-the-art wind energy standards (IEC 61400-1, 2005; Germanischer Lloyd, 2010). In this study, another factor, 10-minute turbulence intensity, I_{10}, which also affects fatigue damage during 10 minutes, is considered. Thus, the annual wind load variation is represented by the joint PDF of V_{10} and I_{10}. In addition, it is found that there is a correlation between V_{10} and I_{10}. In order to properly consider this correlation in the joint PDF of V_{10} and I_{10}, the 10-minute standard deviation Σ_{10} of wind

speed is used. This section will first provide the marginal distributions of the three random parameters for wind speed, i.e., V_{10}, I_{10}, and Σ_{10}. The correlation between these parameters is then studied by using copula (Noh *et al.*, 2009; Noh *et al.*, 2010; Lee *et al.*, 2011b). The joint distribution of V_{10} and I_{10} is derived using the copula for V_{10} and Σ_{10} and marginal distributions of V_{10} and Σ_{10}.

3.1.1 Marginal Distributions of Random Parameters for Wind Speed

The distribution of 10-minute mean wind speed V_{10} has been widely applied in fatigue analysis of wind turbines, while 10-minute turbulence intensity I_{10} is treated as a deterministic value based on wind energy standards (IEC 61400-1, 2005; Germanischer Lloyd, 2010) and its distribution has been seldom studied. As explained in Chapter 2, the 10-minute turbulence intensity I_{10} is calculated as a ratio between 10-minute standard deviation of wind speed Σ_{10} and 10-minute mean wind speed V_{10}. In order to properly derive the joint distribution of V_{10} and I_{10}, the marginal distribution of V_{10}, I_{10}, and Σ_{10} are first studied.

The probability distributions of V_{10}, I_{10}, and Σ_{10} are obtained using measured wind speed data. Before using the data, the wind speed data is first transformed to the same hub height from different measured heights, since the wind speed is inherently different at different heights. The hub height wind speed is calculated by a normal wind profile model (IEC 61400-1, 2005; Germanischer Lloyd, 2010) using the measured wind speed at other heights as

$$V_{hub} = \frac{V_z}{\left(z / z_{hub}\right)^{\alpha}} \tag{3.1}$$

where z is the measured height above the ground, z_{hub} is the hub height, and V_z is the measured wind speed at the height z. The power law exponent α is assumed to be 0.2 according to the standards (IEC 61400-1, 2005; Germanischer Lloyd, 2010). The

following distribution-identifying procedure is based on adjusted wind data at a hub height of 90 m.

The probability distributions of V_{10}, I_{10}, and Σ_{10} are fitted using seven different positive-valued distribution types, Gamma, Weibull, log-logistic, lognormal, Nakagami, Rayleigh, and Rician, provided in Matlab (MATLAB, 2012). The maximum likelihood estimation (MLE) is implemented to find parameters for fitting the candidate distributions (Hoog *et al.*, 2005). The likelihood function $L(\boldsymbol{\theta})$ and its natural logarithm $l(\boldsymbol{\theta})$ are, respectively, given by

$$L(\boldsymbol{\theta}) = \prod_{i=1}^{n} f(x_i; \boldsymbol{\theta}) \tag{3.2}$$

$$l(\boldsymbol{\theta}) = \sum_{i=1}^{n} \ln f(x_i; \boldsymbol{\theta}) \tag{3.3}$$

where $f(x_i;\boldsymbol{\theta})$ is the PDF value of a candidate distribution calculated at data x_i given the vector of distribution parameter $\boldsymbol{\theta}$. For each group of wind data, the distribution type corresponding to the largest log-likelihood value is viewed as the best fit distribution.

In total, 249 groups of measured wind data, which have been collected over different years and at different locations, are used in this study. These raw wind data are accessible online from Anemometer Loan Programs (Wind Data from Anemometer Loan Programs, URL: http://apps2.eere.energy.gov/wind/windexchange/anemometerloans/), UMass Wind Energy Center (Wind Data from the UMass Wind Energy Center, URL: http://www.umass.edu/windenergy/resourcedata), and the IAWind and Iowa EPSCoR data download site (Wind Data from IAWind and Iowa EPSCoR Data Download Site, URL: https://epscor2.cgrer.uiowa.edu/html/download.html). As an example, the distribution fit for V_{10} is illustrated by using one group of wind data from IAWind and Iowa EPSCoR data. The wind data was measured by an anemometer at 100 m in Quimby, Iowa. The measured time ranges from 4/6/2007 to 4/7/2009. The raw wind data

records the 10-minute mean wind speed and 10-minute standard deviation of wind speed. The 90 m hub height wind speed is calculated by Eq. (3.1) using the measured wind speed at 100 m. The distribution fit of V_{10} is shown in Figure 3.2. The values of the log-likelihood functions of the seven distribution candidates are shown in Table 3.1.

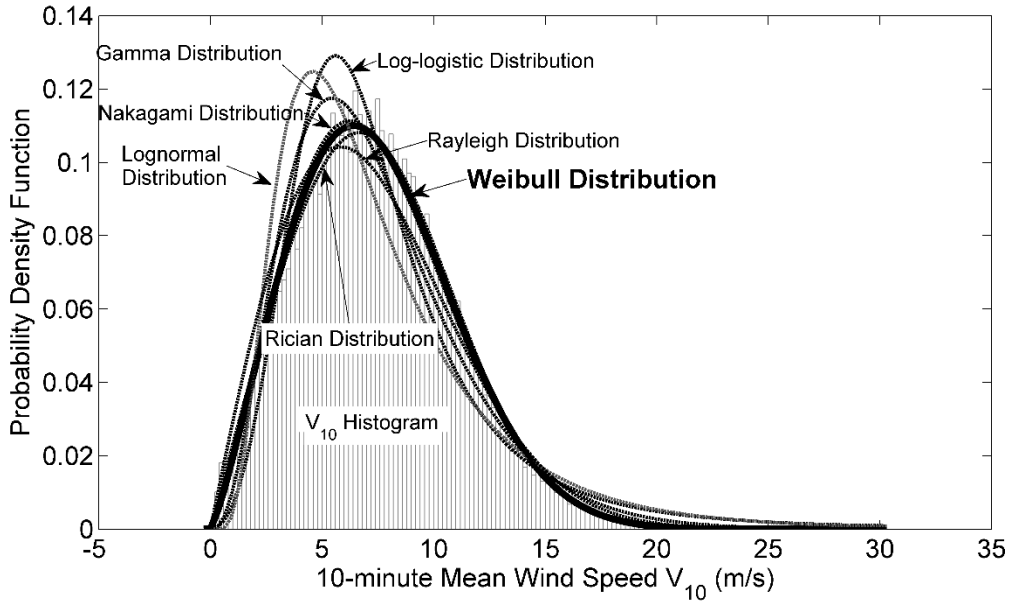

Figure 3.2 Distribution Fit of V_{10}

Table 3.1 Log-likelihood of the Candidate Distribution Types for V_{10}

Distribution Type	Log-likelihood
Gamma	−275722
Weibull	**−273161**
Log-logistic	−279939
Lognormal	−284159
Nakagami	−273244
Rayleigh	−274070
Rician	−273179

As shown in Table 3.1, the Weibull distribution fit for V_{10} has the largest log-likelihood function value among the seven candidate distribution types. Thus the Weibull distribution is selected for the annual V_{10} distribution, which is consistent with the fact that the Weibull distribution has been widely accepted for representing the annual mean wind speed distribution. Similarly, using the MLE, the best marginal distribution types of I_{10} and Σ_{10} have been identified as a log-logistic distribution type and a Gamma distribution type, respectively. In fact, among 249 groups of wind data, there are 46, 163, and 120 groups of wind data best fit by the Weibull distribution for V_{10}, the log-logistic distribution for I_{10}, and the Gamma distribution for Σ_{10}, respectively. Thus, the annual distribution types for V_{10}, I_{10}, and Σ_{10} are selected to be Weibull, log-logistic, and Gamma, respectively. The PDF of the Weibull distribution of V_{10} is given by

$$f_{V10}\left(v_{10};C,k\right)=\frac{k}{C}\left(\frac{v_{10}}{C}\right)^{k-1}\exp\left[-\left(\frac{v_{10}}{C}\right)^{k}\right] \tag{3.4}$$

where v_{10} is a realization of V_{10}, and C and k are the scale parameter and shape parameter, respectively. The PDF of the log-logistic distribution of I_{10} is given by

$$f_{I10}\left(i_{10};\gamma,\delta\right)=\frac{\exp\left(\frac{\ln i_{10}-\gamma}{\delta}\right)}{\delta i_{10}\left[1+\exp\left(\frac{\ln i_{10}-\gamma}{\delta}\right)\right]^2} \tag{3.5}$$

where i_{10} is a realization of I_{10}, and γ and δ are the log-location parameter and log-scale parameter, respectively. ln i_{10} is the natural logarithm of i_{10}. The PDF of the Gamma distribution of Σ_{10} is given by

$$f_{\Sigma 10}\left(\sigma_{10};a,b\right)=\frac{1}{b^a\Gamma\left(a\right)}\sigma_{10}^{a-1}\exp\left(-\frac{\sigma_{10}}{b}\right) \tag{3.6}$$

where σ_{10} is a realization of Σ_{10}, and a and b are the shape parameter and scale parameter, respectively. $\Gamma(a)$ is the gamma function of a.

So far, the marginal distribution types of the random parameters V_{10}, I_{10}, and Σ_{10} have been identified as the Weibull distribution, log-logistic distribution, and Gamma distribution, respectively. The Weibull distribution of V_{10} characterizes the 10-minute mean wind speed variation during the year, while the log-logistic distribution of I_{10} and the Gamma distribution of Σ_{10} represent the variation of fluctuation in wind speed in 10 minutes. It is useful to think of the wind as consisting of a mean wind speed with turbulent fluctuations superimposed. The mean wind speed and turbulence intensity are often used to represent the wind load strength/level by wind turbine design standards (IEC 61400-1, 2005; Germanischer Lloyd, 2010). In this study, V_{10} and I_{10} deterministically determine the 10-minute fatigue damage with the developed fatigue damage analysis procedure in Chapter 2. However, it is found that using V_{10} and Σ_{10} could better represent the correlated joint PDF of V_{10} and I_{10}. The correlation between V_{10} and I_{10} and the correlation between V_{10} and Σ_{10} will be discussed in the next section.

3.1.2 Correlation between Random Parameters for Wind Speed

In order to calculate the probability of a certain wind condition, i.e., V_{10} and I_{10}, in one year, the joint PDF of V_{10} and I_{10} is necessary. If the random variables V_{10} and I_{10} are assumed to be independent, the joint PDF of V_{10} and I_{10} can be simply calculated as

$$f_{VI} = f_{V10} \cdot f_{I10} \tag{3.7}$$

where f_{VI0} and f_{I10} are the marginal PDFs of V_{10} and I_{10}, respectively. However, the scatter plots of (V_{10}, I_{10}) and (V_{10}, Σ_{10}) in Figure 3.3 clearly show that there are correlations among these three random parameters. The wind data in Figure 3.3 was measured at Thompson Island, Boston Harbor, Massachusetts. The measured time ranges from 01/01/2008 to 12/31/2008. The measured data is obtained from the UMass Wind Energy Center (URL: http://www.umass.edu/windenergy/resourcedata).

For bivariate correlated input random variables $\mathbf{X} = \{X_i, X_j\}^{\mathrm{T}}$, the joint PDF of $\mathbf{X}$ can be expressed using copula as (Noh *et al.*, 2009; Noh *et al.*, 2010; Lee *et al.*, 2011b)

$$\begin{aligned} f_{\mathbf{X}}(\mathbf{x};\boldsymbol{\mu}) &= \frac{\partial^2 C(u,v;\theta)}{\partial u \partial v} f_{X_i}(x_i;\mu_i) f_{X_j}(x_j;\mu_j) \\ &= C_{,uv}(u,v;\theta) f_{X_i}(x_i;\mu_i) f_{X_j}(x_j;\mu_j) \end{aligned} \tag{3.8}$$

where C is the copula function; f_{Xi} and f_{Xj} are the marginal PDFs for X_i and X_j, respectively; $u=F_{Xi}(x_i;\mu_i)$ and $v=F_{Xj}(x_j;\mu_j)$ are marginal CDFs for X_i and X_j, respectively; and θ is the correlation coefficient between X_i and X_j. The partial derivative of the copula function with respect to u and v is called the copula density function and is written as

$$c(u,v;\theta) \equiv \frac{\partial^2 C(u,v;\theta)}{\partial u \partial v} = C_{,uv}(u,v;\theta) \tag{3.9}$$

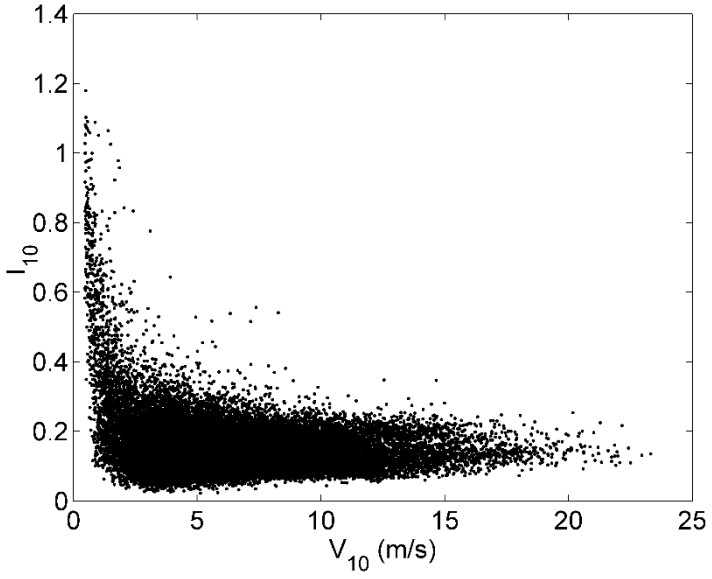

(a) Scatter plot of one group of measured V_{10} and I_{10}

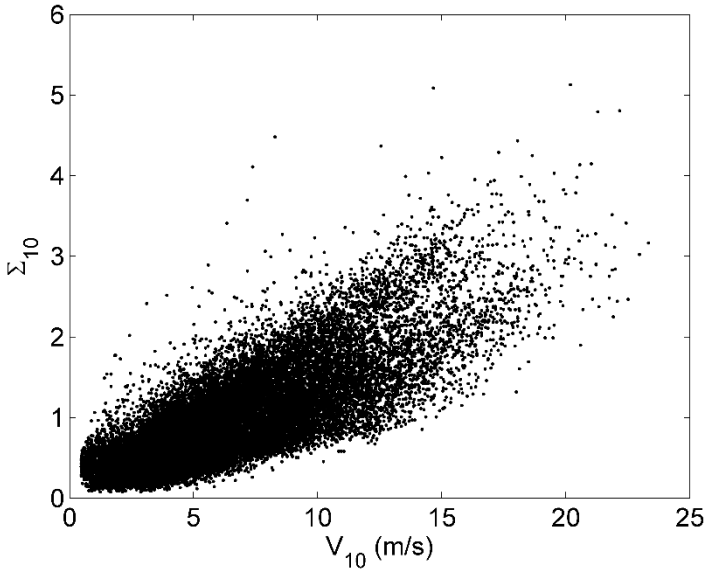

(b) Scatter plot of one group of measured V_{10} and Σ_{10}

Figure 3.3 Scatter Plot of Measured (V_{10}, I_{10}) and (V_{10}, Σ_{10})

In order to include the correlation between V_{10} and I_{10}, two methods have been studied. One method is directly identifying the copula of V_{10} and I_{10}. Then the joint PDF of V_{10} and I_{10} is calculated as

$$f_{VI}\left(v_{10}, i_{10}; C, k, \gamma, \delta, \theta_{VI}\right) = c_{VI}\left(v_{10}, i_{10}; \theta_{VI}\right) f_{V10}\left(v_{10}; C, k\right) f_{I10}\left(i_{10}; \gamma, \delta\right) \tag{3.10}$$

where c_{VI} is the copula density function of V_{10} and I_{10}, and θ_{VI} is the correlation coefficient between V_{10} and I_{10} for the copula. The other method is to first identify the joint PDF of V_{10} and Σ_{10} and then calculate the joint PDF of V_{10} and I_{10} using the joint PDF of V_{10} and Σ_{10}.

Before identifying copula types, Monte Carlo simulation (MCS) samples of V_{10} and I_{10} have been generated according to a joint PDF of V_{10} and I_{10} and a joint PDF of V_{10} and Σ_{10}, respectively. The copula type for V_{10} and I_{10} and the copula type for V_{10} and Σ_{10} are assumed to be Gaussian. The parameters for marginal distribution and the correlation coefficient are calculated by MLE, which uses the data for Figure 3.3. For the latter approach, the MCS samples of V_{10} and Σ_{10} are first generated based on their joint PDF. Then the I_{10} values are calculated by $I_{10} = \Sigma_{10} / V_{10}$ using the MCS samples of V_{10} and Σ_{10}. The scatter plots of MCS samples of V_{10} and I_{10}, using the two methods, are shown in Figure 3.4.

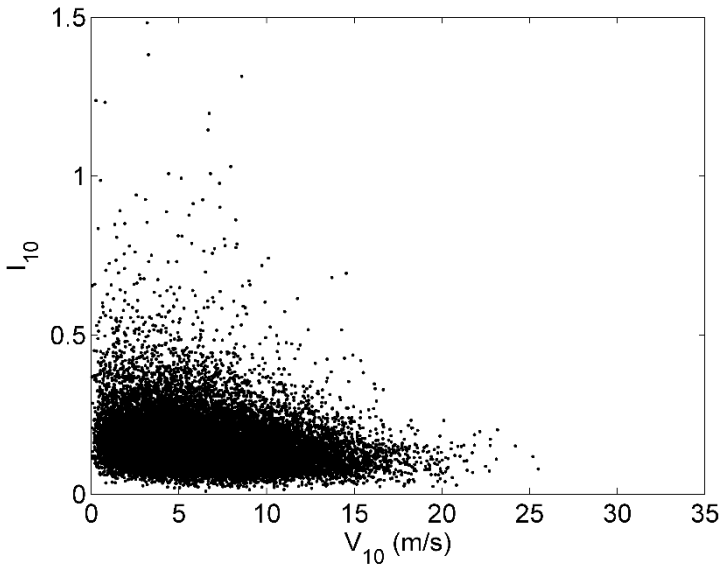

(a) MCS samples of V_{10} and I_{10} using a Gaussian copula between V_{10} and I_{10}

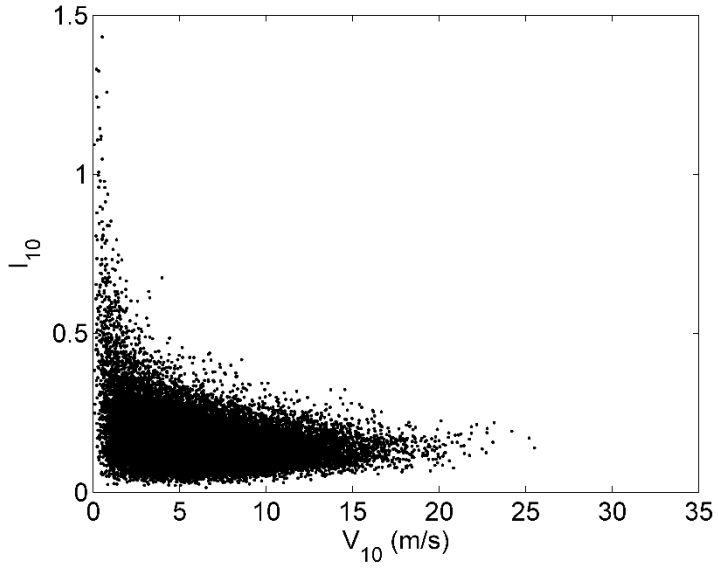

(b) MCS samples of V_{10} and I_{10} using a Gaussian copula between V_{10} and Σ_{10}

Figure 3.4 Scatter Plot of MCS Samples of V_{10} and I_{10}

It can be seen that the scatter plot of MCS samples using the joint PDF of V_{10} and Σ_{10} (Figure 3.4(b)) is closer to that of measured V_{10} and I_{10} (Figure 3.3(a)) than that using the joint PDF of V_{10} and I_{10} (Figure 3.4(a)). The reason might be that extra mathematical correlation between V_{10} and I_{10} is inherently included from the relation $I_{10} = \Sigma_{10} / V_{10}$. In contrast, the V_{10} and Σ_{10} data are directly obtained from the measured wind data. To exclude the mathematical correlation in the joint PDF, it is better to derive the joint PDF of V_{10} and Σ_{10} and then transfer them to V_{10} and I_{10}. This derivation is shown in the following.

For brevity, the marginal distribution parameters and copula parameter are omitted in the following derivation. Using the copula density function, the joint PDF of V_{10} and I_{10} and the joint PDF of V_{10} and Σ_{10} are expressed, respectively, as

$$f_{VI}\left(v_{10}, i_{10}\right) = c_{VI}\left(v_{10}, i_{10}\right) f_{V10}\left(v_{10}\right) f_{I10}\left(i_{10}\right) \tag{3.11}$$

$$f_{V\Sigma}\left(v_{10}, \sigma_{10}\right) = c_{V\Sigma}\left(v_{10}, \sigma_{10}\right) f_{V10}\left(v_{10}\right) f_{\Sigma 10}\left(\sigma_{10}\right) \tag{3.12}$$

where v_{10}, i_{10}, and σ_{10} are realizations of random variables V_{10}, I_{10}, and Σ_{10}, respectively. Using Eqs. (3.11) and (3.12), the conditional distributions of I_{10} and Σ_{10}, given that V_{10} equals a realization v_{10}, can be calculated, respectively, as

$$f_{I|V}\left(i_{10} \mid v_{10}\right) = \frac{f_{VI}\left(v_{10}, i_{10}\right)}{f_{V10}\left(v_{10}\right)} = c_{VI}\left(v_{10}, i_{10}\right) f_{I10}\left(i_{10}\right) \tag{3.13}$$

$$f_{\Sigma|V}\left(\sigma_{10} \mid v_{10}\right) = \frac{f_{V\Sigma}\left(v_{10}, \sigma_{10}\right)}{f_{V10}\left(v_{10}\right)} = c_{V\Sigma}\left(v_{10}, \sigma_{10}\right) f_{\Sigma 10}\left(\sigma_{10}\right) \tag{3.14}$$

Given $V_{10} = v_{10}$, the function $I_{10} = \Sigma_{10} / v_{10}$ defines a one-to-one transformation with Jacobian $J=|(\partial \Sigma_{10})/(\partial I_{10})|=v_{10}$. Thus, the conditional distribution of I_{10} given $V_{10} = v_{10}$ can also be expressed as

$$f_{I|V}\left(i_{10} \mid v_{10}\right) = f_{\Sigma|V}\left(\sigma_{10} \mid v_{10}\right)\left|J\right| = f_{\Sigma|V}\left(\sigma_{10} \mid v_{10}\right) v_{10} \tag{3.15}$$

From Eqs. (3.13) to (3.15), we have

$$c_{VI}\left(v_{10},i_{10}\right)f_{I10}\left(i_{10}\right)=c_{V\Sigma}\left(v_{10},\sigma_{10}\right)f_{\Sigma 10}\left(\sigma_{10}\right)v_{10}=c_{V\Sigma}\left(v_{10},v_{10}\cdot i_{10}\right)f_{\Sigma 10}\left(v_{10}\cdot i_{10}\right)v_{10} \quad (3.16)$$

Substituting Eq. (3.16) into Eq. (3.11), we have the joint PDF of V_{10} and I_{10} as

$$f_{VI}\left(v_{10},i_{10}\right)=c_{V\Sigma}\left(v_{10},v_{10}\cdot i_{10}\right)f_{V10}\left(v_{10}\right)f_{\Sigma 10}\left(v_{10}\cdot i_{10}\right)v_{10} \quad (3.17)$$

In Section 3.1.1, the marginal distribution types for V_{10} and Σ_{10} are found to be Weibull and Gamma, respectively. Therefore, type of copula density function $c_{V\Sigma}$ is the only unknown term in Eq. (3.17). In order to select the best copula type for $c_{V\Sigma}$, the best copula type among eight candidate copula types has been identified for all 249 groups of wind data. The number of best fit copula for each copula type is shown in Table 3.2.

Table 3.2 Number of Best Fit Copula Type for V_{10} and Σ_{10}

Copula Type	Number of Best Copula
Clayton	0
AMH	0
Gumbel	**147**
Frank	18
A12	1
A14	6
FGM	0
Gaussian	77
Independent	0

As shown in Table 3.2, the copula type corresponding to the largest number of best fit copula type for V_{10} and Σ_{10} is Gumbel. Thus, the Gumbel copula is selected to account for the correlation between V_{10} and Σ_{10}. The Gumbel copula function and copula density function are shown, respectively, as (Noh *et al.*, 2010),

$$C_{V\Sigma}\left(u,v;\theta\right)=\exp\left(-w^{1/\theta}\right) \tag{3.18}$$

$$c_{V\Sigma}\left(u,v;\theta\right)=\frac{\left(-\ln u\right)^{\theta-1}\left(-\ln v\right)^{\theta-1}\left(\theta+w^{1/\theta}-1\right)w^{1/\theta-2}\exp\left(-w^{1/\theta}\right)}{uv} \tag{3.19}$$

where u and v are marginal CDFs of V_{10} and Σ_{10}, respectively. The parameter w is calculated as

$$w=\left(-\ln u\right)^{\theta}+\left(-\ln v\right)^{\theta} \tag{3.20}$$

Copula parameter θ can be calculated from Kendall's tau τ as (Noh *et al.*, 2010)

$$\theta=1/\left(1-\tau\right) \tag{3.21}$$

With the marginal distribution parameters and the Kendall's tau τ, the joint PDF of V_{10} and I_{10} in Eq. (3.17) can be represented as

$$f_{VI}\left(v_{10},i_{10};C,k,a,b,\tau\right)=c_{V\Sigma}\left(v_{10},v_{10}\cdot i_{10};\tau\right)f_{V10}\left(v_{10};C,k\right)f_{\Sigma 10}\left(v_{10}\cdot i_{10};a,b\right)v_{10} \tag{3.22}$$

where C and k are the scale parameter and shape parameter, respectively, for the Weibull distribution; a and b are the shape parameter and scale parameter, respectively, for the Gamma distribution; and the PDFs of the Weibull distribution and the Gamma distribution are shown in Eqs. (3.4) and (3.6), respectively. The Kendall's tau τ determines the correlation parameter θ as shown in Eq. (3.21).

Applying the derived joint PDF of V_{10} and I_{10}, the one-year fatigue damage can be calculated as

$$\begin{aligned}D_{1year}\left(\mathbf{d},C,k,a,b,\tau\right)&=52560\int_{V_{low}}^{V_{upp}}\int_{I_{low}}^{I_{upp}}f_{VI}\left(v_{10},i_{10};C,k,a,b,\tau\right)D_{10}\left(\mathbf{d},v_{10},i_{10}\right)\mathrm{d}v_{10}\mathrm{d}i_{10}\\&=52560\int_{V_{low}}^{V_{upp}}\int_{I_{low}}^{I_{upp}}c_{V\Sigma}\left(v_{10},v_{10}\cdot i_{10};\tau\right)f_{V10}\left(v_{10};C,k\right)f_{\Sigma 10}\left(v_{10}\cdot i_{10};a,b\right)v_{10}D_{10}\left(\mathbf{d},v_{10},i_{10}\right)\mathrm{d}v_{10}\mathrm{d}i_{10}\end{aligned} \tag{3.23}$$

where **d** is design vector of laminate thickness; C and k are the scale parameter and shape parameter for the Weibull distribution, respectively; a and b are the shape parameter and scale parameter for the Gamma distribution, respectively; τ is the Kendall's tau for V_{10} and Σ_{10}; $c_{V\Sigma}$ is the Gumbel copula for V_{10} and Σ_{10}; f_{V10} and $f_{\Sigma 10}$ are the Weibull PDF and

Gamma PDF of V_{10} and Σ_{10}, respectively; V_{low} and V_{upp} are the lower and upper bounds of V_{10}, respectively; and I_{low} and I_{upp} are the lower and upper bounds of I_{10}, respectively. D_{10} is the 10-minute fatigue damage. The fatigue analysis procedure for calculating D_{10} is explained in Chapter 2 in detail.

3.2 Wind Load Variation in a Large Spatiotemporal Range

Section 3.1 provides a joint PDF of V_{10} and I_{10} to account for the wind load variation during one year at a specific location. However, the wind load is also varying year-to-year for a specific location. In addition, the wind load could be different at different locations for various reasons, e.g., the non-uniformity of the earth's surface, or the thermal effect due to differences in altitude. Even though the variation of wind load in a large spatiotemporal range seems unpredictable, the distributions and correlation type of the random wind parameters, V_{10}, I_{10}, and Σ_{10}, are assumed to be the same. For example, researchers often use a Weibull distribution to represent the mean wind speed distribution, disregarding when or where their fatigue research has been done (Burton *et al.*, 2011; Germanischer Lloyd, 2010; Griffith and Ashwill, 2011; IEC 61400-1, 2005; Manwell *et al.*, 2009; Ronold *et al.*, 1999; Shokrieh and Rafiee, 2006). In this study, the wind load variation in a large spatiotemporal range is represented by the distributions of the marginal distribution and correlation parameters, i.e., C, k, a, b, and τ, which determine the joint PDF of V_{10} and I_{10} in Eq. (3.22).

Using the 249 groups of wind data measured from different years and at different locations, 249 sets of (C, k, a, b, τ) values have been calculated. Then marginal distribution types of C, k, a, b, and τ can be identified using the same MLE method as explained in Section 3.1.1. The log-likelihood function values for each candidate marginal distribution type are shown in Table 3.3.

Table 3.3 Log-likelihood of Candidate Distribution Types for C, k, a, b, and τ

Log-likelihood	C	k	a	b	τ
Normal	−460.133	**−11.273**	−387.513	254.044	159.332
Lognormal	−453.771	−15.152	−363.056	241.609	104.754
Nakagami	−456.276	−11.859	−375.722	253.001	143.410
Rayleigh	−609.626	−276.748	−433.955	182.445	64.433
Rician	−459.954	−11.276	−385.881	254.192	158.377
Gamma	−453.967	−13.002	−368.133	248.462	127.085
Weibull	−475.839	−21.236	−389.089	**257.120**	169.065
Birnbaum-Sauuders	−454.220	−15.504	−362.710	241.967	100.490
Exponential	−768.942	−444.336	−571.864	39.0837	−82.406
Extreme Value	−506.790	−32.078	−438.082	245.713	**182.775**
Generalized Extreme Value	−453.698	−11.529	**−360.704**	256.163	179.529
Inverse Gaussian	−454.232	−15.521	−362.563	241.583	99.271
Log-logistic	**−448.182**	−12.170	−367.678	236.993	129.781
Logistic	−452.829	−12.667	−385.336	245.866	164.481

As shown in Table 3.3, the largest log-likelihood values for C, k, a, b, and τ correspond to log-logistic distribution, normal distribution, generalized extreme value distribution, Weibull distribution, and extreme value distribution, respectively. After calculating the distribution parameters using MLE, the specific PDFs of random parameters C, k, a, b, and τ can be obtained. The best fit distributions for C, k, a, b, and τ are shown in Figure 3.5. The PDFs of C, k, a, b, and τ are listed in Table 3.4.

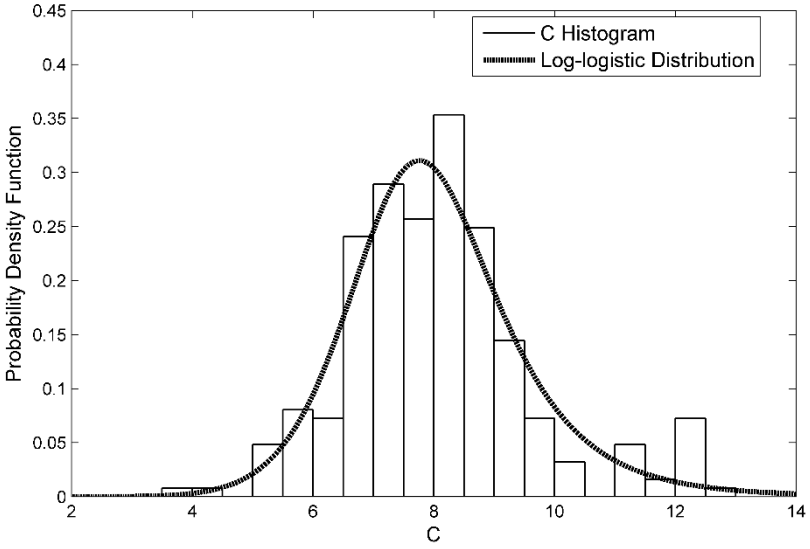

(a) Log-logistic distribution fit for *C* data

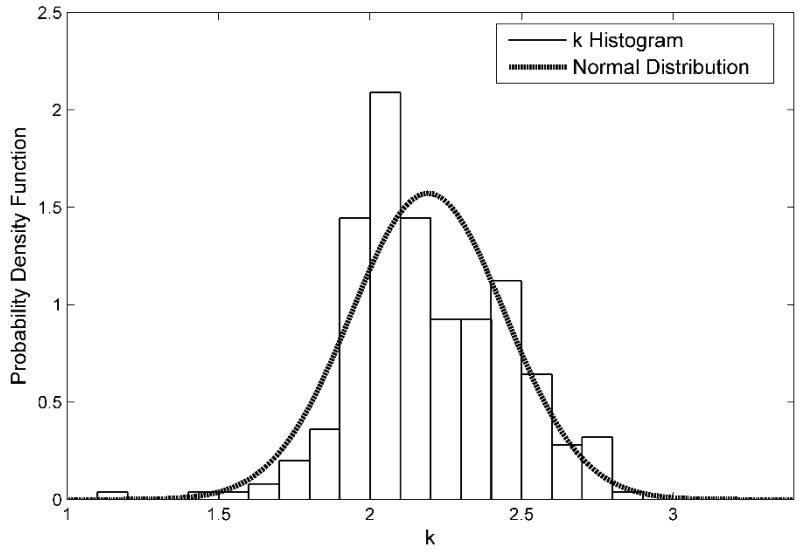

(b) Normal distribution fit for *k* data

Figure 3.5 Best Fit Distributions for *C*, *k*, *a*, *b*, τ

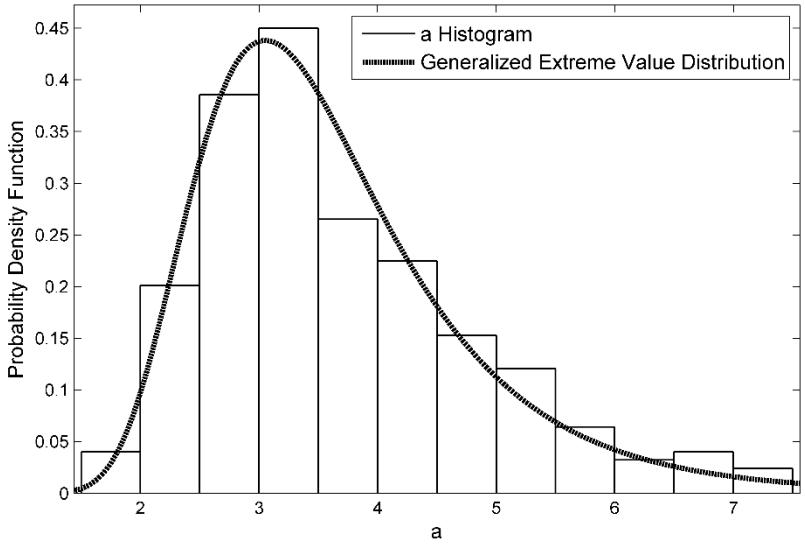

(c) Generalized extreme value distribution fit for *a* data

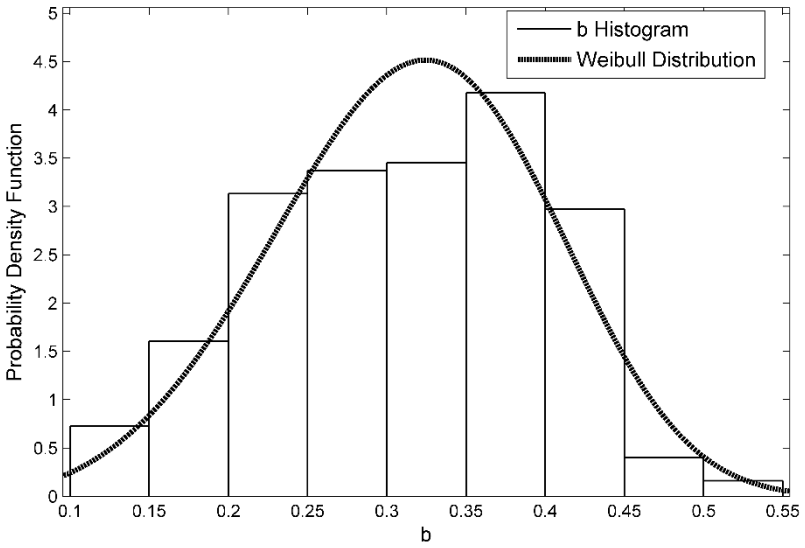

(d) Weibull distribution fit for *b* data

Figure 3.5 Best Fit Distributions for *C*, *k*, *a*, *b*, τ (Continued)

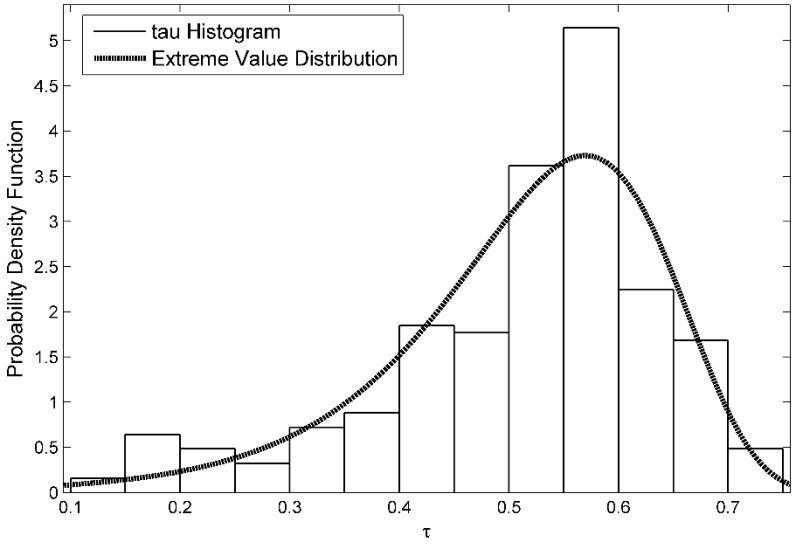

(e) Extreme value distribution fit for τ data

Figure 3.5 Best Fit Distributions for C, k, a, b, τ (Continued)

Table 3.4 Identified PDFs of C, k, a, b, τ Using 249 Groups of Wind Data

Parameter	Distribution Type	PDF
C	Log-logistic	$f_C(x) = \dfrac{\exp\left[\dfrac{\ln(x) - 2.0701}{0.1024}\right]}{0.1024x\left[1+\exp\left(\dfrac{\ln(x) - 2.0701}{0.1024}\right)\right]^2}$
k	Normal	$f_k(x) = \dfrac{1}{0.2532\sqrt{2\pi}}\exp\left[\dfrac{-(x-2.1913)^2}{0.1282}\right]$
a	Generalized Extreme Value	$f_a(x) = 1.1888\dfrac{(0.7429+0.0827x)^{-15.3746}}{\exp\left[(0.7429+0.0827x)^{-14.3746}\right]}$
b	Weibull	$f_b(x) = \dfrac{4.1254}{0.3470}\left(\dfrac{x}{0.3470}\right)^{3.1254}\exp\left[-\left(\dfrac{x}{0.3470}\right)^{4.1254}\right]$
τ	Extreme Value	$f_\tau(x) = 0.0986^{-1}\exp\left(\dfrac{x-0.5696}{0.0986}\right)\exp\left[-\exp\left(\dfrac{x-0.5696}{0.0986}\right)\right]$

3.3 Case Study and Discussion

The composite wind turbine blade model developed in Chapter 2 is used as a case study to demonstrate the influence of wind load uncertainty on blade fatigue life prediction. In this example, the annual wind load variation is represented by the joint PDF of V_{10} and I_{10}, which is determined by parameters (C, k, a, b, τ) as shown in Eq. (3.22). The one-year fatigue damage is calculated using Eq. (3.23). In order to illustrate the effect of wind load variation in a large spatiotemporal range, two sets of (C, k, a, b, τ) are randomly selected from the 249 sets, which are based on measured wind data. The two sets of (C, k, a, b, τ) are C = 6.5856, k = 2.5178, a =3.1570, b = 0.4123, τ = 0.6826, and C = 4.2878, k = 1.9156, a = 3.7330, b = 0.3834, τ = 0.7272, respectively. The corresponding joint PDFs of V_{10} and I_{10} are called joint PDF 1 and joint PDF 2 and are shown in Figure 3.6. The lower bound and upper bound of V_{10} are 3 m/s and 25 m/s, respectively. The lower bound and upper bound of I_{10} are 0.02 and 1, respectively. The 10-minute fatigue analyses are run over the range of V_{10} between 3 m/s and 25 m/s in 2 m/s increments, and the range of I_{10} between 0.02 and 1 in 0.02 increments.

As can be seen in Figure 3.6 (b), the most probable wind condition, which has the largest probability equal to 0.0453 using joint PDF 1, is located at V_{10} = 7 m/s, I_{10} = 0.22. Figure 3.6 (d) show that the most probable wind condition, which has the largest probability equal to 0.0359 using joint PDF 2, is located at V_{10} = 3 m/s, I_{10} = 0.36. Because the cut-in wind speed, i.e., the lower bound of V_{10}, is equal to 3 m/s, the wind load corresponding to V_{10} smaller than 3 m/s is assumed to contribute no fatigue damage. The maximum fatigue damage of section points through laminate thickness is used to represent the damage for the corresponding finite element (FE) node. The one-year fatigue damage contours corresponding to joint PDFs 1 and 2 are shown in Figure 3.7.

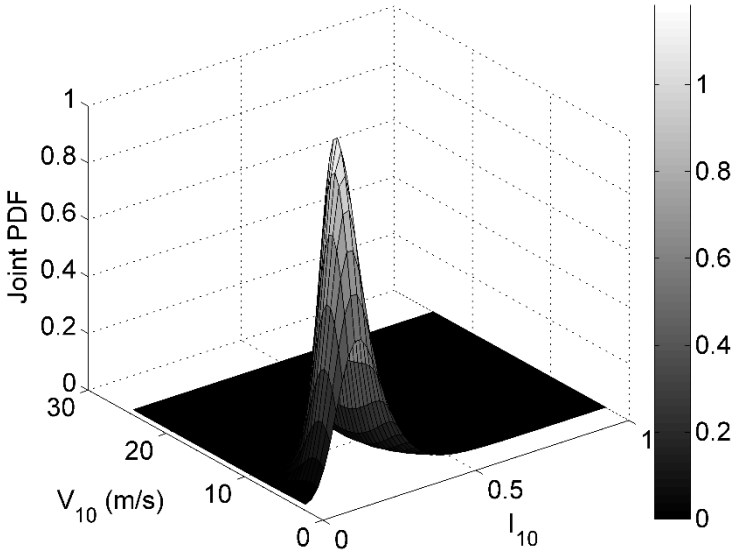

(a) Stereoscopic view of joint PDF 1

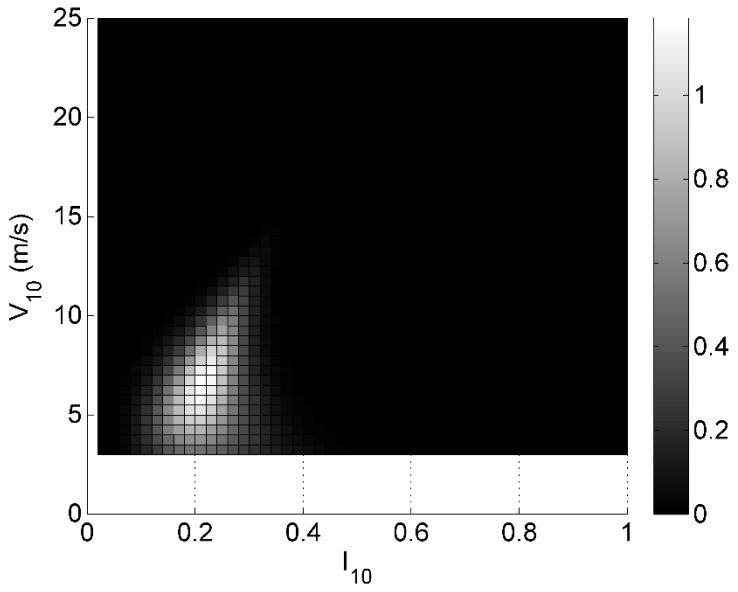

(b) Top view of joint PDF 1

Figure 3.6 Two Joint PDFs Used in Fatigue Damage Calculation

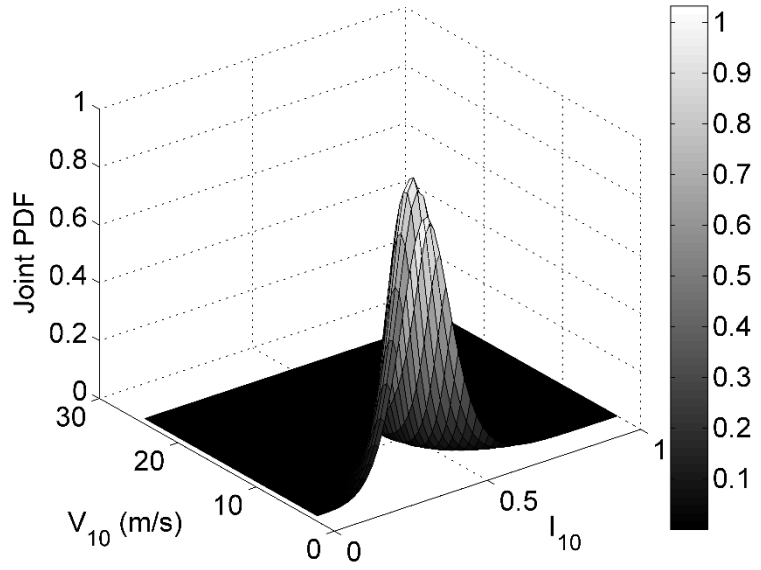

(c) Stereoscopic view of joint PDF 2

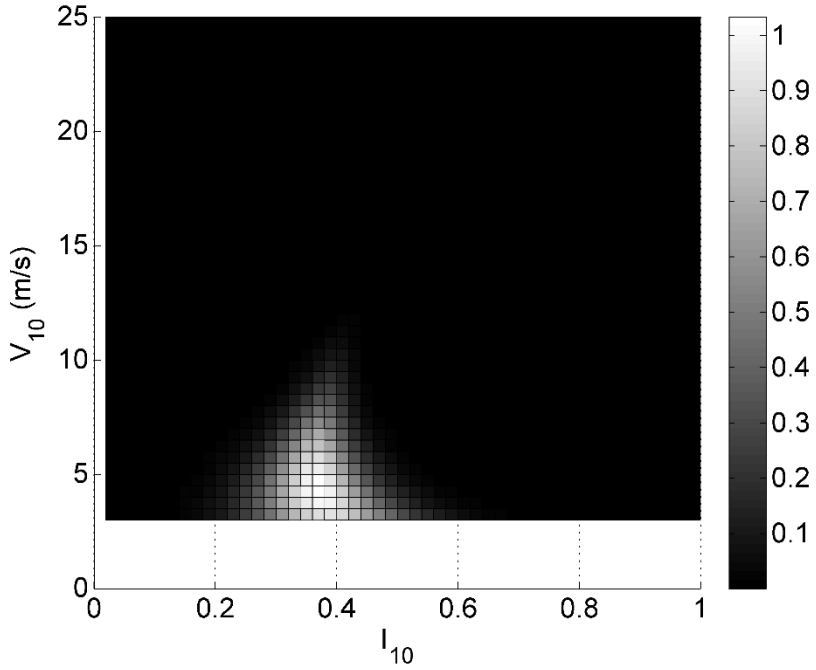

(d) Top view of joint PDF 2

Figure 3.6 Two Joint PDFs Used in Fatigue Damage Calculation (Continued)

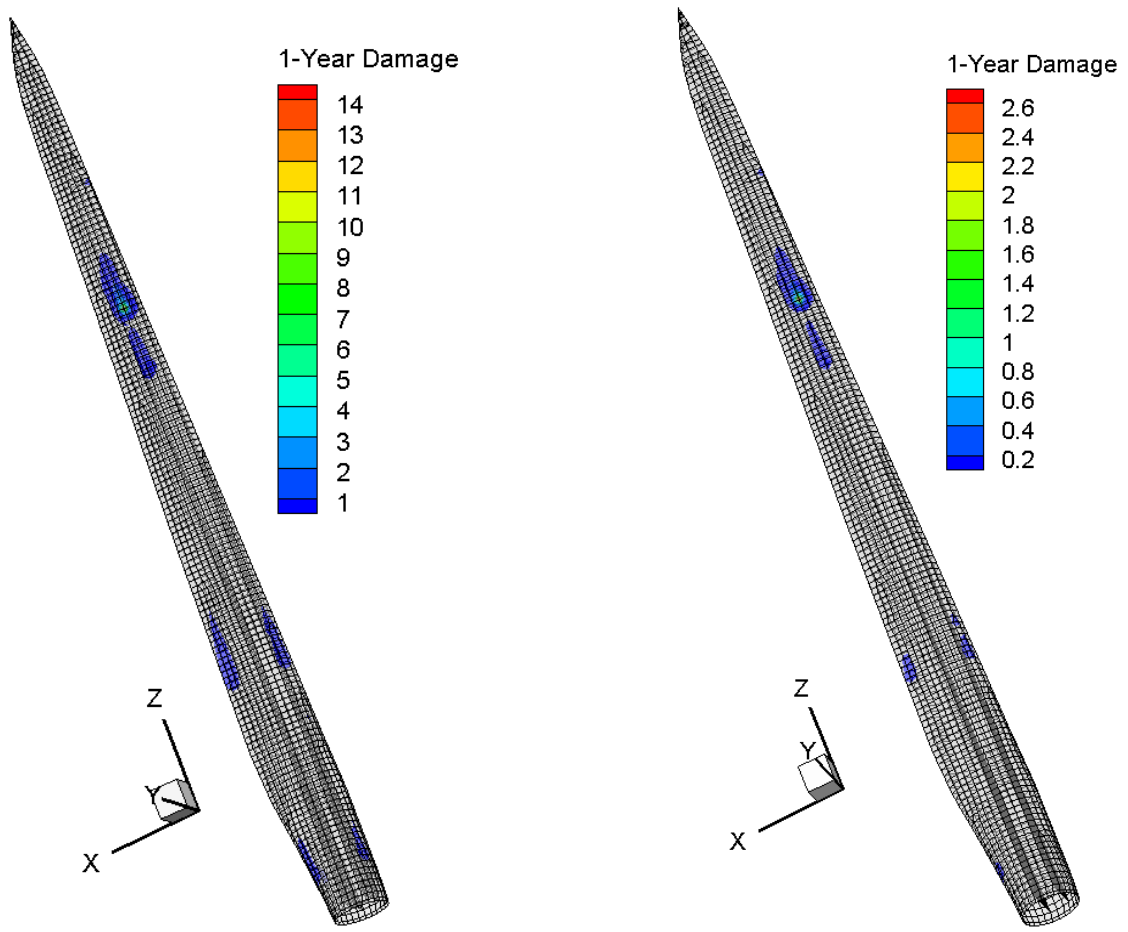

(a) Fatigue contour using joint PDF 1 (b) Fatigue contour using joint PDF 2

Figure 3.7 One-year Fatigue Damage Contours Generated by Using Two Joint PDFs

It can be seen that the distributions of the fatigue-critical areas for the cases of joint PDFs 1 and 2 are similar, but accumulated fatigue damages are different. The maximum one-year fatigue damage for the case of joint PDF 1 is 14.5840, and the maximum one-year fatigue damage for the case of joint PDF 2 is 2.7411. The calculated maximum one-year fatigue damage using joint PDF 1 is 5.32 times larger than that using joint PDF 2. This finding confirms that the wind load variation plays a critical role in

blade fatigue analysis. It also attests that, due to the variable wind load in the large spatiotemporal range, varied wind load distributions corresponding to the realistic measured wind data must be considered in the reliability analysis of wind turbines.

The developed wind load uncertainty model will be used to create a mean wind load for deterministic design optimization (DDO) in Chapter 4 and provide uncertain wind load for reliability analysis and reliability-based design optimization (RBDO) in Chapter 5 and Chapter 6, respectively.

CHAPTER 4
DETERMINISTIC DESIGN OPTIMIZATION OF COMPOSITE WIND TURBINE BLADES UNDER MEAN WIND LOAD

In this chapter, a deterministic design optimization (DDO) procedure for composite wind turbine blades is explained. The purpose of DDO is to obtain a DDO optimum design, which usually provides a good initial design to reliability-based design optimization (RBDO), so that less computational effort will be required in the following RBDO procedure. Because DDO does not involve wind load uncertainty, one representative wind load is considered in DDO. The mean wind load of the wind load uncertainty model is first obtained as the representative wind load in Section 4.1. The DDO of the composite wind turbine blade under the mean wind load is presented in Section 4.2. The DDO results and discussion are given in Section 4.3.

4.1 Mean Wind Load Generation

4.1.1 Wind Load Probability Table

As explained in Chapter 3, the one-year fatigue damage is determined by the design vector **d** and random parameters C, k, a, b, and τ. However, the theoretical equation to calculate the one-year fatigue damage, as shown in Eq. (3.23), cannot be explicitly expressed as a function of **d**, C, k, a, b, and τ, due to the complexity of the joint PDF and 10-minute fatigue damage calculation. Thus, in real damage calculation, the double integration in Eq. (3.23) is numerically calculated using the Riemann integral as

$$D_{1year}\left(\mathbf{d},C,k,a,b,\tau\right)\approx 52560\sum_{i=1}^{m}\sum_{j=1}^{n}P_{VI}^{i,j}\left(v_{10}^{i},i_{10}^{j};C,k,a,b,\tau\right)D_{10}^{i,j}\left(\mathbf{d},v_{10}^{i},i_{10}^{j}\right) \qquad (4.1)$$

where the probability of V_{10} and I_{10} being in a small cell can be calculated as

$$P_{VI}^{i,j}\left(v_{10}^{i},i_{10}^{j};C,k,a,b,\tau\right)=f_{VI}\left(v_{10}^{i},i_{10}^{j};C,k,a,b,\tau\right)\Delta v_{10}\Delta i_{10} \qquad (4.2)$$

Here, Δv_{10} and Δi_{10} are the intervals discretizing ranges of V_{10} and I_{10}, respectively. In this study, the ranges of V_{10} and I_{10} are evenly discretized. The numbers of selected V_{10} and I_{10} are m and n, respectively. v_{10}^{i} is the value of V_{10} at the center of ith interval in the V_{10} direction. Therefore, $v_{10}^{i}=v_{10}^{1}+(i\text{-}1)\Delta v_{10}$. Similarly, i_{10}^{j} is the value of I_{10} at the center of the jth interval in the I_{10} direction. Hence, $i_{10}^{j}=i_{10}^{1}+(j\text{-}1)\Delta i_{10}$. f_{VI} is the joint probability density function (PDF) of V_{10} and I_{10}.

In this study, a large range of V_{10} and I_{10} has been considered to examine the fatigue damage considering all probable wind conditions. Moriarty *et al.* applied the cut-in wind speed and the cut-out wind speed as the lower bound and upper bound respectively, of 10-minute segments in one-year fatigue simulation, and the calculated fatigue load cycles agreed well with those obtained by a long-term extrapolation method in their work (Moriarty *et al.*, 2004). The turbines were assumed to operate 100% of the time between cut-in and cut-out wind speed with 100% availability (Moriarty *et al.*, 2004). Even though the unsteadiness when wind speed is larger than cut-out wind speed can cause large fluctuating loads, the probability of occurrence of such extreme wind conditions is very small, which makes little fatigue contribution in long term. The damage due to extreme wind condition may be better addressed by wind turbine extreme analysis, which is beyond the scope of this study. In this study, the lower bound and upper bound of V_{10} are set to be the cut-in wind speed of 3 m/s and cut-out wind speed of 25 m/s, respectively (Jonkman *et al.*, 2009b). The lower bound and upper bound of I_{10} are set to be 0.02 and 1, respectively. The 10-minute fatigue analyses are run over the range of V_{10} between 3 m/s and 25 m/s in 2 m/s increments, and the range of I_{10} between 0.02 and 1 in 0.02 increments. Therefore, the number of V_{10} and I_{10} are 12 and 50, respectively (i.e., m = 12 and n = 50 in Eq. (4.1)). There are 600 different wind conditions in total. All the wind conditions are listed in Table 4.1.

Table 4.1 Selected 600 Wind Conditions

I_{10} / V_{10} (m/s)	0.02	0.04	0.06	0.08	….	0.94	0.96	0.98	1
3	3,0.02	3,0.04	3,0.06	3,0.08	….	3,0.94	3,0.96	3,0.98	3,1
5	5,0.02	5,0.04	5,0.06	5,0.08	….	5,0.94	5,0.96	5,0.98	5,1
7	7,0.02	7,0.04	7,0.06	7,0.08	….	7,0.94	7,0.96	7,0.98	7,1
9	9,0.02	9,0.04	9,0.06	9,0.08	….	9,0.94	9,0.96	9,0.98	9,1
11	11,0.02	11,0.04	11,0.06	11,0.08	….	11,0.94	11,0.96	11,0.98	11,1
13	13,0.02	13,0.04	13,0.06	13,0.08	….	13,0.94	13,0.96	13,0.98	13,1
15	15,0.02	15,0.04	15,0.06	15,0.08	….	15,0.94	15,0.96	15,0.98	15,1
17	17,0.02	17,0.04	17,0.06	17,0.08	….	17,0.94	17,0.96	17,0.98	17,1
19	19,0.02	19,0.04	19,0.06	19,0.08	….	19,0.94	19,0.96	19,0.98	19,1
21	21,0.02	21,0.04	21,0.06	21,0.08	….	21,0.94	21,0.96	21,0.98	21,1
23	23,0.02	23,0.04	23,0.06	23,0.08	….	23,0.94	23,0.96	23,0.98	23,1
25	25,0.02	25,0.04	25,0.06	25,0.08	….	25,0.94	25,0.96	25,0.98	25,1

At each wind condition, a wind load probability $P_{VI}^{i,j}$ is calculated using Eq. (4.2), and a 10-minute fatigue damage $D_{10}^{i,j}$ is calculated using the developed fatigue analysis procedure in Chapter 2. In this way, a 12-by-50 wind load probability table and a 12-by-50 10-minute fatigue damage table can be constructed. For brevity, the wind load probability table and the 10-minute fatigue damage table are symbolically shown in Table 4.2 and Table 4.3, respectively.

Table 4.2 Wind Load Probability Table

I_{10} / V_{10}	i_{10}^{1}	i_{10}^{2}	⋯	i_{10}^{50}
v_{10}^{1}	$P_{VI}^{1,1}$	$P_{VI}^{1,2}$	⋯	$P_{VI}^{1,50}$
v_{10}^{2}	$P_{VI}^{2,1}$	$P_{VI}^{2,2}$	⋯	$P_{VI}^{2,50}$
⋮	⋮	⋮	⋱	⋮
v_{10}^{12}	$P_{VI}^{12,1}$	$P_{VI}^{12,2}$	⋯	$P_{VI}^{12,50}$

Table 4.3 Ten-minute Fatigue Damage Table

I_{10} / V_{10}	i_{10}^{1}	i_{10}^{2}	⋯	i_{10}^{50}
v_{10}^{1}	$D_{VI}^{1,1}$	$D_{VI}^{1,2}$	⋯	$D_{VI}^{1,50}$
v_{10}^{2}	$D_{VI}^{2,1}$	$D_{VI}^{2,2}$	⋯	$D_{VI}^{2,50}$
⋮	⋮	⋮	⋱	⋮
v_{10}^{12}	$D_{VI}^{12,1}$	$D_{VI}^{12,2}$	⋯	$D_{VI}^{12,50}$

To facilitate understanding the two types of tables, a typical wind load probability table and a typical 10-minute fatigue damage table are illustrated by 3-D bar charts in Figure 4.1 and Figure 4.2, respectively. In Figure 4.1, the C, k, a, b, τ used to generate the illustrated wind load probability table are C = 6.5856, k = 2.5178, a =3.1570, b = 0.4123, τ = 0.6826. Figure 4.2 uses 10-minute fatigue damages calculated at a node-section point randomly selected from the blade model developed in Chapter 2. As shown in Figure 4.1, the large probabilities are concentrated at mild wind conditions, e.g., V_{10} < 11 m/s, I_{10} < 0.3. For extreme wind conditions, the probabilities are much smaller than those corresponding to mild wind load conditions. The reason these extreme wind conditions are also considered is that the 10-minute fatigue damages under extreme wind conditions are often much larger than those under mild wind conditions. As shown in Figure 4.2, the 10-minute fatigue damage increases exponentially as V_{10} and I_{10} increase. Hence, it is necessary to include all the wind conditions when calculating the one-year fatigue damage. A 3-D bar chart of the multiplication of the wind load probability table (Figure 4.1) and the 10-minute fatigue damage table (Figure 4.2) is shown in Figure 4.3. As shown in Figure 4.3, in this case the distribution of the multiplication is more close to that of the wind load probability table. The large multiplication values are clustered at the mild wind conditions. The reason is that the magnitude of probability at the extreme wind conditions is much smaller than that at the mild wind conditions. For example, P_{VI} =0.0453 when V_{10} = 7 m/s, I_{10} = 0.22, while P_{VI} =2.27E−36 when V_{10} = 17 m/s, I_{10} = 1 in Figure 4.1. Even though the D_{10} is relatively large at the extreme wind conditions, the multiplication of the probability and the D_{10} is smaller at the extreme wind conditions than that at the mild wind conditions in this case.

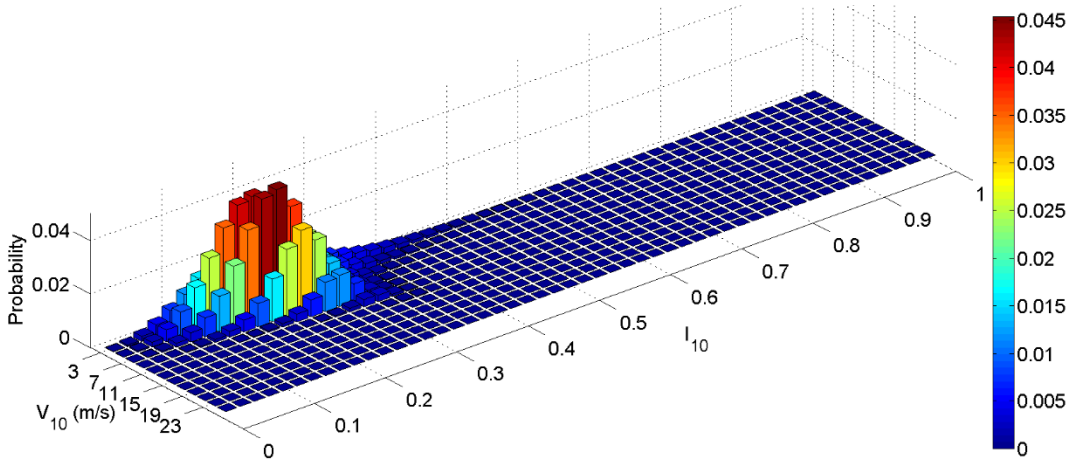

Figure 4.1 A 3-D Bar Chart of a Wind Load Probability Table

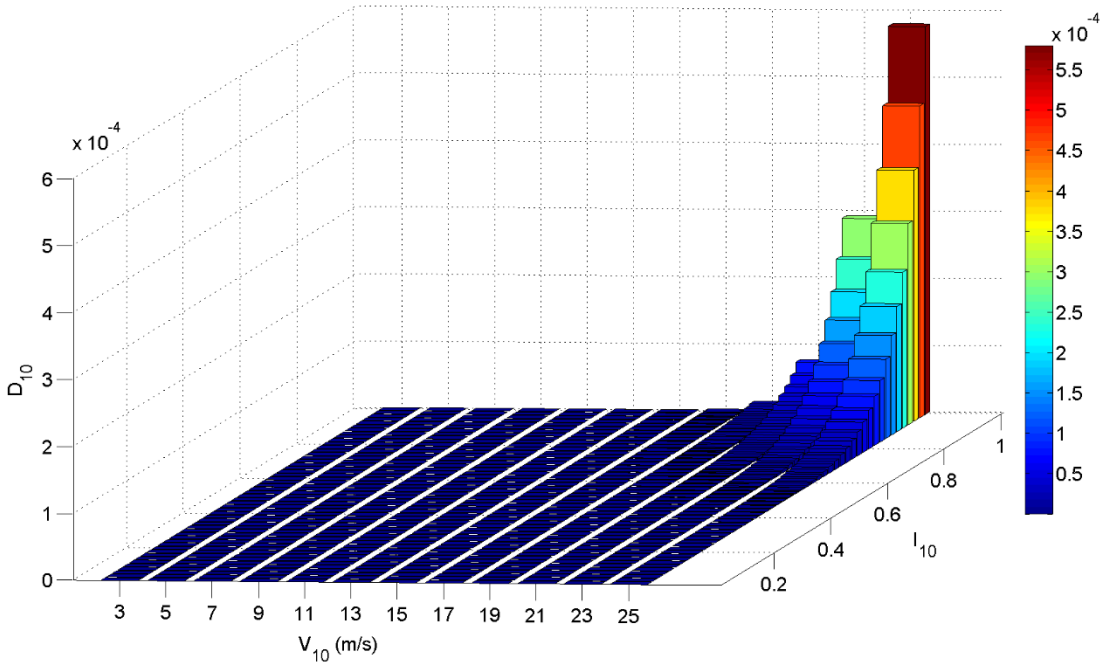

Figure 4.2 A 3-D Bar Chart of a 10-minute Fatigue Damage Table

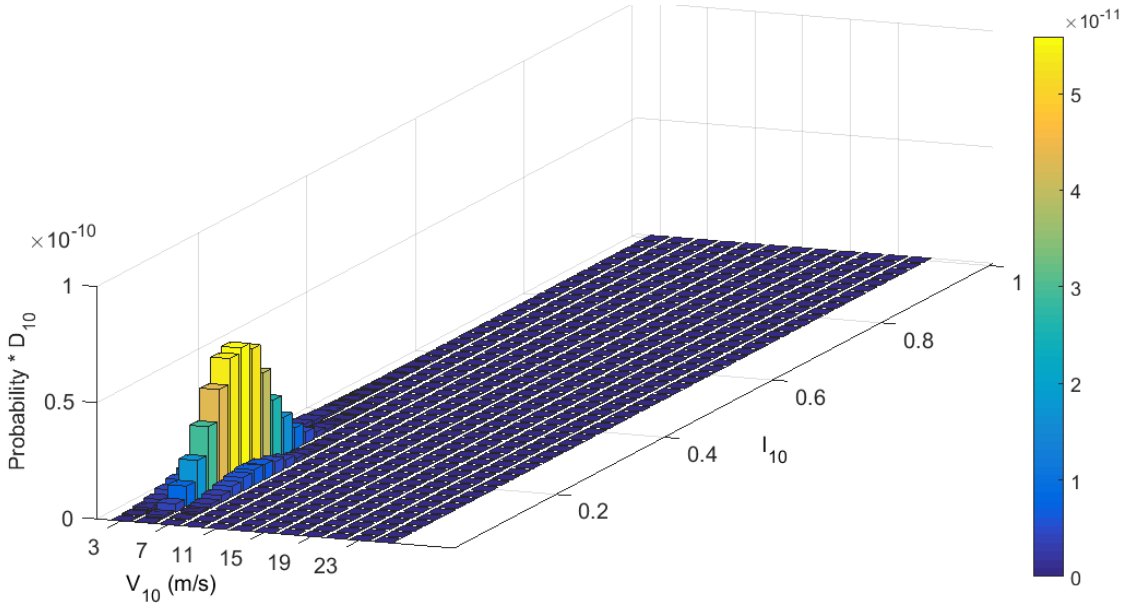

Figure 4.3 A 3-D Bar Chart of the Multiplication of a Wind Load Probability Table and a 10-minute Fatigue Damage Table

4.1.2 Mean Wind Load Probability Table

In order to provide a mean wind load for DDO, a mean wind load probability table is generated using the Monte Carlo simulation (MCS) method. The main procedure to calculate the mean wind load probability table is listed below.

(1) Generate one million MCS sample sets of (C, k, a, b, τ) based on the identified distributions in Table 3.4. Assume C, k, a, b, and τ are independent.

(2) Create one million joint PDFs of V_{10} and I_{10} based on the MCS samples of (C, k, a, b, τ). The joint PDF of V_{10} and I_{10} is shown in Eq. (3.22).

(3) Create a wind load probability table based on each joint PDF of V_{10} and I_{10}. The probability value $P_{VI}^{i,j}$ in each cell (corresponding to each combination of v_{10}^{i} and i_{10}^{j}) in the probability table is calculated using Eq. (4.2). Thus, one million wind load probability tables can be created using one million joint PDFs of V_{10} and I_{10}.

(4) Calculate an average value $\bar{P}_{VI}^{i,j}$ of one million probability values corresponding to the same wind condition v_{10}^{i} and i_{10}^{j}. Then use the average value as the probability value in the cell of the mean wind load probability table. Similarly, the mean probability values corresponding to other wind conditions can be obtained. Finally, the mean wind load probability table using one million MCS samples of (C, k, a, b, τ) is obtained.

The generated mean wind load probability table is schematically shown in Figure 4.4. As shown in Figure 4.4, the largest probability value 0.0218 corresponds to V_{10} = 7 m/s and I_{10} = 0.1. Each cell in the mean wind load probability table contains an averaged probability of one wind load considering the wind load variation in a large spatiotemporal range.

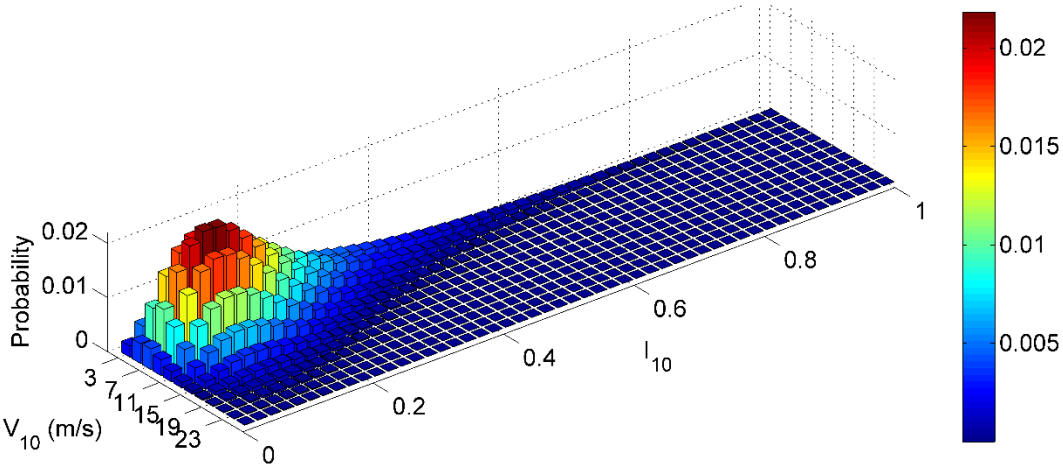

Figure 4.4 3-D Bar Chart of the Mean Wind Load Probability Table

4.2 Deterministic Design Optimization under Mean Wind Load

Using the mean wind load probability table generated in Section 4.1, the composite wind turbine blade developed in Section 2.3.1 has been utilized as an initial design for the DDO procedure. The objective function is the total cost of composite materials used in the blade. Design variables are laminate thicknesses of the blade, and there are 12 design variables. Twenty-year fatigue damages, under the assumption that the mean wind load in Section 4.1 will continue for 20 years, of selected hotspots are used for the optimization constraints. The DDO procedure tailors laminate thickness design variables to minimize the cost while satisfying a 20-year fatigue lifespan under a mean wind load condition.

4.2.1 Design Variables

As shown in Figure 4.5, the blade is composed of seven parts: the root, forward shear web, aft shear web, leading edge, spar cap, trailing edge, and tip. In the developed parametric blade model, each part consists of one/multiple panel(s). For example, the root has only one panel while the forward shear web has 13 panels. The blade is made of 71 panels in total. Each panel is composed of composite laminates, e.g., QQ1 and P2B. There is a foam core layer in the middle of the panels of the forward shear web, aft shear web, leading edge, and trailing edge. The numbers of layers in the outer shell of the blade, i.e., root, leading edge, trailing edge, spar cap and tip, have referred to the laminate schedule of the Sandia's l00-m blade model (Griffith and Ashwill, 2011). The detail laminate schedule of the blade is given in Table 2.4. The number of laminate layers in each panel is summarized in Table 4.4. The hierarchical relationship for the blade, parts, panels, and laminates is shown in Figure 4.6.

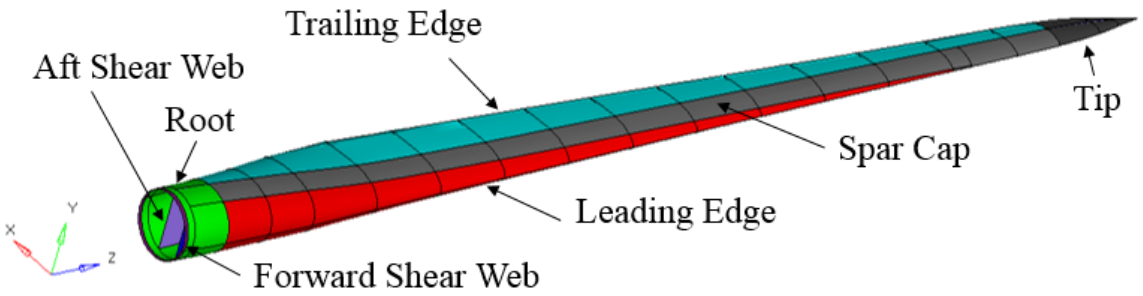

Figure 4.5 Seven Parts of the Composite Wind Turbine Blade

Table 4.4 Composite Material Type Used in Each Part and Number of Laminate Layers in Each Panel at the Initial Design

Part Name	Composite Materials	Number of Laminate Layers															
Root	QQ1	7															
Forward Shear Web	QQ1	4	4	4	4	4	4	4	4	4	4	4	4	4			
Aft Shear Web	QQ1	4	4	4	4	4	4	4	4	4	4	4	4	4	4	4	4
Tip	QQ1	2															
Leading Edge	QQ1	4	4	6	4	2	2	2	2	2	2	2	2				
Trailing Edge	QQ1	4	4	4	4	2	2	2	2	2	2	2	2	2	2		
Spar Cap	P2B	6	6	10	10	10	10	10	10	8	6	4	4	4	4		
Panel Number		1	2	3	4	5	6	7	8	9	10	11	12	13	14	15	16

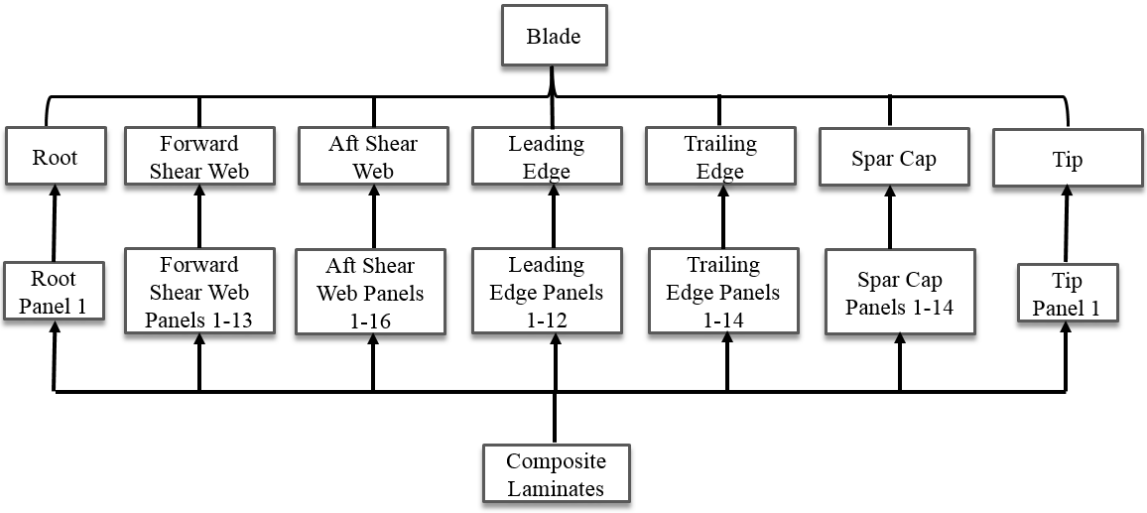

Figure 4.6 Hierarchical Relationship in the Parametric Composite Blade Model

The design variables control the thicknesses of the composite laminates. The thicknesses of laminates in the same panel are assumed to be identical. In order to reduce the number of design variables, one design variable is linked to one or multiple panels. For example, design variable 1 is linked to the root panel; design variable 2 is linked to the panels 1 to 5 in the forward shear web. The detailed linkage between design variables and linked panels is shown in Table 4.5. The initial value, lower and upper bounds of design variables, and corresponding composite materials are also listed in Table 4.5. It is noted that a design variable is not the total thickness of corresponding panels. It is the thickness of one composite laminate. For example, when design variable d_1 is 4 mm, the thickness of root panel 1 is 28 mm because there are seven laminate layers, as shown in Table 4.4.

Table 4.5 Initial Value, Lower and Upper Bounds of Design Variables, Linked Panels, and Composite Materials

Design Variables	Initial Value (mm)	Lower Bound (mm)	Upper Bound (mm)	Linked Panel	Composite Material
d_1	4	2	8	Root Panel 1	QQ1
d_2	4	2	16	Forward Shear Panels 1-5	QQ1
d_3	4	2	16	Forward Shear Panels 6-9	QQ1
d_4	4	2	16	Forward Shear Panels 10-13	QQ1
d_5	4	2	16	Aft Shear Web Panels 1-4	QQ1
d_6	4	2	16	Aft Shear Web Panels 5-8	QQ1
d_7	4	2	16	Aft Shear Web Panels 9-12	QQ1
d_8	4	2	16	Aft Shear Web Panels 13-16	QQ1
d_9	4	2	8	Tip Panel 1	QQ1
d_{10}	4	2	8	Leading Edge Panels 1-12	QQ1
d_{11}	4	2	8	Trailing Edge Panels 1-14	QQ1
d_{12}	2.5	1.5	4.5	Spar Cap Panels 1-14	P2B

4.2.2 Objective Function

The objective function in DDO is the total cost of the composite materials used in the blade model. As the thickness of the laminate changes, the mass of composite materials changes proportionally. Consequently, the cost is a function of laminate thickness, i.e., design variables. According to TPI Composites (2003), the material cost of QQ1, which belongs to E-glass composite material, is $4.18/kg. The material cost of P2B, which is carbon/E-glass hybrid-fiber-reinforced composite material, is taken to be $11.70/kg.

If the initial mass of panel(s) linked to the *i*th design variable is m_i^0 (unit: ton) and the initial design is d_i^0 (unit: mm), then the mass of panel(s) at a new design d_i can be calculated as

$$m_i = m_i^0 \frac{d_i}{d_i^0} \tag{4.3}$$

where i = 1, 2, …, 12. Assuming the material cost is proportional to the mass, the cost (unit: dollar) of composite materials used in the blade can be calculated as

$$Material\ Cost = 4.18 \times 1000 \times \sum_{i}^{11} m_i^0 \frac{d_i}{d_i^0} + 11.70 \times 1000 \times m_{12}^0 \frac{d_{12}}{d_{12}^0} \tag{4.4}$$

In this study, Matlab's Sequential Quadratic Programming (SQP) algorithm (Matlab, 2012) is used for DDO. The magnitude of composite material cost is at a level of 10,000, while the constraints are normalized at a level of 1. In the nonlinear constrained optimization process, the level difference between the objective function and the constraints might cause the problem that the optimization process is dominated by the objective function, such that the optimization process mainly considers the objective function while ignoring the constraints. Thus, the optimization iteration may not converge well. In order to avoid this problem, the composite material cost in Eq. (4.4) is normalized by its initial value. The final objective function for DDO becomes

$$C(\mathbf{d}) = \left(4.18 \times 1000 \times \sum_{i}^{11} m_i^0 \frac{d_i}{d_i^0} + 11.70 \times 1000 \times m_{12}^0 \frac{d_{12}}{d_{12}^0} \right) \Big/ Cost^0 \tag{4.5}$$

where the design vector $\mathbf{d} = [d_1, d_2, \ldots, d_{12}]$; m_i^0 is the initial mass of panel(s) linked to the ith design variable; d_i^0 is the initial ith design variable; and $Cost^0$ is the initial composite material cost, which is \$95,494 in this study.

4.2.3 Fatigue Constraints

The constraints for DDO are to satisfy the 20-year fatigue lifespan. In other words, the 20-year fatigue damages for all node-section points in the blade model should be smaller than 1. A demonstration of node-section points is shown in Figure 2.5 in Section 2.3.2. Under the assumption that the mean wind load condition continues for 20 years, the 20-year fatigue damage is calculated as

$$D_{20\,year}(\mathbf{d}) = 52560 \times 20 \times \sum_{i}^{12} \sum_{j}^{50} \bar{P}_{VI}^{i,j}\left(v_{10}^i, i_{10}^j\right) D_{10}^{i,j}\left(\mathbf{d}, v_{10}^i, i_{10}^j\right) \tag{4.6}$$

where 52560 indicates the number of 10-minute periods in one year; 20 indicates that the designed lifespan is 20 years, and $\bar{P}_{VI}^{i,j}(v_{10}^i, i_{10}^j)$ is the mean probability value corresponding to the wind condition $V_{10} = v_{10}^i$ and $I_{10} = i_{10}^j$. The mean probability value is obtained from the mean wind load probability table (Figure 4.4) in Section 4.1.

The fatigue hotspots are the node-section points where fatigue is considered as the DDO constraints. A node-section point, which combines nodal ID and section point ID, identifies the specific location at the blade FE model. The selection of fatigue hotspots is a challenging issue due to the complexity of the blade model. The blade FE model consists of 3,422 nodes, and each node corresponds to multiple section points through laminate thickness. The number of section points corresponding to each FE node depends on the number of laminate layers in a panel. In total, there are 60,954 node-section points in the blade FE model. It is quite demanding computationally to check the fatigue damages of all the node-section points during the DDO procedure due to the

computational burden. In addition, the fatigue-critical node-section points may vary in each DDO iteration due to design change. For example, new fatigue-critical node-section points may come out because the associated laminate thickness becomes small in a design iteration. Thus, the fatigue hotspots need to be wisely selected in order to save computational time and to make sure that all node-section points satisfy the 20-year fatigue life constraints at the DDO optimum design.

The main steps for selecting hotspots in DDO are listed below.

(1) Calculate 20-year fatigue damages of all node-section points of the blade at the initial design.

(2) For each panel, find the node-section point that has the largest fatigue damage in the panel. These node-section points with largest fatigue damages are the initial hotspots in DDO.

(3) Include the 20-year fatigue damages of the initial hotspots into DDO constraints.

(4) Launch the DDO procedure.

(5) After five iterations, stop the DDO procedure. Check all the node-section points at the latest design. If there are new hotspots, add their fatigue damages to the constraint and go to step 4. If the DDO procedure converges under five iterations, go to step 6.

(6) Check the 20-year fatigue damages of all the node-section points. If there is no new hotspot, DDO is converged. If there are new hotspots, add their fatigue damages to the constraints and go to step 4.

In conclusion, the DDO of the blade for fatigue under the mean wind load can be formulated as

$$\text{minimize } C(\mathbf{d}) = \left(4.18\times 1000\times \sum_{i}^{11} m_i^0 \frac{d_i}{d_i^0} + 11.70\times 1000\times m_{12}^0 \frac{d_{12}}{d_{12}^0} \right) \Big/ Cost^0$$

$$\text{subject to } G_k(\mathbf{d}) = 52560\times 20\times \sum_{i}^{12}\sum_{j}^{50} \bar{P}_{VI}^{i,j}\left(v_{10}^i, i_{10}^j\right) D_{10}^{i,j}\left(\mathbf{d}, v_{10}^i, i_{10}^j\right) - 1 < 0,\ k = 1, 2, ..., NC$$

$$\mathbf{d}^L \le \mathbf{d} \le \mathbf{d}^U, \quad \mathbf{d} \in \mathbb{R}^{NDV} \tag{4.7}$$

where $\mathbf{d}$ is the 12-dimensional design variable vector for laminate thicknesses; $\mathbf{d}^L$ and $\mathbf{d}^U$ are the lower bound and upper bound for the design variable vector, respectively; G_k is the k-th constraint function; and NC is the number of constraints.

4.3 DDO Results and Discussion

The whole DDO procedure consists of seven sets of the five iterations, which is called the "intermediate process" hereafter. In the beginning of DDO, 69 node-section points are selected as hotspots at the initial design. Because some selected node-section points are shared by adjacent panels, the number of hotspots at the initial design is smaller than the total number of panels, i.e., 71. As the DDO procedure goes on, the number of hotspots increases as new hotspots are added in each intermediate process. Finally, 120 node-section points are selected as hotspots for DDO constraints. The DDO procedure is converged at the first iteration of the eighth intermediate process, because the design change is less than the tolerance 1E−3 and the relative maximum constraint violation is also less than the tolerance 1E−3. Table 4.6 compares the design variables, objective function, and fatigue life of the blade at the initial design and the DDO optimum design. The histories of the cost function and fatigue life are plotted in Figure 4.7. Here, the fatigue life (unit: year) of the blade is calculated as

$$\text{Fatigue Life} = \frac{20}{D_{20\,year}^{\max}} \tag{4.8}$$

where $D_{20year}^{\max}$ is the maximum 20-year fatigue damage among all node-section points in the blade model.

As shown in Table 4.6, the fatigue life of the initial design is only 0.0004 year, which obviously does not satisfy the target fatigue lifespan of 20 years. After the DDO procedure, the cost is increased by 31.53% and the fatigue life of the blade model is significantly increased to satisfy the 20-year fatigue lifespan. That is, the fatigue life of the DDO optimum design is about 49,999 times longer than that of the initial design.

Table 4.6 Design Variables, Cost, and Fatigue Life at Initial Design and at DDO Optimum Design

	Initial Design	DDO Optimum Design
d_1 (mm)	4	3.99
d_2 (mm)	4	3.50
d_3 (mm)	4	4.45
d_4 (mm)	4	**6.51**
d_5 (mm)	4	2.00
d_6 (mm)	4	2.00
d_7 (mm)	4	**7.06**
d_8 (mm)	4	4.40
d_9 (mm)	4	2.00
d_{10} (mm)	4	4.73
d_{11} (mm)	4	5.31
d_{12} (mm)	2.5	3.85
Cost	1	1.3153
Fatigue Life (year)	0.0004	19.9995

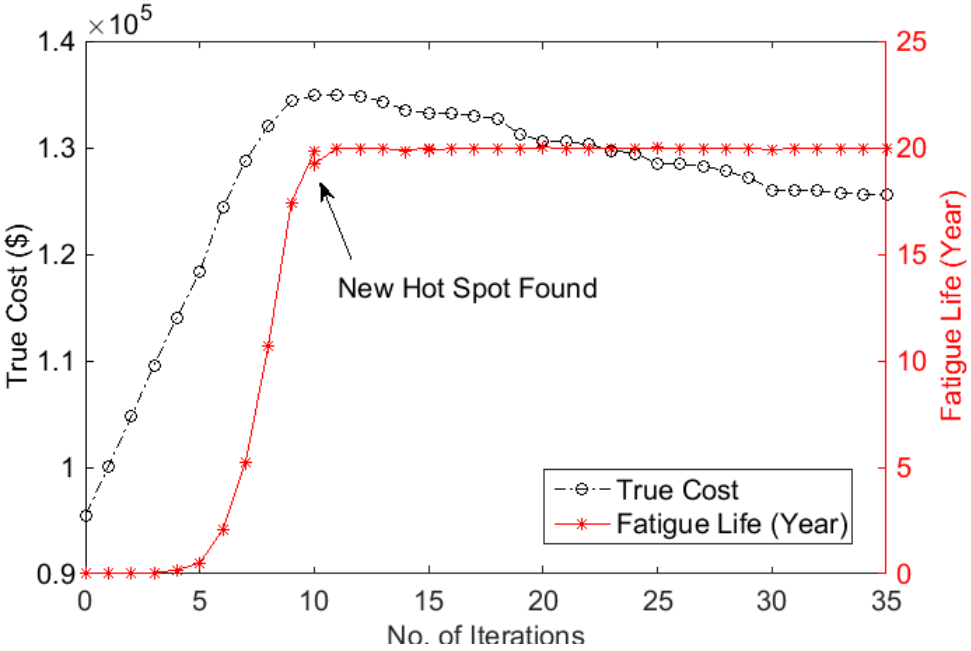

Figure 4.7 Histories of Cost and Fatigue Life in DDO

As shown in Figure 4.7, there is a drop at the 10th iteration in the fatigue life history. The drop occurred because new fatigue hotspots were identified after 10 iterations. Among the new hotspots, one hotspot has significantly large fatigue damage compared to the others. After incorporating this new hotspot, the fatigue life was reduced while the cost remained the same. After 35 iterations, the DDO procedure was converged and no violated hotspots were found. The number of active or violated constraints are reduced from fifteen at the initial design to six at the DDO optimum design. Figure 4.8 shows the nodal location of hotspots corresponding to active or violated constraints at the initial design and the DDO optimum design. It is shown that the hotspots are moved from rear part at the initial design to the root at the DDO optimum design because many more materials are applied at the rear part of the DDO optimum design. For example, as shown in Table 4.6, the rear part of the forward shear web controlled by design variable d_4 and

the rear part of the aft shear web controlled by design variable d_7 are increased by 62.8% and 76.5%, respectively, which significantly increases the fatigue strength in the rear part of the blade. The six hotspots at the DDO optimum design will be used for constraints in RBDO in Chapter 6.

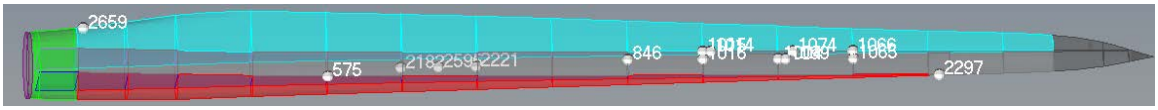

(a) At the initial design

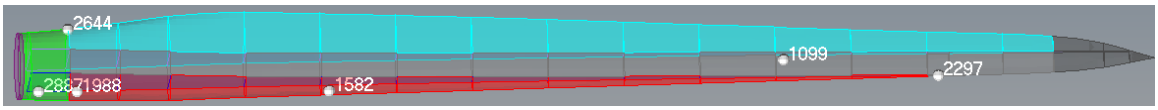

(b) At the DDO optimum design

Figure 4.8 Nodal Location of Hotspots Corresponding to Active/Violated Constraints at the Initial Design and the DDO Optimum Design

Table 4.6 shows that the design variables d_4 and d_7 have relatively large values at the DDO optimum design. In order to generate a reasonable thickness of composite laminates for manufacturing purposes, the number of laminate layers in the panels corresponding to d_4 and d_7 has been adjusted so that the thicknesses of these two design variables at the DDO optimum design are reduced. The total thickness of each panel has remained the same after increasing the number of laminate layers. In addition, the 20-year fatigue damages of all node-section points of the adjusted blade model has been checked again. No violated node-section point has been found in the adjusted blade model. In fact, for the hotspots corresponding to active constraints at the DDO optimum

design, the adjusted blade model produces the same fatigue damage as the original model because d_4 and d_7 correspond to uniaxial laminate layers. Thus, the fatigue life of the adjusted model is the same as the original model at the DDO optimum design. The final adjusted model at the DDO optimum design and number of laminate layers are shown in Table 4.7 and Table 4.8, respectively.

Table 4.7 Design Variables, Cost, and Fatigue Life of the Adjusted Model at DDO Optimum Design

d_1 (mm)	3.99
d_2 (mm)	3.50
d_3 (mm)	4.45
d_4 (mm)	**4.34**
d_5 (mm)	2.00
d_6 (mm)	2.00
d_7 (mm)	**3.53**
d_8 (mm)	4.40
d_9 (mm)	2.00
d_{10} (mm)	4.73
d_{11} (mm)	5.31
d_{12} (mm)	3.85
Cost	1.3153
Fatigue Life (year)	19.9995

Table 4.8 Number of Laminate Layers of the Adjusted Model at DDO Optimum Design

Part Name	Number of Laminate Layers in Each Panel															
Root	7															
Forward Shear Web	4	4	4	4	4	4	4	4	4	**6**	**6**	**6**	**6**			
Aft Shear Web	4	4	4	4	4	4	4	4	**8**	**8**	**8**	**8**	4	4	4	4
Tip	2															
Leading Edge	4	4	6	4	2	2	2	2	2	2	2	2				
Trailing Edge	4	4	4	4	2	2	2	2	2	2	2	2	2	2		
Spar Cap	6	6	10	10	10	10	10	10	8	6	4	4	4	4		
Panel Number	1	2	3	4	5	6	7	8	9	10	11	12	13	14	15	16

CHAPTER 5

RELIABILITY ANALYSIS OF COMPOSITE WIND TURBINE BLADES UNDER WIND LOAD UNCERTAINTY

This chapter describes the reliability analysis method for composite wind turbine blades under wind load uncertainty. In Section 5.1, the Monte Carlo simulation (MCS) method to simulate uncertain wind load using the developed dynamic wind load uncertainty model is explained. The reliability analysis method using MCS can estimate the probability that a wind turbine could survive 20 years of target lifespan. The reliability analyses at the initial design and the deterministic optimal design have been carried out in Section 5.2. Results and discussion are provided in Section 5.3. The overall procedure to carry out reliability analysis for a given design under wind load uncertainty is shown in Figure 5.1.

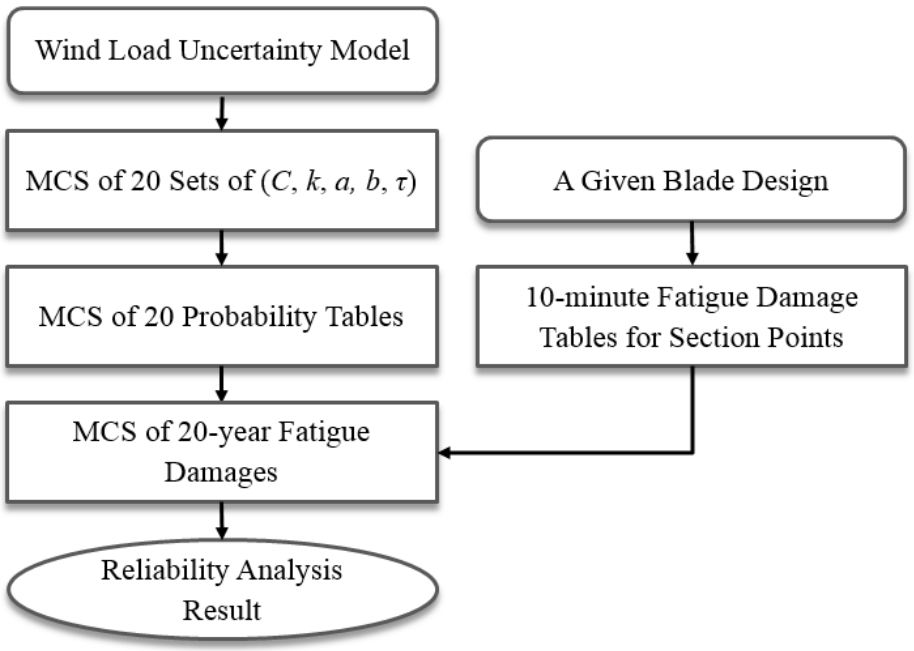

Figure 5.1 Flowchart of Reliability Analysis of Wind Turbine Blade at a Design under Wind Load Uncertainty

5.1 Reliability Analysis Using Monte Carlo Simulation

As given in Eq. (4.1), the one-year fatigue damage is calculated using Riemann integration as

$$D_{1year}\left(\mathbf{d},C,k,a,b,\tau\right)\approx 52560\sum_{i=1}^{12}\sum_{j=1}^{50}P_{VI}^{i,j}\left(v_{10}^{i},i_{10}^{j};C,k,a,b,\tau\right)D_{10}^{i,j}\left(\mathbf{d},v_{10}^{i},i_{10}^{j}\right) \tag{5.1}$$

where $P_{VI}^{i,j}$ and $D_{VI}^{i,j}$ are the probability and the 10-minute fatigue damage, respectively, corresponding to a wind condition (v_{10}^{i}, i_{10}^{j}). The $P_{VI}^{i,j}$, $D_{VI}^{i,j}$, and corresponding wind condition are obtained from a wind load probability table, a 10-minute fatigue damage table, and a wind condition table, respectively. The details of constructing the three tables are given in Section 4.1.

In this study, the wind load condition table includes 600 wind load conditions and does not change, as shown in Table 4.1. Thus, the one-year fatigue damage calculation depends only on the wind load probability table and the 10-minute fatigue damage table. Furthermore, the wind load probability table is determined by (C, k, a, b, τ), and the 10-minute fatigue damage table is determined only by design **d**. Therefore, for a given design **d**, the one-year fatigue damage is a function of (C, k, a, b, τ) only. Finally, considering the wind load variation in a 20-year range, 20-year fatigue damage at a given design **d** can be calculated as

$$\begin{aligned} D_{20\,year}\left(\mathbf{d};\mathbf{C},\mathbf{k},\mathbf{a},\mathbf{b},\boldsymbol{\tau}\right) &= \sum_{t=1}^{20}D_{1year}^{t}\left(\mathbf{d},C^{t},k^{t},a^{t},b^{t},\tau^{t}\right) \\ &= 52560\sum_{t=1}^{20}\sum_{i=1}^{12}\sum_{j=1}^{50}P_{VI}^{i,j}\left(v_{10}^{i},i_{10}^{j};C^{t},k^{t},a^{t},b^{t},\tau^{t}\right)D_{10}^{i,j}\left(\mathbf{d},v_{10}^{i},i_{10}^{j}\right) \end{aligned} \tag{5.2}$$

where random vectors **C**, **k**, **a**, **b**, and **τ** contain 20 sets of (C, k, a, b, τ) as $\mathbf{C} = [C^{1}, C^{2},\ldots, C^{20}]$, $\mathbf{k} = [k^{1}, k^{2},\ldots, k^{20}]$, $\mathbf{a} = [a^{1}, a^{2},\ldots, a^{20}]$, $\mathbf{b} = [b^{1}, b^{2},\ldots, b^{20}]$, and $\boldsymbol{\tau} = [\tau^{1}, \tau^{2},\ldots, \tau^{20}]$. Hence, there are 100 random parameters in Eq. (5.2). In this study, the random vectors are assumed to be independent. The 20 random parameters in one random vector are also

assumed to be independent, which means last year's wind load is independent from this year's.

In Eq. (5.2), the 20-year fatigue damage D_{20year} is also random because the random vectors **C**, **k**, **a**, **b**, and **τ** are random. Consequently, a fatigue failure ($D_{20year} > 1$) in 20 years can be measured with its probability. The probability of fatigue failure cannot be calculated using a sensitivity-based reliability method such as the first-order reliability method (FORM) or the second-order reliability method (SORM) because the sensitivity (gradient) of D_{20year} is not available due to its implicit feature. In this study, the probability of fatigue failure is calculated using a sampling-based reliability method that uses MCS. Using Eq. (5.2) and MCS, the probability of fatigue failure is calculated as

$$\begin{aligned} P\left(\text{Fatigue Life } < \text{ 20 years}\right) &= P\left(D_{20\,year}\left(\mathbf{d};\mathbf{X}\right) > 1\right) \\ &= \int_{D_{20\,year}(\mathbf{d},\mathbf{X})>1} f_{\mathbf{X}}\left(\mathbf{x}\right) d\mathbf{x} \\ &= \int_{\mathbb{R}^N} I_{\Omega_F}\left(\mathbf{x}\right) f_{\mathbf{X}}\left(\mathbf{x}\right) d\mathbf{x} \\ &\cong \frac{1}{NMCS} \sum_{i=1}^{NMCS} I_{\Omega_F}\left[\mathbf{x}^{(i)}\right] \end{aligned} \tag{5.3}$$

where $\mathbf{X} = [\mathbf{C}, \mathbf{k}, \mathbf{a}, \mathbf{b}, \boldsymbol{\tau}]$, and $\mathbf{x}^{(i)}$ is the ith realization of **X**. It is worth noting that the realization $\mathbf{x}^{(i)}$ is randomly generated based on the PDFs of (C, k, a, b, τ) in Table 3.4. Each realization includes 20 sets of (C, k, a, b, τ). *NMCS* is the number of realizations for MCS. Ω_F is the failure domain such that $D_{20year}(\mathbf{d}; \mathbf{X}) > 1$, and $I_{\Omega_F}(\cdot)$ is an indicator function defined as

$$I_{\Omega_F}\left(\mathbf{x}\right) = \begin{cases} 1, & \text{for } \mathbf{x} \in \Omega_F \\ 0, & \text{otherwise} \end{cases}. \tag{5.4}$$

Though the reliability analysis calculation is straightforward, there are two points that need to be noted. One is that the uncertainty of design variables (laminate thicknesses) due to manufacturing has not been considered in this chapter. The design variable uncertainty will be discussed in Chapter 6. The other is that each MCS

realization, which includes 20 sets of (C, k, a, b, τ), represents the wind load variation in 20 years.

5.2 Reliability Analysis Examples

The reliability analyses of fatigue in a wind turbine blade at the initial design and the optimal design obtained from the deterministic design optimization (DDO) in Chapter 4 have been carried out in this section. Note that the number of laminate layers of the DDO optimum design was adjusted for manufacturing purposes in Section 4.3, and the adjusted blade model produces the same fatigue damage at selected hotspots compared to the original model. Thus, the probabilities of failure corresponding to the adjusted blade and the original blade are the same. For simplicity, the original blade model at the DDO optimum design is used for the reliability analysis because this model has the same laminate schedule as the initial design. The initial design and DDO optimum design are shown in Table 5.1.

Table 5.1 Initial Design and DDO Optimum Design

	DDO Initial Design	DDO Optimum Design
d_1 (mm)	4	3.99
d_2 (mm)	4	3.50
d_3 (mm)	4	4.45
d_4 (mm)	4	6.51
d_5 (mm)	4	2.00
d_6 (mm)	4	2.00
d_7 (mm)	4	7.06
d_8 (mm)	4	4.40
d_9 (mm)	4	2.00
d_{10} (mm)	4	4.73
d_{11} (mm)	4	5.31
d_{12} (mm)	2.5	3.85

In this example, the reliability analyses are carried out for all the 60,954 node-section points, not only for the selected hotspots. 50,000 realizations of **C**, **k**, **a**, **b**, and $\boldsymbol{\tau}$ have been generated for reliability analysis. As explained earlier, each realization is 20 sets of (C, k, a, b, τ). Then, 50,000 20-year fatigue damages have been calculated using Eq. (5.2) at each node-section point. The probability of fatigue life smaller than 20 years is then calculated by Eq. (5.3). The largest probability of failure among node-section points associated with one finite element (FE) node is selected as the probability of failure for that FE node. The reliability analysis results and discussion are provided in the following section. It is noted that all the 10-minute fatigue damage tables for 60,954 node-section points have already been obtained in the DDO procedure in Chapter 4. In this example, the probability tables for 50,000 realizations are generated, and the

generation requires only small computational cost. Therefore, the reliability analysis considering only wind load uncertainty is computationally affordable.

5.3 Reliability Analysis Results and Discussion

The reliability analysis has been carried out on the Linux machine (Dell PowerEdge R720 single server, 8 quad-core Xeon E5-2690 CPUs-32 cores, 2.9 GHz, 256 GB of RAM). Ten cores were used in parallel. Given the 10-minute fatigue damage tables of all 60,954 node-section points, the computational time for reliability analyses is about 7 hours. It is worth noting that the computational time for generating the 10-minute fatigue damage tables of all the node-section points using the same machine is about 14 hours. Thus, the total computational time would be about 21 hours for a given blade design using the machine.

The probability of fatigue failure contours of the initial design and the DDO optimum design are shown in Figure 5.2. As shown in Figure 5.2(a), the probability of failure of the initial design is 100%, especially at the rear parts of the aft shear web, forward shear web, and spar cap. The reason for the high probability of failure may be that the initial design of these parts is too small, as these parts often endure much larger aerodynamic wind loads than the root part. After the DDO procedure, the design variables d_4, d_7, and d_{12}, which are associated with the rear parts of the aft shear web, forward shear web, and spar cap, respectively, are increased by 62.8%, 76.5%, and 54%, respectively. The maximum probability of failure of the DDO optimum design is reduced to 49.9%, which occurs at the leading edge. Other areas with high probability of failure are isolated on the root of the blade as shown in Figure 5.2(b).

The significant reduction of the probability of fatigue failure from 100% at the initial design to 49.9% at the DDO optimum design indicates that the DDO procedure indeed reduces the probability of failure. However, the probability of failure of the DDO optimum design is still up to 49.9%, which obviously does not satisfy the target reliability

requirement. Thus, the reliability-based design optimization (RBDO) is necessary to further improve the fatigue reliability of the wind turbine blade.

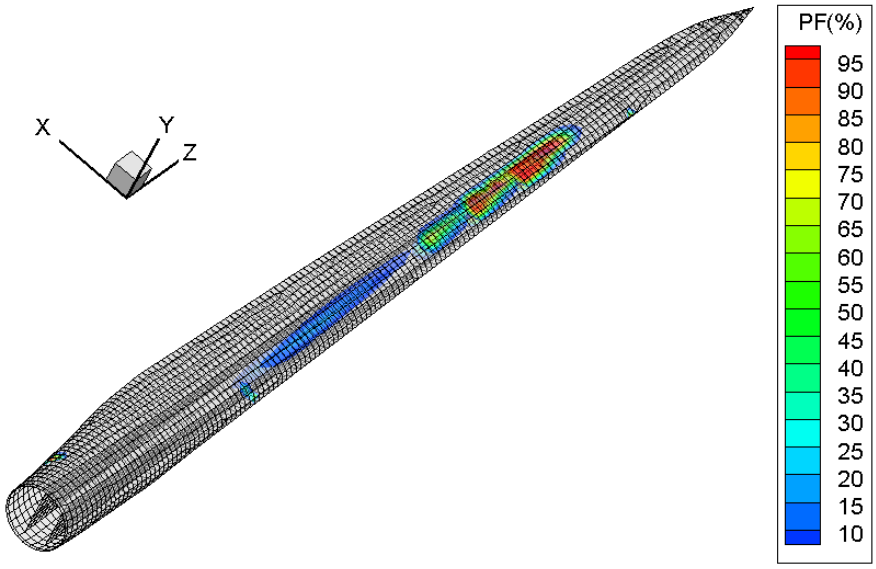

(a) Initial design

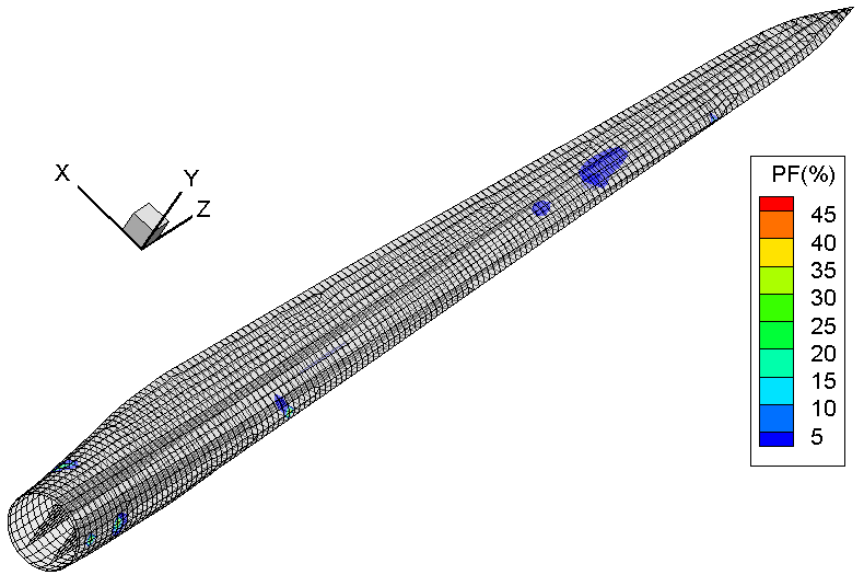

(b) DDO optimum design

Figure 5.2 Probability of Failure Contour of the Initial Design and the DDO Optimum Design

CHAPTER 6

RELIABILITY-BASED DESIGN OPTIMIZATION OF COMPOSITE WIND TURBINE BLADES UNDER WIND LOAD UNCERTAINTY

This chapter describes reliability-based design optimization (RBDO) of composite wind turbine blades under wind load uncertainty. A sampling-based RBDO method is used for the current problem because the design sensitivity of fatigue performance is complicated, nonlinear, and implicit. The fundamental ideas of the sampling-based RBDO are reviewed in Section 6.1. The RBDO problem of the composite wind turbine blade is explained in Section 6.2. The RBDO results and discussion are provided in Section 6.3.

6.1 Sampling-Based RBDO

6.1.1 Reliability Analysis

Reliability analysis is a procedure to calculate the probability of failure of a performance measure. The probability of failure, denoted by P_F, can be calculated using a multi-dimensional integral as (Madsen *et al.*, 1986)

$$P_F \equiv P\left[G(\mathbf{X}) > 0\right] = \int_{G(\mathbf{X})>0} f_{\mathbf{X}}(\mathbf{x})\, d\mathbf{x} \tag{6.1}$$

where $P[\cdot]$ represents a probability measure, $\mathbf{X} = [X_1, X_2, \ldots, X_N]^{\mathrm{T}}$ is an N-dimensional vector of input random variables X_i, $G(\mathbf{X})$ is a performance measure function such that $G(\mathbf{X}) > 0$ is defined as failure, and $f_{\mathbf{X}}(\mathbf{x})$ is a joint probability density function (PDF) of the input random variables. For real engineering problems, it is very difficult to evaluate Eq. (6.1) analytically, because the type of joint PDF is usually not Gaussian (multivariate normal distribution), and the performance measure $G(\mathbf{X})$ is nonlinear and implicit. To solve this kind of problem, there are two approaches: sensitivity-based reliability analysis and sampling-based reliability analysis. The sensitivity-based reliability analysis needs to

transform the random variable vector **X**, which follows a non-Gaussian PDF, into independent standard normal space (*U*-space) and approximate the nonlinear performance measure by Taylor series expansion in the *U*-space. The Taylor series expansion requires the sensitivity (gradient) of the performance measure $G(\mathbf{X})$, while the fatigue performance measure is a complicated, nonlinear, and implicit function. Thus, it is not suitable to use the sensitivity-based reliability analysis method for the fatigue reliability analysis of composite wind turbine blades. In contrast, the sampling-based reliability analysis does not require the sensitivity of the performance measure. Instead, it directly uses the Monte Carlo simulation (MCS) method, which applies samples drawn from the input joint PDF $f_{\mathbf{X}}(\mathbf{x})$. Thus, sampling-based reliability analysis is used for the reliability analysis method of composite wind turbine blades. The sampling-based reliability analysis is explained in Section 6.1.2.

6.1.2 Sampling-Based Reliability Analysis

The sampling-based reliability analysis calculates the probability of failure in Eq. (6.1) by applying the MCS method as (Lee *et al.*, 2011a; Lee *et al.*, 2011b)

$$\begin{aligned} P_F &= \int_{G(\mathbf{X})>0} f_{\mathbf{X}}(\mathbf{x})\, d\mathbf{x} = \int_{\mathbb{R}^N} I_{\Omega_F}(\mathbf{x})\, f_{\mathbf{X}}(\mathbf{x})\, d\mathbf{x} \\ &\cong \frac{1}{NMCS} \sum_{i=1}^{NMCS} I_{\Omega_F}\left[\mathbf{x}^{(i)}\right] \end{aligned} \tag{6.2}$$

where $\mathbf{x}^{(i)}$ is the *i*th realization of **X** (*i*th MCS sample), *NMCS* is the number of MCS samples, Ω_F is the failure domain such that $G(\mathbf{X}) > 0$, and $I_{\Omega_F}(\cdot)$ is an indicator function defined as

$$I_{\Omega_F}(\mathbf{x}) \equiv \begin{cases} 1, & \text{for } \mathbf{x} \in \Omega_F \\ 0, & \text{otherwise} \end{cases} \tag{6.3}$$

Although sampling-based reliability analysis does not require the sensitivity of the performance measure, the accuracy of the calculated probability of failure depends on the number of MCS samples *NMCS*. To calculate an accurate probability of failure, a large

number of MCS samples are required. Based on the 95% confidence interval of the estimated probability of failure, the percentage error can be defined as (Haldar and Mahadevan, 2000)

$$\varepsilon\% = \sqrt{\frac{\left(1 - P_F^{Tar}\right)}{NMCS \times P_F^{Tar}}} \times 200\% \tag{6.4}$$

where *NMCS* is the number of MCS samples and P_F^{Tar} is the target probability of failure. Equation (6.4) shows that *NMCS* should be increased to maintain the accuracy as the target probability of failure reduces. Because real engineering problems may involve expensive computational time, a large number of MCS samples could be unaffordable. In order to solve the computational issue, surrogate models are often used for sampling-based reliability analysis, as well as sampling-based RBDO. Sampling-based RBDO is explained in Section 6.1.3.

6.1.3 Sampling-Based RBDO

The general formulation of an RBDO problem can be expressed as

$$\begin{aligned} &\text{minimize} && \text{Cost}(\mathbf{d}) \\ &\text{subject to} && P\left[G_j\left(\mathbf{X}\right) > 0\right] \le P_{F_j}^{Tar},\ j = 1,\ldots,NC \\ & && \mathbf{d}^L \le \mathbf{d} \le \mathbf{d}^U,\quad \mathbf{d} \in \mathbb{R}^{NDV} \text{ and } \mathbf{X} \in \mathbb{R}^N \end{aligned} \tag{6.5}$$

where **X** is the *N*-dimensional random variable vector, **d** is the *NDV*-dimensional random design variable vector, G_j is the *j*th constraint function, $P[G_j(\mathbf{X}) > 0]$ is the probability of failure of the *j*th constraint, $P_{F_j}^{Tar}$ is the target probability of failure of the *j*th constraint, and *NC* is the number of constraints. The different dimensionalities of the design variable vector **d** and **X** is due to the fact that **X** contains random parameters, such as *C*, *k*, *a*, *b*, and τ, in addition to the random design variables. It is noted that a random design variable d_i is the mean μ_j of the corresponding random variable X_j. Also, standard deviation σ_j of X_j is linearly changing as random design variable d_i changes in this study.

In sampling-based RBDO, the probability of failure used in a probabilistic constraint is directly calculated using Eq. (6.2). The design sensitivity of the probabilistic constraint is derived using the score function and the MCS method (Lee *et al.*, 2011a; Lee *et al.*, 2011b). The design sensitivity is calculated during estimation of the probability of failure using the same MCS samples and constraint function evaluations. Thus, no extra MCS samples are required for calculating the design sensitivity.

Before derivation of the design sensitivity, the following four regularity conditions should be satisfied (Rubinstein and Shapiro, 1993; Rahman, 2009).

(1) The joint PDF fx($\mathbf{x};\boldsymbol{\mu},\boldsymbol{\sigma}$) is continuous.

(2) The mean $\mu_i \in M_i \subset \mathbb{R}$, $i = 1, \ldots, N$, where M_i is an open interval on $\mathbb{R}$.

(3) The partial derivative $\partial f_{\mathbf{X}}(\mathbf{x};\boldsymbol{\mu},\boldsymbol{\sigma})/\partial\mu_i$ exists and is finite for all $\mathbf{x}$ and μ_i. In addition, $P_F(\boldsymbol{\mu})$ is a differentiable function of $\boldsymbol{\mu}$.

(4) There exists a Lebesgue integrable dominating function $r(\mathbf{x})$ for all $\boldsymbol{\mu}$ such that

$$\left| h(\mathbf{x}) \frac{\partial f_{\mathrm{X}}(\mathbf{x};\boldsymbol{\mu},\boldsymbol{\sigma})}{\partial \mu_i} \right| \le r(\mathbf{x}) \tag{6.6}$$

where $h(\mathbf{x})$ is a general function and can be $I_{\Omega_F}(\mathbf{x})$.

With the four conditions satisfied, taking the partial derivative of Eq. (6.2) with respect to d_i yields (Lee *et al.*, 2011a; Lee *et al.*, 2011b)

$$\begin{aligned} \frac{\partial P_F(\boldsymbol{\mu})}{\partial d_i} &= \frac{\partial}{\partial d_i} \int_{\mathbb{R}^N} I_{\Omega_F}(\mathbf{x})\, f_{\mathrm{X}}(\mathbf{x};\boldsymbol{\mu},\boldsymbol{\sigma})\, d\mathbf{x} \\ &= \int_{\mathbb{R}^N} I_{\Omega_F}(\mathbf{x}) \frac{\partial f_{\mathrm{X}}(\mathbf{x};\boldsymbol{\mu},\boldsymbol{\sigma})}{\partial d_i} d\mathbf{x} \\ &= \int_{\mathbb{R}^N} I_{\Omega_F}(\mathbf{x}) \frac{\partial \ln f_{\mathrm{X}}(\mathbf{x};\boldsymbol{\mu},\boldsymbol{\sigma})}{\partial d_i} f_{\mathrm{X}}(\mathbf{x};\boldsymbol{\mu})\, d\mathbf{x} \\ &= E\left[I_{\Omega_F}(\mathbf{x}) \frac{\partial \ln f_{\mathrm{X}}(\mathbf{x};\boldsymbol{\mu},\boldsymbol{\sigma})}{\partial d_i} \right] \end{aligned} \tag{6.7}$$

The partial derivative of the log function of the joint PDF in Eq. (6.7) with respect to d_i is called the first-order score function for d_i and is denoted as

$$s_{d_i}^{(1)}(\mathbf{x};\boldsymbol{\mu},\boldsymbol{\sigma}) \equiv \frac{\partial \ln f_{\mathbf{X}}(\mathbf{x};\boldsymbol{\mu},\boldsymbol{\sigma})}{\partial d_i} \tag{6.8}$$

As shown in Eq. (6.7), the design sensitivity using the first-order score function does not depend on the sensitivity of the constraint function $G(\mathbf{X})$. Instead, it can be analytically obtained using the score function in Eq. (6.8). The reason is well illustrated in Figure 6.1. As shown in Figure 6.1, the horizontal axis is the random vector, and the vertical axis represents the jth constraint $G_j(\mathbf{X})$. The failure region of the constraint is set as $G_j(\mathbf{X}) > 0$, and the gray area in Figure 6.1 represents the probability of failure. When the random design variable $\mathbf{d}$ changes in the optimization process, the constraint function $G_j(\mathbf{X})$ holds its position, whereas the joint PDF $f_{\mathbf{X}}(\mathbf{x}; \boldsymbol{\mu}, \boldsymbol{\sigma})$ moves along with the random design variable. Consequently, the gray area, i.e., the probability of failure, changes as the random design variable changes. The rate of the probability of failure change is the same as the rate of the gray area change, which depends on the shape (slope) of the PDF on the limit state. The shape (slope) of the PDF on the limit state is related to the score function. This is the reason that the design sensitivity of the probabilistic constraint with respect to random design variable is related to the score function, not the sensitivity of the constraint function in Eq. (6.7).

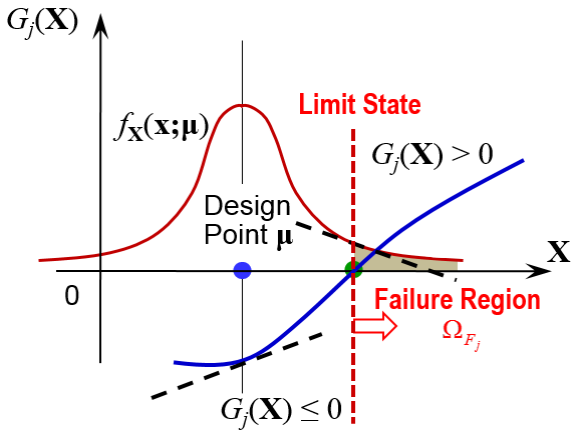

Figure 6.1 Design Sensitivity for Sampling-Based RBDO

In this study, the random design variables and random parameters are assumed to be independent. For statistically independent random variables, the first-order score function for d_i in Eq. (6.8) can be expressed with the marginal PDF as $f_{X_j}(x_j;\mu_j,\sigma_j)$ as

$$s_{d_i}^{(1)}\left(\mathbf{x};\boldsymbol{\mu},\boldsymbol{\sigma}\right) \equiv \frac{\partial \ln f_{\mathbf{X}}\left(\mathbf{x};\boldsymbol{\mu},\boldsymbol{\sigma}\right)}{\partial d_i} = \frac{\partial \ln f_{X_j}\left(x_j;\mu_j,\sigma_j\right)}{\partial \mu_j} + \frac{\partial \sigma_j}{\partial \mu_j}\frac{\partial \ln f_{X_j}\left(x_j;\mu_j,\sigma_j\right)}{\partial \sigma_j} \quad (6.9)$$

where the random design variable d_i corresponds to the random variable X_j. If the random variables are statistically correlated, the score function needs to consider the correction between random variables. Noh *et al.* used copula to consider the correlation between two random variables in RBDO problems (Noh *et al.*, 2009; Noh *et al.*, 2010), and Lee *et al.* derived the first-order score function of mean μ_j for both independent and correlated random variables (Lee *et al.*, 2011b). Cho *et al.* developed the first-order score functions for fixed coefficient of variation (CoV) problems for both independent and correlated random variables (Cho *et al.*, 2015).

6.2 RBDO of the Composite Wind Turbine Blade

This section explains the details of RBDO of the composite wind turbine blade, including random design variables, objective function, probabilistic constraints, and RBDO formulation. Sampling-based RBDO developed in the I-RBDO software is used to carry out the RBDO process starting from the DDO optimum design. Both the wind load uncertainty and manufacturing variability are considered in the RBDO process. The dynamic wind load uncertainty model provides uncertain wind load, while the manufacturing variability is represented by distributions of input random variables corresponding to random design variables. In order to release the computational burden and reduce the design of experiment (DoE) samples, local surrogate models of 10-minute fatigue damages are implemented during the RBDO process.

6.2.1 Random Design Variables

In RBDO, the uncertainty of composite laminate thickness due to the manufacturing process has been considered. Three assumptions are made for uncertainty of laminate thickness due to the manufacturing variability, as explained below.

(1) The variability of laminate thickness is assumed to follow normal distribution.

(2) The coefficient of variation (CoV) of the laminate thickness is assumed to be the same at different designs. Therefore, standard deviation of the laminate thickness changes linearly as design (thickness) changes. The CoV of the two composite materials used in the blade, QQ1 and P2B, are referred from the SNL/MSU/DOE Composite Material Fatigue Database (Mandell and Smaborsky, 2014).

(3) The randomness of laminate thickness in seven parts of the blade is assumed to be independent. Thus the laminate thicknesses in seven parts are represented by seven independent random variables, respectively.

The current RBDO process starts from the DDO optimum design obtained in Chapter 4. Based on the third assumption above, seven random design variables are used

in RBDO. As we consider the manufacturing variability, the laminate thickness becomes random. In order to bridge the seven RBDO random design variables and the twelve random thickness variables, a random variable transformation is used as explained below.

Let T_i, i = 1, 2, …, 12, be random variables corresponding to the twelve design variables d_i used in DDO. Using the first assumption above, T_i follows normal distribution $N(\mu_{T_i}, \sigma_{T_i})$, where μ_{T_i} and σ_{T_i} are the mean and standard deviation of T_i, respectively. The relationship between μ_{T_i} and σ_{T_i} can be expressed as

$$\sigma_{T_i} = c_{T_i} \mu_{T_i} \tag{6.10}$$

where c_{T_i} is the CoV of T_i. Based on the material type (see material type for each design variable in Table 4.5) and by referring SNL/MSU/DOE Composite Material Fatigue Database (Mandell and Smaborsky, 2014), it is obtained that $c_{T_i} = c^{\mathrm{QQ1}} = 0.0323$ for i = 1, 2, …, 11, and $c_{T_{12}} = c^{\mathrm{P2B}} = 0.0203$, where c^{QQ1} and c^{P2B} are CoV for QQ1 and P2B, respectively.

Let X_j, j = 1, 2, …, 7 be independent random variables used in RBDO. X_j follows normal distribution $N(\mu_{X_j}, \sigma_{X_j})$, where μ_{X_j} and σ_{X_j} are the mean and standard deviation of X_j, respectively. In order to reduce the number of random design variables from twelve to seven, multiple laminate thickness random variables in the same part are linked to one RBDO random variable X_j. For example, because T_2, T_3, and T_4 are representing laminate thicknesses in forward shear web, these three laminate thickness random variables are linked to one RBDO random variable X_2. Using the DDO optimum design d_i, i = 1, 2, …, 12 (Table 4.7), the transformation between laminate thickness random variables T_i and RBDO random design variables X_j is expressed as

$$T_i = \begin{cases} d_i X_i & , \quad i = 1 \\ d_i X_2 & , \quad i = 2,3,4 \\ d_i X_3 & , \quad i = 5,6,7,8 \\ d_i X_{i-5} & , \quad i = 9,10,11,12 \end{cases} \tag{6.11}$$

Because the relationship between T_i and X_j is linear, the CoV of X_j, c_{X_j}, is equal to the corresponding CoV of T_i. Thus, $c_{X_j} = c^{\mathrm{QQ1}} = 0.0323$ for $j = 1, 2, \ldots, 6$, and $c_{X_7} = c^{\mathrm{P2B}} = 0.0203$. Using the above random variable transformation (Eq. (6.11)), two results are produced, as explained below.

(1) At different RBDO designs, the CoV is constant for the RBDO design variable X_j, $j = 1, 2, \ldots, 7$.

(2) At different RBDO designs, the ratio of laminate thicknesses T_2, T_3, and T_4 will be the same as the ratio of design variables d_2, d_3, and d_4 of the DDO optimum design. Similarly, at different RBDO designs, the ratio of laminate thicknesses T_5, T_6, T_7, and T_8 will be the same as the ratio of design variables d_5, d_6, d_7, and d_8 of the DDO optimum design, etc.

In summary, the properties of random design variables for RBDO are listed in Table 6.1, where $\boldsymbol{\mu}^L$, $\boldsymbol{\mu}^O$, $\boldsymbol{\mu}^U$ are the normalized lower bound, mean, and upper bound of the random design variables in RBDO, respectively. μ_i, $i = 1, 2, \ldots, 7$, are RBDO design variables, each of which is the mean of random design variables X_i. The symbol $\boldsymbol{\mu}$ is used to represent the design in RBDO, in order to distinguish the design variable $\mathbf{d}$ used in DDO.

Table 6.1 Properties of Random Design Variables

Random Design Variable	Distribution	$\boldsymbol{\mu}^L$	$\boldsymbol{\mu}^O$	$\boldsymbol{\mu}^U$	CoV	Corresponding Part	Composite Material
μ_1	Normal	0.5010	1	2.0039	0.0323	Root	QQ1
μ_2	Normal	0.5707	1	1.7988	0.0323	Forward Shear Web	QQ1
μ_3	Normal	1.0000	1	1.8184	0.0323	Aft Shear Web	QQ1
μ_4	Normal	1.0000	1	4.0000	0.0323	Tip	QQ1
μ_5	Normal	0.4230	1	1.6919	0.0323	Leading Edge	QQ1
μ_6	Normal	0.3764	1	1.5057	0.0323	Trailing Edge	QQ1
μ_7	Normal	0.3898	1	1.1695	0.0203	Spar Cap	P2B

6.2.2 Objective Function

Similar to the DDO process, the normalized total cost of composite materials that are used in the blade is set as the objective function, which is expressed as

$$C(\boldsymbol{\mu}) = \left(4.18 \times 1000 \times \sum_{i}^{6} M_i^0 \frac{\mu_i}{\mu_i^0} + 11.70 \times 1000 \times M_7^0 \frac{\mu_7}{\mu_7^0} \right) \Big/ Cost^{DDO} \tag{6.12}$$

where M_i^0 (unit: ton) is the mass of the *i*th part at the RBDO initial design, i.e., the DDO optimum design; $\mu_i^0$is the normalized RBDO initial design corresponding to the *i*th part; μ_i is the current design corresponding to the *i*th part; i = 1, 2, …, 7; and $Cost^{DDO}$ is the RBDO initial cost, i.e., the cost of the DDO optimum design, which is $125,605 obtained in DDO. According to TPI Composites (2003), the material costs of QQ1 and P2B are $4.18/kg and $11.70/kg, respectively. It is worth noting that the cost of the carbon/glass-hybrid-fiber-reinforced laminate P2B is 2.8 times more expensive than that of QQ1, which is a glass-fiber-reinforced laminate. The objective function in Eq. (6.12) is minimized in the RBDO process.

6.2.3 Probabilistic Constraints

The probabilistic constraint is the probability of fatigue failure (fatigue life smaller than 20 years) at a selected hotspot being smaller than a target probability of failure P_F^{tar}=2.275%. The hotspots for RBDO are the node-section points where probability of fatigue failure is considered as the RBDO constraints. In this study, the event that fatigue life is smaller than 20 years is equivalent to that the 20-year fatigue damage is larger than 1. Thus, the 20-year fatigue damage is calculated first. Considering the manufacturing variability and wind load uncertainty, the 20-year fatigue damage can be calculated as

$$D_{20\,year}\left(\mathbf{X},\mathbf{C},\mathbf{k},\mathbf{a},\mathbf{b},\boldsymbol{\tau}\right)=\sum_{t=1}^{20}D_{1year}^{t}\left(\mathbf{X},C^{t},k^{t},a^{t},b^{t},\tau^{t}\right)$$
$$=52560\sum_{t=1}^{20}\sum_{i=1}^{12}\sum_{j=1}^{50}P_{VI}^{i,j}\left(v_{10}^{i},i_{10}^{j};C^{t},k^{t},a^{t},b^{t},\tau^{t}\right)D_{10}^{i,j}\left(\mathbf{X},v_{10}^{i},i_{10}^{j}\right) \tag{6.13}$$

where **X** is a random thickness vector; random vectors **C**, **k**, **a**, **b**, and **τ** contain 20 sets of (C, k, a, b, τ) as $\mathbf{C} = [C^1, C^2,\ldots, C^{20}]$, $\mathbf{k} = [k^1, k^2,\ldots, k^{20}]$, $\mathbf{a} = [a^1, a^2,\ldots, a^{20}]$, $\mathbf{b} = [b^1, b^2,\ldots, b^{20}]$, and $\boldsymbol{\tau} = [\tau^1, \tau^2,\ldots, \tau^{20}]$. The realizations of random vectors can be randomly drawn from the obtained PDFs of C, k, a, b, and τ in Section 3.2.

In this study, the probability of fatigue failure is calculated using a sampling-based reliability analysis introduced in Section 6.1.2. Using Eq. (6.13) and MCS, the probability of fatigue failure is calculated as

$$P\left(\text{Fatigue Life } < \text{ 20 years}\right)=P\left(D_{20\,year}\left(\mathbf{Y}\right)>1\right)=\int_{D_{20\,year}(\mathbf{Y})>1}f_{\mathbf{Y}}\left(\mathbf{y}\right)d\mathbf{y}$$
$$=\int_{\mathbb{R}^N}I_{\Omega_F}\left(\mathbf{y}\right)f_{\mathbf{Y}}\left(\mathbf{y}\right)d\mathbf{y}\cong\frac{1}{NMCS}\sum_{i=1}^{NMCS}I_{\Omega_F}\left[\mathbf{y}^{(i)}\right] \tag{6.14}$$

where $\mathbf{Y} = [\mathbf{X}, \mathbf{C}, \mathbf{k}, \mathbf{a}, \mathbf{b}, \boldsymbol{\tau}]$, and $\mathbf{y}^{(i)}$ is the i^{th} realization of **Y**. It is worth noting that the realization $\mathbf{y}^{(i)}$ is randomly generated based on the PDF of a random thickness vector **X** and the PDFs of random parameters (C, k, a, b, τ) in the dynamic wind load uncertainty model. The mean of the random thickness vector **X** is the random design vector **μ** in RBDO. Each realization $\mathbf{y}^{(i)}$ includes 20 sets of (C, k, a, b, τ), which represent the wind load variation in 20 years. *NMCS* is the number of realizations for MCS. Ω_F is the failure domain such that $D_{20\text{year}}(\mathbf{Y}) > 1$, and I_{Ω_F} is an indicator function defined as

$$I_{\Omega_F}\left(\mathbf{y}\right)=\begin{cases}1, & \text{for } \mathbf{y}\in\Omega_F\\ 0, & \text{otherwise}\end{cases} \tag{6.15}$$

By using Eq. (6.13) and Eq. (6.14), the probabilistic constraints can be expressed as

$$P\left(D_{20\,year}^{j}\left(\mathbf{Y}\right)>1\right)\le P_{F_j}^{\text{tar}}=2.275\%,\qquad j=1,\ldots,NC \tag{6.16}$$

where *NC* is the number of probabilistic constraints.

In order to accurately carry out RBDO with affordable computational time, two issues need to be addressed. The first issue is that the hotspots for RBDO probabilistic constraints need to be carefully selected. By using enough hotspots, the RBDO optimum design obtained in the future could guarantee that all the node-section points in the blade model satisfy the 2.275% target probability of failure requirement. However, too many hotspots increase the computational cost. The second issue is that the 20-year fatigue damage in Eq. (6.13) needs to be accurately and efficiently calculated, so that the probability of failure calculation in Eq. (6.14) will be accurate and efficient.

The method to select hotspots for RBDO is first explained. Three criteria are developed to select hotspots as listed below.

(1) Select the six node-section points, which correspond to the six active constraints at the DDO optimum design, as hotspots for RBDO.

(2) For each part, select a node-section point, which has the maximum one-year fatigue damage among all node-section points inside the part, as a hotspot for RBDO. The one-year fatigue damage is calculated by using the mean wind load (see Section 4.1).

(3) For each part, select a node-section point, which has the maximum one-year fatigue damage among all node-section points inside and adjacent to the part, as a hotspot for RBDO.

In order to better understand criteria 2 and 3 above, a demonstration about how to select hotspots based on criteria 2 and 3 is schematically shown in Figure 6.2. As shown in Figure 6.2, inside part A there are 20 node-section points, which are embraced by the box with the red-dashed boundary. Another five node-section points, which are inside part B, are adjacent to part A. For part A, if the node-section point *a* has the maximum one-year fatigue damage among the 20 node-section points inside part A, the node-section point *a* is selected as one hotspot based on criterion 2. By using criterion 3, if the

node-section point *b* has the maximum one-year fatigue damage among all the 25 node-section points embraced by the box with the blue-dashed boundary, the node-section point *b* is also selected as a hotspot. However, if the one-year fatigue damage of the node-section point *b* is smaller than that of the node-section point *a*, the node-section point *b* is not selected as a hotspot. Essentially, the reason that criterion 3 is included is because the design change in one part will not only affect the fatigue damage of node-section points inside the part but will also affect the fatigue damage of node-section points adjacent to the part.

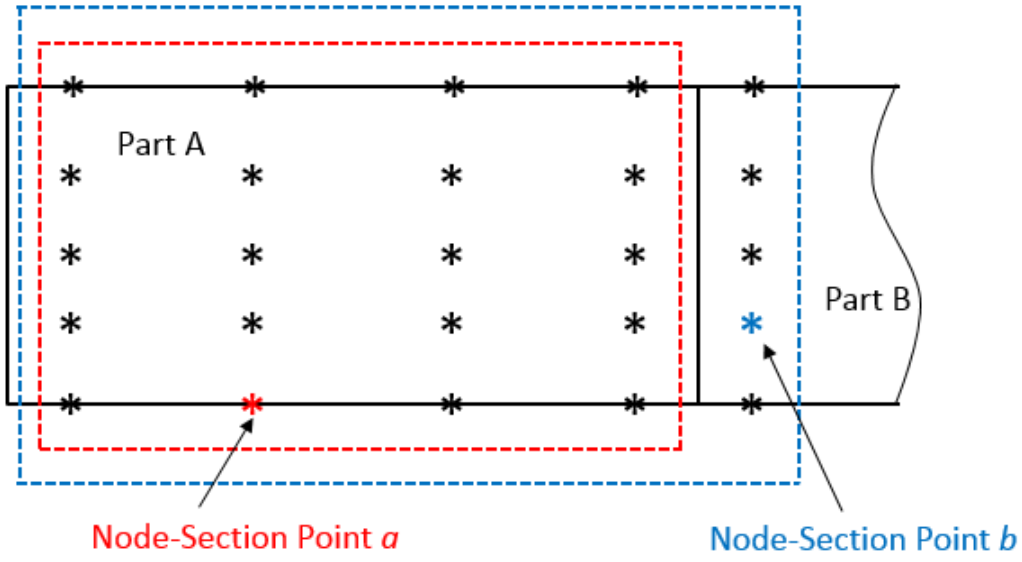

Figure 6.2 Demonstration of Hotspot Selection

In summary, nine hotspots are selected at the RBDO initial design. Information about the nine hotspots is provided in Table 6.2. The “Yes” in Table 6.2 indicates that the node-section point in the same row is selected because of the

criterion in the corresponding column. For example, six node-section points, which correspond to active constraints (one-year fatigue damage = 0.05) at the DDO optimum design, are selected based on criterion 1. Additional three node-section points are selected based on criteria 2 and 3. For example, node 61 - section point 15, which has the maximum fatigue damage in the root, is selected based on criterion 2. It is noted that some node-section points are selected by two or three criteria. The one-year fatigue damage calculated for identifying hotspots uses the mean wind load and does not consider the manufacturing variability. The nodal locations of the nine hotspots at the RBDO initial design are shown in Figure 6.3.

Similar to the hotspot selection during the DDO process in Section 4.2.3, the hotspots for RBDO are re-checked every four RBDO iterations. If new hotspots based on the three criteria are found, the newfound hotspots are included for RBDO constraints. If no new hotspot is found, the RBDO iteration is continued using the previously found hotspots.

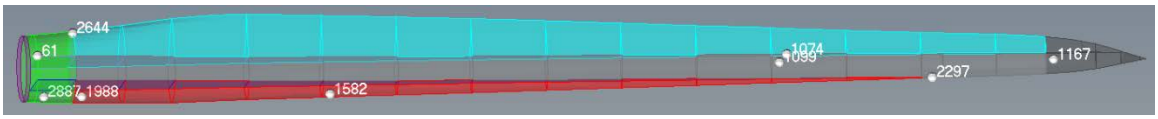

Figure 6.3 Nodal Locations of the Nine Hotspots at the RBDO initial Design

Table 6.2 Information about the Nine Hotspots Selected at RBDO Initial Design

RBDO Constraint	Nodal ID	Section Point ID	Belonging Part	Adjacent Part	One-year Fatigue Damage	Criterion 1	Criterion 2	Criterion 3
1	61	15	Aft Shear Web	Root	3.3182E−04		Yes	
2	1074	9	Trailing Edge	Aft Shear Web & Spar Cap	3.1771E−03			Yes
3	1099	9	Spar Cap		4.9965E−02	Yes	Yes	
4	1167	3	Tip		8.7192E−08		Yes	Yes
5	1582	9	Leading Edge		5.0001E−02	Yes	Yes	Yes
6	1988	15	Leading Edge		4.9990E−02	Yes		
7	2297	1	Forward Shear Web	Spar Cap	4.9991E−02	Yes	Yes	Yes
8	2644	1	Trailing Edge	Root	4.9996E−02	Yes	Yes	Yes
9	2887	1	Root		4.9968E−02	Yes	Yes	

The second issue that the 20-year fatigue damage needs to be accurately and efficiently calculated is well addressed by using local surrogate models of 10-minute fatigue damages. As shown in Eq. (6.13), the 20-year fatigue damage $D_{20year}(\mathbf{X}, \mathbf{C}, \mathbf{k}, \mathbf{a}, \mathbf{b}, \boldsymbol{\tau})$ is a function of 107 random variables, including seven random design variables plus 100 random parameters of (C, k, a, b, τ). With the large amount of dimensionality, it is extremely difficult to directly create an accurate surrogate model of the 20-year fatigue damage due to the high nonlinearity. In contrast, the 10-minute fatigue damage $D_{10}(\mathbf{X}, v_{10}, i_{10})$, which is a function of seven random thickness variables at given wind condition (v_{10}, i_{10}), is mildly nonlinear. However, it requires 12×50 = 600 surrogate models of 10-minute fatigue damage to calculate 20-year fatigue damage at one hotspot.

Two types of surrogate models have been created to investigate the efficiency and accuracy of 20-year fatigue damage calculation. One type is the surrogate model of one-year fatigue damage which is a function of seven random design variables and five random parameters of (C, k, a, b, τ). The other type is the surrogate model of the 10-minute fatigue damage which is a function of seven random design variables. The former type applies Dynamic Kriging method (Zhao *et al.*, 2011) with 1350 DoE samples to generate nine one-year fatigue damage surrogate models corresponding to nine hotspots on a local window. For the latter type, the Universal Kriging method (Zhao *et al.*, 2011) with 150 DoE samples is used to generate 12×50×No. of hotspots D_{10} surrogate models on the same local window. The size of the local window is 3 sigma, i.e., the lower bound of the local window is the mean of design minus 3 times the standard deviation, and the upper bound of the local window is the mean of design plus 3 times the standard deviation. The computational times for the former type and the latter type are 63 hours and 26 hours, respectively, using the same Linux server (72 GB of RAM, 12 cores, 2.9 GHz Intel CPU).

The accuracy of the two types of surrogate models at the RBDO initial design is checked by calculating the normalized root mean square error (NRMSE) of 20-year fatigue damage using 1000 testing samples. The steps to check accuracy of surrogate models of 10-minute fatigue damages are briefly listed below.

(1) Uniformly generate 1000 testing samples of $\mathbf{x}_i$, i = 1, 2, …, 1000, in the local window using Latinized Centroidal Voronoi Tessellation (LCVT) method (Basudhar *et al.*, 2012; Saka *et al.*, 2007).

(2) Calculate the 10-minute fatigue damage tables at the 1000 testing samples by using the 10-minute fatigue analysis procedure developed in Chapter 2. Calculate the approximated 10-minute fatigue damages at the 1000 testing samples by using the 10-minute fatigue damage surrogate models. Details about how to create a 10-minute fatigue damage table are provided in Section 4.1.1.

(3) Randomly generate 1000 sets of 20 (C, k, a, b, τ) based on the PDFs of (C, k, a, b, τ), which are provided at the end of Section 3.2. Using the 1000 sets of 20 (C, k, a, b, τ) , create 1000 × 20 wind load probability tables. Details about how to create a wind load probability table are provided in Section 4.1.1. Note that every 20 wind load probability tables are used for one testing sample to calculate one 20-year fatigue damage.

(4) Calculate the 20-year fatigue damages D_{20year}^{i}, i = 1, 2, …, 1000, by using the 10-minute fatigue damage tables and the wind load probability tables. Calculate the approximated 20-year fatigue damages $\widehat{D}_{20year}^{i}$, i = 1, 2, …, 1000, by using the approximated 10-mintue fatigue damage tables and the wind load probability tables.

(5) Calculate the NRMSE of 20-year fatigue damage with the following equation,

$$\text{NRMES} = \frac{\sqrt{\sum_{i}^{1000}\left(D_{20\,year}^{i} - \hat{D}_{20\,year}^{i}\right)^{2}}}{1000} \Big/ \left(\max\left(D_{20\,year}\right) - \min\left(D_{20\,year}\right)\right) \tag{6.17}$$

where max(D_{20year}) is the maximum of 20-year fatigue damages D_{20year}^{i}, and min(D_{20year}) is the minimum of 20-year fatigue damages D_{20year}^{i}, i = 1, 2, …, 1000.

For checking accuracy of surrogate model of one-year fatigue damage, the same 1000 testing samples and 1000 sets of 20 (C, k, a, b, τ) are used to first approximate 20,000 one-year fatigue damages using the surrogate model of one-year fatigue damage of one hotspot. Every 20 approximated one-year fatigue damages are summed to calculate one approximated 20-year fatigue damage. For example, approximated one-year fatigue damages 1 - 20 are used to calculate one approximated 20-year fatigue damage; approximated one-year fatigue damage 21 - 40 are used to calculate the next approximated 20-year fatigue damage. Likewise, 1000 approximated 20-year fatigue damage are obtained. The obtained 1000 approximated 20-year fatigue damage and the previously obtained 1000 20-year fatigue damages based the fatigue analysis procedure are used in Eq. (6.17) to calculate the NRMSE of 20-year fatigue damage. It is noting that the same 20 sets of (C, k, a, b, τ) are used to approximate a 20-year fatigue damage at one testing sample for two types of surrogate models.

Table 6.3 provides the calculated NRMSE of 20-year fatigue damage for the nine probabilistic constraints, which correspond to the nine hotspots listed in Table 6.2. As shown in Table 6.3, the NRMSE of 20-year fatigue damage using 10-minute fatigue damage surrogate model is smaller than that using one-year fatigue damage surrogate model for each hotspot, which indicates that using a larger number of surrogate models with smaller dimension could create more accurate 20-year fatigue damage results. Moreover, it only used 150 DoE samples to generate the 10-minute fatigue damage surrogate models, while the one-year fatigue damage surrogate models used 1350 DoE

samples. The maximum NRMSE using 10-minute fatigue damage surrogate model is equal to 5.792E−4 corresponding to the probabilistic constraint 3. Since the maximum NRMSE is smaller than 1E−3, the created 10-minute fatigue damage surrogate models are accurate for RBDO.

In order to require a small number of design of experiment (DoE) samples and accurately calculate 20-year fatigue damage, the approach for a large number of surrogate models with small dimension, i.e., surrogate models of 10-minute fatigue damage D_{10}, is used. As the RBDO iteration proceeds, new sets of D_{10} local surrogate models are created. The accuracy of the new sets of D_{10} surrogate models will not be checked in order to save computation time. However, the accuracy of D_{10} surrogate models will be checked at the final RBDO optimum design using the same method.

Table 6.3 NRMSE of 20-year Fatigue Damage of the Nine Hotspots at the RBDO Initial Design

Probabilistic Constraint	Nodal ID	Section Point ID	NRMSE of 20-year Fatigue Damage	
			One-year Fatigue Damage Surrogate Model	Ten-minute Fatigue Damage Surrogate Model
1	61	15	1.860E-02	5.532E−4
2	1074	9	2.231E-02	1.050E−5
3	1099	9	**4.119E-01**	**5.792E−4**
4	1167	3	2.248E-02	3.492E−5
5	1582	9	1.577E-02	4.200E−4
6	1988	15	1.330E-02	2.186E−4
7	2297	1	2.638E-02	4.411E−5
8	2644	1	1.137E-02	1.755E−4
9	2887	1	9.452E-03	2.052E−4

6.2.4 RBDO Formulation

The RBDO problem can be formulated as

$$\begin{aligned} &\text{minimize} && C(\boldsymbol{\mu}) \\ &\text{subject to} && P\left(D^{j}_{20\,year}\left(\mathbf{Y}\right)>1\right) \le P^{\text{tar}}_{F_j} = 2.275\%, \quad j=1,...,n \\ & && \boldsymbol{\mu}^{L} \le \boldsymbol{\mu} \le \boldsymbol{\mu}^{U}, \quad \boldsymbol{\mu} \in \mathbb{R}^{7} \text{ and } \mathbf{Y} \in \mathbb{R}^{107} \end{aligned} \tag{6.18}$$

where $\mathbf{Y}$ is the 107-dimensional random vector including seven random thickness variables and 20 sets of (C, k, a, b, τ); $\boldsymbol{\mu}$ is the 7-dimensional random design variable

vector; $C(\boldsymbol{\mu})$ is the normalized cost as shown in Eq. (6.12); and D_{20year}^{j} is the 20-year fatigue damage for the *j*th probabilistic constraint $P(D_{20year}^{j}(\mathbf{Y}) > 1) \leq P_{F_j}^{tar}$.

As explained in Section 6.2.1, the coefficient of variation (CoV) of a random thickness variable is constant in the RBDO process. In this study, RBDO with constant CoV of random variable, which has been developed by Cho *et al.* (2015), is applied to solve the RBDO problem. A flowchart of the RBDO process is shown in Figure 6.4. The basic steps to carry out the RBDO process including hotspot selection and surrogate model creation are listed below.

(1) Calculate the one-year fatigue damage of all node-section points of the blade at the RBDO initial design.

(2) Select the hotspots based on the three criteria in Section 6.2.3.

(3) Create (12×50×No. of hotspots) surrogate models of 10-minute fatigue damage with respect to seven design variables in the local window. The local surrogate models of 10-minute fatigue damage are used to calculate 20-year fatigue damage as shown in Eq. (6.13).

(4) Launch the RBDO procedure.

(5) For a new iteration and line search, create the local surrogate models of 10-minute fatigue damage at selected hotspots.

(6) After four design iterations, check hotspots in the design. If there are new hotspots, add their probability of fatigue failure to the probabilistic constraints and go to step 4. If the RBDO procedure converges under four iterations, go to step 7.

(7) Check the hotspots of the converged design. If there is no new hotspot, RBDO optimum design is obtained. If there are new hotspots, add their probability of fatigue failure to the constraints and go to step 4.

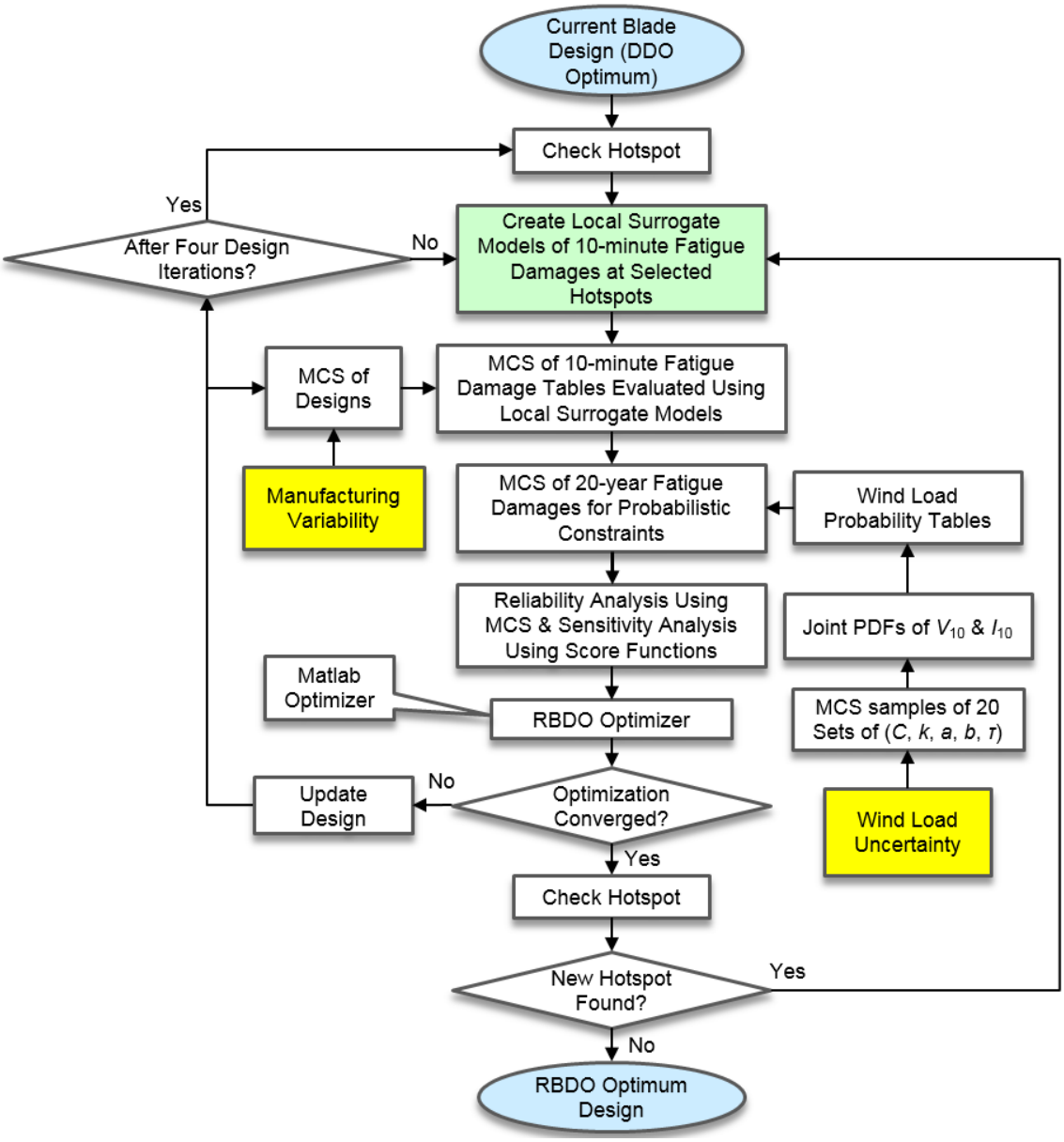

Figure 6.4 Flowchart of the RBDO Process

6.3 RBDO Results and Discussion

The RBDO process has been carried out on the Linux machine (Dell PowerEdge R720 single server, 8 quad-core Xeon E5-2690 CPUs-32 cores, 2.9 GHz, 256 GB of RAM). Fifteen cores were used in parallel. The entire RBDO process has twelve design iterations, twelve line searches, and four episodes of hotspot checking. Each design iteration or line search requires one set of local surrogate models and one reliability analysis. Thus, 25 sets of local surrogate models have been generated, including one set for the RBDO initial design. Accordingly, there are 25 reliability analyses for the RBDO initial design and designs at twelve iterations and twelve line searches. It takes about sixteen hours to generate one set of local surrogate model models and three hours for one reliability analysis. The computational time is about fifteen hours for checking hotspots at one design. The total computational time for the entire RBDO process is about 535 hours (22.3 days).

At the RBDO initial design, nine hotspots are identified as explained in Section 6.2.3. Since each RBDO constraint requires 600 local surrogate models of 10-minute fatigue damage, 5400 local D_{10} surrogate models are created at each RBDO iteration. There are 150 DoE samples are used to create one set of local D_{10} surrogate models. Existing DoE samples which are inside the new local window are applied to create local D_{10} surrogate models in the new local window. At the fourth RBDO iteration, a new hotspot has been found according to criteria 2 and 3 for hotspot selection. The new hotspot, which is node 2657 - section point 15, has the largest one-year fatigue damage among all node-section points inside and adjacent to the trailing edge part. All the previous selected nine hotspots are remained for design constraints. Thus there are ten hotspots after the fourth RBDO iteration. The nodal locations of the ten hotspots are shown in Figure 6.5. The wisely selected ten hotspots can well represent the fatigue critical areas in the blade model, so that the RBDO procedure does not require too many hotspots, which would cause computational burden. At the eighth and twelfth RBDO

iteration designs, hotspots are re-checked again but no new hotspots are found. The whole RBDO procedure is converged at the end of the twelfth iteration because the maximum relative change of random design variables, 7.35E−4, is less than its convergence criterion, 1E−3, and the relative maximum constraint violation, 3.01E−4, is less than its convergence criterion 1E−3. There are 1151 DoE samples are used in total.

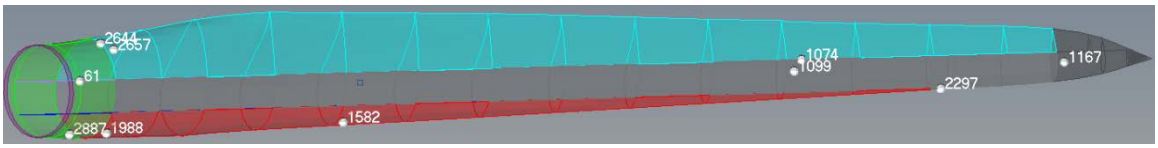

Figure 6.5 Nodal Locations of the Ten Hotspots after Fourth RBDO Iteration

The accuracy of local surrogate models of the RBDO optimum design is checked using another 1000 testing samples. Similar to checking the accuracy of local surrogate models at the RBDO initial design, the normalized root mean square error (NRMSE) of 20-year fatigue damage using the 1000 testing samples has been calculated and is provided in Table 6.4. As shown in Table 6.4, the maximum NRMSE is 8.264E−4, which is smaller than 1E−3. Thus, the created surrogate models are accurate surrogate models for reliability analysis at the RBDO optimum design.

Table 6.4 NRMSE of 20-year Fatigue Damage of the Ten Hotspots at the RBDO Optimum Design

Probabilistic Constraint	Nodal ID	Section Point ID	NRMSE
1	61	15	8.054E−4
2	1074	9	1.867E−5
3	1099	9	5.540E−4
4	1167	3	1.344E−5
5	1582	9	3.618E−4
6	1988	15	2.115E−4
7	2297	1	9.362E−5
8	2644	1	2.318E−4
9	**2657**	**15**	**8.264E−4**
10	2887	1	1.525E−4

Table 6.5 provides detailed histories of random design variables, normalized cost (objective function), true cost, mass, and the maximum probability of failure. As shown in Table 6.5, the maximum probability of fatigue failure has been reduced from 50.06% at the RBDO initial design to 2.28% at the RBDO optimum design, while the cost is only increased by 3.01%. In spite of the little cost increase, the mass of the RBDO optimum design is increased by 10.95% compared to that of the RBDO initial design. The reason for the large increase in mass is that more cheap but heavy composite material, QQ1, is applied at the RBDO optimum design than at the RBDO initial design. Meanwhile, the more expensive composite material, which is P2B corresponding to the random design

variable μ_7, at the RBDO optimum design is used 13.33% less than at the RBDO initial design. The hotspots are checked at four designs, which correspond to iterations 0, 4, 8, and 12 highlighted in bold in Table 6.5.

The histories of normalized cost and the maximum probability of failure are plotted in Figure 6.6. As shown in Figure 6.6, during the first three iterations, the cost was increased while the probability of failure was significantly reduced. The reason is that a significant amount of composite materials QQ1, which are controlled by the random design variables μ_1 - μ_6, were added in the blade in order to increase the fatigue resistance of the blade model. There is a peak at the fourth iteration of the history of the probability of failure. The reason is that a new hotspot was identified at the fourth iteration, and it has a larger probability of failure than do the existing hotspots. Between the fourth iteration and eighth iteration, both the cost and the maximum probability of failure were reduced, which shows that by tuning the seven random design variables, the RBDO process could find a more cost-effective and reliable design. The RBDO process converged at the twelfth iteration.

Table 6.5 RBDO Histories of Random Design Variables, Normalized Cost, True Cost, Mass, and the Maximum Probability of Failure

Iteration	Random Design Variables							Normalized Cost	True Cost ($)	Mass (ton)	Maximum Probability of Failure (%)
	μ_1	μ_2	μ_3	μ_4	μ_5	μ_6	μ_7				
0	1.0000	1.0000	1.0000	1.0000	1.0000	1.0000	1.0000	1.0000	125605.49	21.8050	50.06
1	1.0644	1.1397	1.0414	1.0000	1.0455	1.0288	1.0163	1.0316	129576.55	22.5735	12.78
2	1.0933	1.3309	1.1619	1.0000	1.0498	1.0410	0.9986	1.0424	130935.77	23.0962	5.86
3	1.1060	1.4853	1.3095	1.0205	1.0485	1.0455	0.9650	1.0407	130721.00	23.4183	3.29
4	1.1162	1.5568	1.4252	1.0645	1.0566	1.0472	0.9508	1.0440	131130.63	23.6742	22.22
5	1.1175	1.5434	1.4483	1.0783	1.0601	1.0718	0.9399	1.0430	131011.32	23.7669	7.75
6	1.1195	1.5430	1.5127	1.1182	1.0644	1.0862	0.9252	1.0410	130750.47	23.8683	3.67

Table 6.5 RBDO Histories of Random Design Variables, Normalized Cost, True Cost, Mass, and the Maximum Probability of Failure (Continued)

Iteration	Random Design Variables							Normalized Cost	True Cost ($)	Mass (ton)	Maximum Probability of Failure (%)
	μ_1	μ_2	μ_3	μ_4	μ_5	μ_6	μ_7				
7	1.1231	1.5462	1.7120	1.2414	1.0770	1.1130	0.8850	1.0344	129926.80	24.1181	2.93
8	1.1305	1.5827	1.8184	1.3069	1.1027	1.1067	0.8588	1.0280	129127.31	24.2184	2.51
9	1.1296	1.5885	1.8184	1.3001	1.0986	1.0977	0.8620	1.0281	129139.96	24.1862	2.40
10	1.1313	1.5850	1.8184	1.3021	1.1035	1.0931	0.8650	1.0293	129284.61	24.1869	2.31
11	1.1328	1.5741	1.8184	1.2983	1.1124	1.0914	0.8662	1.0298	129346.03	24.1883	2.30
12	1.1333	1.5708	1.8184	1.2990	1.1148	1.0913	0.8667	1.0301	129384.14	24.1917	2.28

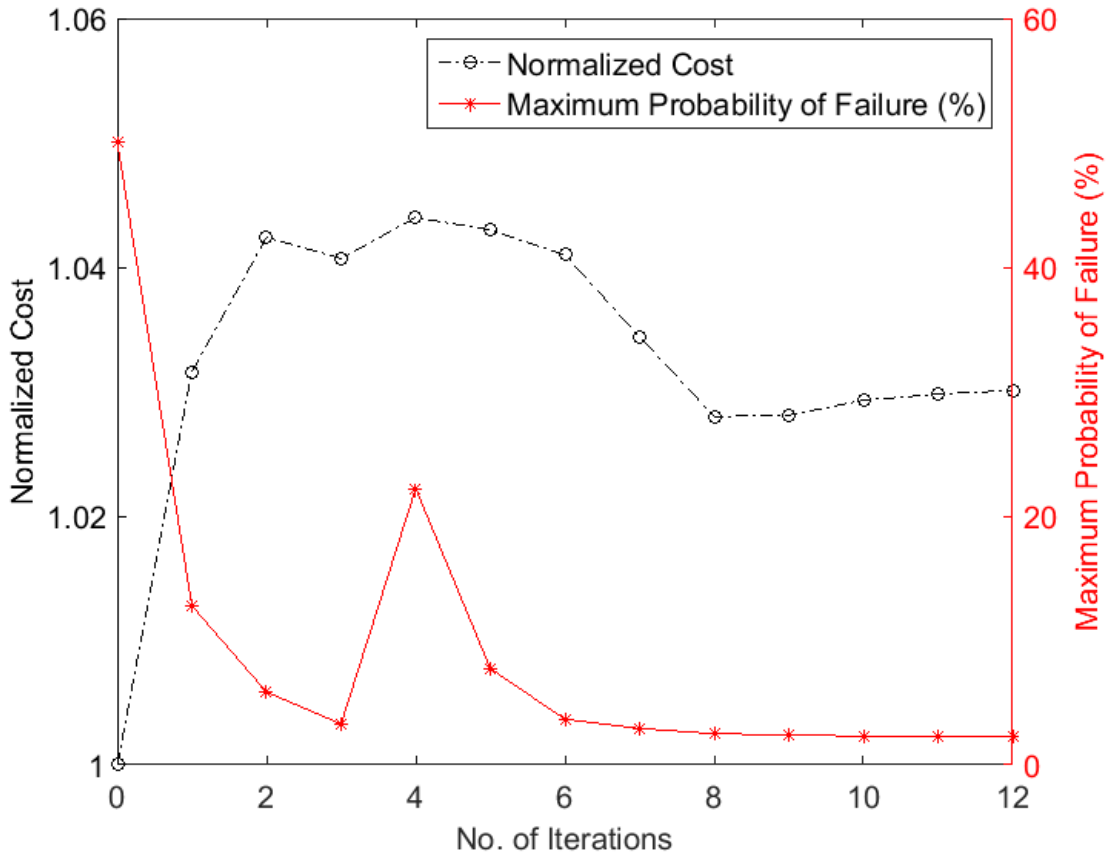

Figure 6.6 Histories of Normalized Cost and the Maximum Probability of Failure

Table 6.6 provides the history of probability of failure of each probabilistic constraint. The maximum probability of failure at each iteration is highlighted in bold. As shown in Table 6.6, the probabilistic constraint with the maximum probability of failure is changing as the design iteration proceeds, which indicates the most probable fatigue failure location is changing as the design changes. The probabilistic constraint 9 has no results of probability of failure at iterations 0, 1, 2, and 3 because the corresponding hotspot node 2657 - section point 15 (see Table 6.4) was not identified until checking the hotspots at the fourth design iteration. The largest probability of failure at the RBDO

optimum design occurs at the probabilistic constraint 3, which corresponds to the hotspot node 1099 - section point 9. In order to distinguish the probabilities of failure at the last iteration, three decimal places are used for the probabilities of failure at the last iteration.

Table 6.7 compares the laminate thickness, true cost, mass, and probability of failure of three designs: the initial design, the DDO optimum design, and the RBDO optimum design. In order to compare the laminate thickness, all three designs apply the same laminate schedule, which is provided in Table 2.4. As shown in Table 6.7, at the RBDO optimum design, the laminate thicknesses t_4, t_7, and t_8 corresponding to forward shear panels 10-13, aft shear web panels 9-12, and aft shear web panels 13-16, respectively, are significantly increased by 155.75%, 221%, and 100%, respectively, compared to those at the initial design. Along the direction from root to tip, the blade becomes thinner and thinner, which makes the two shear webs inside the blade shell decrease the height significantly close to the blade tip. Thus, a much thicker rear part of the two shear webs is necessary in order to keep the shear webs stiff, which makes the blade more fatigue reliable. This explains why the laminate thicknesses t_4, t_7, and t_8 are significantly increased. Table 6.7 also shows that the laminate thicknesses, for example t_5 and t_6, are decreased from the initial design to the DDO optimum design, but increased from the DDO optimum design to the RBDO optimum design, in order to satisfy the target 2.275% probability of failure requirement. The laminate thickness in spar cap, which is made of expensive composite material P2B, is decreased by 13.51% from the DDO optimum design to the RBDO optimum design in order to minimize the cost.

Table 6.6 History of Probability of Failure of Each Probabilistic Constraint

Probability of Failure (%)		Probabilistic Constraints									
		1	2	3	4	5	6	7	8	9	10
Iterations	0	0	0.36	5.18	0	**50.06**	49.10	18.75	49.37		48.74
	1	0	0.22	3.05	0	1.52	**12.78**	7.97	12.47		12.38
	2	0	0.17	2.55	0	0.02	**5.86**	4.02	4.76		4.91
	3	0	0.18	2.52	0	0.00	**3.29**	2.81	2.80		2.99
	4	0	0.15	2.19	0	0.00	2.39	2.22	2.40	**22.22**	2.41
	5	0	0.16	2.25	0	0.01	2.30	2.27	0.56	**7.75**	2.42
	6	0	0.16	2.26	0	0.02	2.29	2.27	0.21	**3.67**	2.45
	7	0	0.14	2.25	0	1.62	2.37	2.25	0.03	0.66	**2.93**
	8	0	0.15	**2.51**	0	2.39	0.52	2.30	0.02	0.81	2.28
	9	0	0.15	**2.40**	0	2.39	0.66	2.24	0.05	1.58	2.37
	10	0	0.15	**2.31**	0	2.30	0.53	2.23	0.07	2.15	2.29
	11	0	0.15	**2.30**	0	2.25	0.34	2.27	0.08	2.27	2.28
	12	0	0.144	**2.281**	0	2.262	0.304	2.279	0.076	2.265	2.277

Table 6.7 Comparison of the Initial Design, the DDO Optimum Design, and the RBDO Optimum Design

Laminate Thickness (mm)	Corresponding Panel	Initial Design	DDO Optimum Design	RBDO Optimum Design
t_1	Root	4	3.99	4.52
t_2	Forward Shear Panels 1-5	4	3.50	5.50
t_3	Forward Shear Panels 6-9	4	4.45	6.99
t_4	Forward Shear Panels 10-13	4	6.51	**10.23**
t_5	Aft Shear Web Panels 1-4	4	2.00	3.64
t_6	Aft Shear Web Panels 5-8	4	2.00	3.64
t_7	Aft Shear Web Panels 9-12	4	7.06	**12.84**
t_8	Aft Shear Web Panels 13-16	4	4.40	**8.00**
t_9	Tip	4	2.00	2.60
t_{10}	Leading Edge	4	4.73	5.27
t_{11}	Trailing Edge	4	5.31	5.80
t_{12}	Spar Cap	2.5	3.85	3.33
True Cost ($)		95494.42	125605.49	129384.14
Mass (ton)		18.4981	21.8048	24.1918
Probability of Failure (%)		100	50.06	2.28

The mass distributions of the initial design, the DDO optimum design, and the RBDO optimum design have been studied. Table 6.8 compares the mass of each part in

the blade model. As shown in Table 6.8, the DDO procedure significantly increases the mass of the trailing edge and the spar cap by 24.31% and 53.91%, respectively, in order to satisfy the 20-year fatigue life constraint. The RBDO procedure significantly increases the mass of the forward shear web and the aft shear web by 46.38% and 62.20%, respectively, while the mass of the spar cap is reduced by 13.33% through the RBDO procedure. This finding indicates that the two shear webs play important role in fatigue reliability of the blade. By enhancing the two shear webs, the thickness of the spar cap, which is made of expensive composite material P2B, can be reduced in order to decrease the total cost. The total mass of the DDO optimum design and the RBDO are increased by 17.88% and 30.78%, respectively, comparing that of the initial design. The reasons of the significant increment of the total mass may be that:

(1) The composite material QQ1 is too heavy to be used in the blade model;
(2) The defined laminate schedule in the blade model may not be an optimal laminate schedule;
(3) The assumed constant life diagram (CLD) in shear direction may be too conservative comparing to the true CLD in shear direction;
(4) The objective function of both DDO and RBDO only considers the total cost of composite materials. The optimization procedure tends to apply more heavy but cheap material QQ1, instead of light but expensive material P2B, in order to minimize the cost.

The total mass is an important factor when designing wind turbine blades. It is not only related to the material cost, but also affect the blade transportation, energy generation, and blade control. For designing a cost-effective, reliable, and light wind turbine blade, optimization problem could use a multi-objective function including both the mass and the cost, and subject to probabilistic constraints. This work may be carried out in the future.

Table 6.9 compares section mass in the spanwise direction of the initial design, the DDO optimum design, and the RBDO optimum design. Figure 6.7 clearly shows the distributed section mass in the spanwise direction of the above three design, as well as the 5-MW NREL reference wind turbine blade (Jonkman *et al.*, 2009b). The larger section mass of the DDO optimum design and the RBDO optimum design comparing that of the 5-MW NREL reference wind turbine blade could also be because of the above four points.

Table 6.8 Comparison of Part Mass of the Initial Design, the DDO Optimum Design, and the RBDO Optimum Design

Part Name	Part Mass (ton)		
	Initial Design	DDO Optimum Design	RBDO Optimum Design
Root	1.5246	1.5217	1.7245
Forward Shear Web	2.1122	2.1400	**3.1326**
Aft Shear Web	2.4529	1.9422	**3.1503**
Tip	0.2230	0.1115	0.1448
Leading Edge	2.4673	2.8191	3.0814
Trailing Edge	5.7002	**7.0862**	7.5984
Spar Cap	4.0180	**6.1840**	**5.3598**
Total Mass (ton)	18.4981	21.8048	24.1918

Table 6.9 Comparison of Blade Section Mass of the Initial Design, the DDO Optimum Design, and the RBDO Optimum Design

Section ID	Section Width (m)	Blade Span	Section Mass (ton)			Section Mass Density (kg/m)		
			Initial Design	DDO Optimum Design	RBDO Optimum Design	Initial Design	DDO Optimum Design	RBDO Optimum Design
1	2.7333	0.022	2.0380	1.9013	2.2922	745.6291	695.6097	838.6171
2	2.7333	0.067	1.6483	1.7733	2.0501	603.0344	648.7656	750.0545
3	2.7333	0.111	1.5611	1.7082	1.9556	571.1488	624.9563	715.4619
4	4.1000	0.167	2.4718	2.8557	3.1502	602.8756	696.5107	768.3363
5	4.1000	0.233	2.0328	2.4036	2.6069	495.7976	586.2532	635.8205
6	4.1000	0.300	1.4220	1.7081	1.8367	346.8200	416.6032	447.9715
7	4.1000	0.367	1.2988	1.5844	1.6791	316.7907	386.4347	409.5285
8	4.1000	0.433	1.1972	1.4790	1.5480	292.0105	360.7259	377.5529
9	4.1000	0.500	1.0975	1.4973	1.6432	267.6793	365.1954	400.7856
10	4.1000	0.567	0.9171	1.2806	1.4239	223.6918	312.3376	347.2886
11	4.1000	0.633	0.7514	1.0430	1.1696	183.2579	254.4022	285.2758
12	4.1000	0.700	0.5874	0.8082	0.9190	143.2674	197.1119	224.1487
13	4.1000	0.767	0.5221	0.6889	0.7494	127.3410	168.0162	182.7750
14	4.1000	0.833	0.4365	0.5793	0.6043	106.4681	141.2854	147.3954
15	2.7333	0.889	0.2622	0.3490	0.3628	95.9165	127.6862	132.7236
16	2.7333	0.933	0.1950	0.1155	0.1626	71.3273	42.2498	59.4857
17	2.7333	0.978	0.0590	0.0295	0.0383	21.5856	10.7928	14.0193

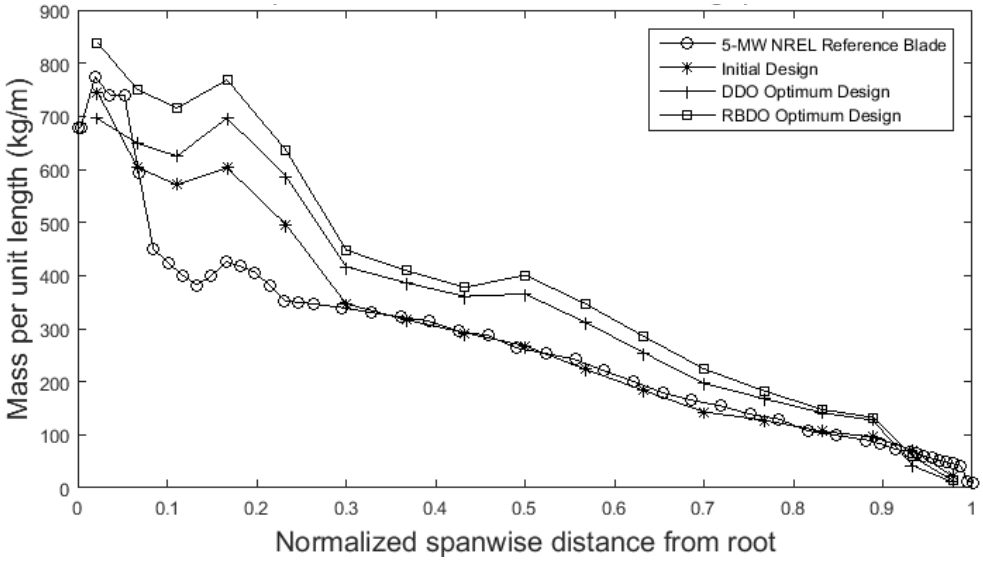

Figure 6.7 Comparison of Sectional Mass Distribution

One question about the obtained RBDO optimum design is that are all the node-section points at the RBDO optimum design satisfying the target reliability requirement when considering both wind load uncertainty and manufacturing variability? The difficulty to solve this question is that it is very computationally expensive to carry out reliability analysis for all node-section points considering both wind load uncertainty and manufacturing variability. On the other side, it is affordable to check the probability of failure only considering wind load uncertainty and to calculate one-year fatigue damage under the mean wind load for all node-section pints, as explained in Chapter 5 and Chapter 4, respectively. Moreover, by studying the results of the probability of failure considering only wind load uncertainty and the results of the one-year fatigue damage under the mean wind load, it is possible to see if there are any missing node-section

points which may violate the target reliability requirement when considering both wind load uncertainty and manufacturing variability. Details are explained as follows.

Both the probability of failure considering only wind load uncertainty and the one-year fatigue damage under the mean wind load for all node-section points at the RBDO optimum design have been calculated. Table 6.10 provides the probability of failure PF_{wind} considering only wind load uncertainty, the probability of failure $PF_{wind+manu.}$ considering both wind load uncertainty and manufacturing variability (surrogate models for 10-minute fatigue damage are used), and the one-year fatigue damage under the mean wind load at the selected ten hotspots. In order to study the fatigue effect due to different load types, i.e., wind load, gravity load, and centrifugal load, the one-year fatigue damage due to wind load, gravity load, and centrifugal load is also calculated. In Table 6.10, the $D_{1year\text{-}wind}$, $D_{1year\text{-}gravity}$, and $D_{1year\text{-}centrifugal}$ indicate that only aerodynamic wind load, gravity load, and centrifugal load, respectively, is applied when calculating 10-minute fatigue damage. The D_{1year} in Table 6.10 indicates that all three kinds of load are applied when calculating 10-minute fatigue damage. For each case, the mean wind load probability table is used to calculate the one-year fatigue damage. Some interesting findings extracted from Table 6.10 are listed below.

(1) The probability of failure considering both wind load uncertainty and manufacturing variability is either larger than or equal to the probability of failure considering only wind load uncertainty. The larger probability of failure considering both wind load uncertainty and manufacturing variability is due to that the manufacturing variability introduces design uncertainty, which increases the probability of failure. The equal probability of failure occurs at two hotspots, node 61 - section point 15 and at node 1167 - section point 3, which have 0 probability of failure due to very small fatigue damage as indicated in Table 6.10. For these two hotspots, the RBDO optimum design is in a very safe region and the

introduction of manufacturing variability does not increase the probability of failure at all.

(2) The node-section points, for which the wind load dominates the overall fatigue damage, have probability of failure considering both wind load uncertainty and manufacturing variability close to that considering only wind load uncertainty. For example, the wind load dominates the fatigue damage at node 1074 - section point 9 as shown in Table 6.10. The $PF_{wind+manu}$ is close to PF_{wind} at this hotspot. The reason of the closed probability of failure is that the introduction of manufacturing variability has non-significant influence on the probability of failure calculation since the wind load dominates the overall fatigue damage. This finding also holds true for node 1099 - section point 9 and node 2297 - section point 1 as shown in Table 6.10.

(3) The node-section points, for which the gravity load dominates the overall fatigue damage, may have much larger probability of failure considering both wind load uncertainty and manufacturing variability than that considering only wind load uncertainty. The reason is that manufacturing variability is directly related to the gravity load uncertainty. By introducing the manufacturing variability for gravity load dominated node-section points, the probability of failure may increase significantly due to the gravity load uncertainty. For example, the gravity load dominated hotspots, node 1582 - section point 9, node 2657 - section point 15, and node 2881- section point 1 in Table 6.10, have much larger $PF_{wind+manu}$ than PF_{wind}.

Among the probabilities of failure of all node-section points considering only wind load uncertainty, the largest probability of failure is 2.19% and occurs at node 2297 - section point 1. Thus, there is no node-section point at the RBDO optimum design violating the target probability of failure if only wind load uncertainty is considered. It is also found that node 1582 - section point 9, node 2657 - section point 15, node 2644 -

section point 1, and node 1988 - section point 15 are top 4 gravity load dominated node-section points among all node-section points by ordering one-year fatigue damage. These four node-section points have already been selected as hotspots. In addition, another four node-section points are selected at the RBDO optimum design to calculate the probability of failure considering both wind load uncertainty and manufacturing variability. The four node-section points are not close to any selected hotspots. The one-year fatigue damages corresponding to the four node-section points are among the top 50 large one-year fatigue damages of all node-section points. In order to calculate the probability of failure, the surrogate models for 10-minute fatigue damages of the four node-section points are generated first. Then, the probability of failure considering both wind load uncertainty and manufacturing variability are calculated using the surrogate models. The probability of failure and one-year fatigue damage of the additional four node-section points are shown in Table 6.11. As shown in Table 6.11, all of the additional tested four node-section points satisfy the target 2.275% probability of failure considering both wind load uncertainty and manufacturing variability.

In summary, all of the node-section points at the RBDO optimum design satisfying the target reliability requirement when considering both wind load uncertainty and manufacturing variability.

Table 6.10 Probability of Failure and One-Year Fatigue Damage of the Ten Hotspots at the RBDO Optimum Design

Probabilistic Constraint	Nodal ID	Section Point ID	PF_{wind} (%)	$PF_{wind+manu.}$ (%)	D_{1year}	$D_{1year\text{-}wind}$	$D_{1year\text{-}gravity}$	$D_{1year\text{-}centrifugal}$
1	61	15	0	0	1.5069E−04	8.1900E−09	1.2625E−06	0
2	1074	9	0.142	0.144	1.7648E−03	1.7060E−03	6.2187E−14	0
3	1099	9	2.030	2.281	2.2703E−02	2.0688E−02	7.9918E−32	0
4	1167	3	0	0	2.8135E−09	2.8780E−09	2.5181E−18	0
5	**1582**	**9**	0.032	2.262	4.2083E−02	3.3417E−06	3.8250E−04	0
6	1988	15	0	0.304	3.2140E−02	1.1997E−08	8.4981E−04	0
7	2297	1	2.190	2.279	9.2256E−03	1.0096E−02	3.6445E−14	0
8	2644	1	0	0.076	3.2918E−02	3.4867E−13	1.9853E−03	0
9	**2657**	**15**	0.010	2.265	3.6132E−02	7.2627E−10	3.1032E−04	0
10	**2887**	**1**	0	2.277	2.9686E−02	2.2233E−09	1.0124E−03	0

Table 6.11 Probability of Failure and One-Year Fatigue Damage of the Four Selected Node-Section Points at the RBDO Optimum Design

Nodal ID	Section Point ID	PF_{wind} (%)	$PF_{wind+manu.}$ (%)	D_{1year}	$D_{1year\text{-}wind}$	$D_{1year\text{-}gravity}$	$D_{1year\text{-}centrifugal}$
1572	9	0	0.0005	1.7646E−02	1.2086E−05	1.2990E−04	0
1961	12	0	0.0055	2.5300E−02	2.3344E−08	1.2439E−03	0
2527	3	0	0	2.7234E−02	5.6960E−11	2.4691E−04	0
2872	1	0	0.0045	1.7703E−02	3.1586E−10	1.4755E−04	0

CHAPTER 7

CONCLUSIONS AND FUTURE RECOMMENDATIONS

In this chapter, the conclusions of the thesis and future recommendations are presented. Section 7.1 presents conclusions about the fatigue analysis procedure for composite wind turbine blades, the dynamic wind load uncertainty model, the deterministic design optimization (DDO) procedure, reliability analysis, and the reliability-based design optimization (RBDO) procedure. Future recommendations are provided in Section 7.2

7.1 Conclusions

A fatigue analysis procedure for composite wind turbine blades, including wind field simulation, aerodynamic analysis, detailed stress analysis, and fatigue damage evaluation, is proposed in this thesis. The wind field simulation applies the Veers' method to simulate 10-minute wind field realizations based on a 10-minute mean wind speed V_{10} and a 10-minute turbulence intensity I_{10}. Using the simulated wind field realization, an aerodynamic analysis method is proposed to efficiently generate quasi-physical blade surface pressures for subsequent stress and fatigue analysis. The proposed aerodynamic analysis method is based on the computationally efficient aerodynamic analysis of airfoil and the wind turbine blade. In addition to the wind load, gravity load and centrifugal load are included in the detailed stress analysis of a composite wind turbine blade. A fatigue failure criterion is proposed to deal with non-proportional multi-axial stress states in which more than one stress component is operative and stress components are out of phase with each other. Finally, 10-minute fatigue damages at blade node-section points are calculated using the proposed fatigue failure criterion. Previous works considered the mean wind speed in fatigue damage calculation. In this study, atmospheric turbulence is also taken into account by I_{10} as well as V_{10}. This study also provides a detailed composite laminate schedule and fatigue constant life diagrams for

the realistic composite wind turbine blade model, which has been used in DDO, reliability analysis, and RBDO.

A dynamic wind load uncertainty model has been developed using 249 groups of measured wind data. The wind load uncertainty model involves both the annual wind load variation and the wind load variation in a large spatiotemporal range. The annual wind load variation is represented by the joint probability density function (PDF) of V_{10} and I_{10}. In order to properly represent the joint PDF of V_{10} and I_{10}, the marginal distributions and copula types (correlation) for V_{10} and 10-minute standard deviation of wind speed Σ_{10} have been studied. Based on the 249 groups of measured wind data, the best fit marginal distribution types of V_{10} and Σ_{10} are identified to be Weibull distribution and Gamma distribution, respectively. The best copula type for V_{10} and Σ_{10} is also identified as Gumbel. The joint PDF of V_{10} and I_{10} is derived from the joint PDF of V_{10} and Σ_{10}. The wind load variation in a large spatiotemporal range is represented by the PDFs of five parameters C, k, a, b, and τ, which determine the joint PDF of V_{10} and I_{10}. Using the 249 sets of (C, k, a, b, τ), the best fit PDFs of C, k, a, b, and τ are identified to be log-logistic distribution, normal distribution, generalized extreme value distribution, Weibull distribution, and extreme value distribution, respectively. Using two different sets of (C, k, a, b, τ), a case study has been carried out to predict the fatigue damage of the developed composite wind turbine blade. The case study results show that the calculated maximum one-year fatigue damage using one set of (C, k, a, b, τ) is 5.32 times larger than that when the other set is used. This finding confirms that the wind load variation in the lifespan of wind turbine blades plays a critical role in blade fatigue analysis and that the uncertain wind load must be considered in the fatigue reliability analysis of wind turbines.

Using the dynamic wind load uncertainty model, a mean wind load is generated to use for the DDO of the composite wind turbine blade. In order to generate the mean wind load, a wind condition table, which consists of 600 combinations of V_{10} and I_{10}, is

constructed. The selected 600 combinations of V_{10} and I_{10} cover a wide range of wind conditions. For each wind condition, a mean probability using the developed wind load uncertainty model and Monte Carlo simulation (MCS) is calculated. Consequently, a mean wind load probability table, which represents the mean wind load, is created. Applying the mean wind load, 20-year fatigue damages at blade node-section points are calculated for DDO constraints. By fine-tuning the laminate thickness design variables, a DDO optimum design was successfully obtained through the DDO procedure. At the DDO optimum design, the fatigue life of the blade model is increased 49,999 times over that of the initial design, while the cost is 31.53% larger than that of the initial design.

The reliability analysis method of the composite wind turbine blade under wind load uncertainty is then proposed using the sampling-based reliability analysis method. The MCS method simulates uncertain wind load using the proposed wind load uncertainty model. The reliability analysis estimates the probability that a wind turbine could survive 20 years of target lifespan. The reliability analyses of the initial design and the DDO optimum design are taken as examples. The reliability analysis has been carried out for all 60,954 node-section points of the blade. Thus the probability of failure of each node-section point is obtained. Detailed probability of failure contours have been obtained for both the initial design and the DDO optimum design. Using the probability of failure contour, the largest probability of failure can be located. The reliability analysis results show that the probability of failure considering only wind load uncertainty is reduced from 100% at the initial design to 49.9% at the DDO optimum design, which indicates that the DDO procedure indeed reduces the probability of failure. However, the high probability of failure (49.9%) at the DDO optimum design also indicates that RBDO is necessary to further improve the fatigue reliability of the composite wind turbine blade.

Finally, the RBDO procedure for composite wind turbine blades considering both wind load uncertainty and manufacturing variability is developed. The wind load uncertainty model could provide realistic uncertain wind load through the designed 20-

year lifespan. The fundamental theories of sampling-based RBDO with fixed coefficient of variation (CoV) are reviewed. The twelve random thickness variables are linked to seven random design variables by using the DDO optimum design result. The RBDO objective function is normalized cost based on true cost at the DDO optimum design. Three criteria for identifying hotspots are created. The probabilistic constraints are probability of fatigue failure at the selected hotspots. During the RBDO iterations, local surrogate models of 10-minute fatigue damages are created to calculate 20-year fatigue damage efficiently and accurately. Using the surrogate models, probability of fatigue failure is calculated considering both wind load uncertainty and manufacturing variability. The obtained RBDO optimum design reduces the maximum probability of failure from 50.06% at the RBDO initial design to 2.28% at the RBDO optimum design. This research demonstrates that applying RBDO methods to wind turbine blades could provide reliable and yet economical designs considering wind load uncertainty. The developed wind load uncertainty, the reliability analysis method, and the RBDO methods could be applicable to other wind turbine components, such as rotor hub, gears, and bearings.

7.2 Future Recommendations

Three areas are recommended to be improved in fatigue analysis procedure in the future. Firstly, consider the aero-elastic effect when calculating detailed wind pressure load. In the proposed fatigue analysis procedure, the aerodynamic wind pressure is generated based on the computationally efficient aerodynamic analysis of airfoil and the wind turbine blade. The blade is un-deformed when calculating the aerodynamic wind load for fatigue analysis within AeroDyn. Thus, the aero-elastic effect has not been considered in fatigue reliability analysis. For future research, new methods/procedures may be developed to consider the aero-elastic effect of the blade and calculate detailed wind pressure for finite element analysis. Secondly, address the non-deterministic

relationship between section load coefficient (C_l, C_d, C_m) and effective angle of attack. Due to that the current fatigue analysis procedure cannot afford the computational time for each individual realization, a fifth-order polynomial regression model is used. However, as found in this study, the aerodynamic coefficients are not deterministic functions of angle of attack. This non-deterministic relationship could generate varied wind pressure at the same angle of attack, which makes the fatigue analysis more complex and affect the reliability of the blade. Thirdly, introduce a turbine control model to fatigue analysis. In current fatigue analysis, the rotational speed is assumed to be constant for different wind conditions. In reality, the control system keeps the rotational speed, as well as the power out, within a certain range. In addition, the blade pitch control is one of the most important factors affecting aerodynamic loads over the range of wind conditions considered. The computational time issue of involving these improvements needs to be well addressed before carrying out reliability analysis and RBDO. One potential method may be using high-performance computing (HPC) to carry out parallel computation.

Recommendations for the wind load uncertainty model are also provided. The proposed wind load uncertainty model utilizes 249 groups of measured wind data. If more wind data is available, the developed dynamic wind load uncertainty model could generate more realistic uncertainty wind load for reliability analysis and RBDO. At the current state, due to lack of wind data over 20 years, the random variables of C, k, a, b, and τ are assumed to be independent. In other words, the wind load variation over years is assumed to be independent. In reality, the wind load distribution in one year at a location is probably close to the wind load distribution in the following years at the same location. That means there is a correlation between the wind loads in years. In the future, the correlation among random variables of C, k, a, b, and τ may be studied. For example, by adding the correlation into the wind load uncertainty model, the correlation between wind loads generated from sequential years may be considered.

REFERENCES

ABAQUS/CAE Version 6.11, "Abaqus User Documentations," Dassault Systems, 2011.

ASTM Committee, "Standard Practices for Cycle Counting in Fatigue Analysis," ASTM International, West Conshohocken, PA, USA, 2005.

ASTM Committee, "Standard Practices for Statistical Analysis of Linear or Linearized Stress-Life (S-N) and Strain-Life (ε-N) Fatigue Data. Designation: E739-91 (Reapproved 2004)," ASTM International, West Conshohocken, PA, USA, 2004.

Basudhar, A., Dribusch, C., Lacaze, S. and Missoum, S., "Constrained Efficient Global Optimization with Support Vector Machines," *Structural and Multidisciplinary Optimization*, Vol. 46, No. 2, pp. 201-221, 2012.

Bottasso, C.L., Campagnolo, F., Croce, A., Dilli, S., Gualdoni, F., and Nielsen, M.B., "Structural optimization of wind turbine rotor blades by multilevel sectional/multibody/3D-FEM analysis," *Multibody Syst Dyn*, Vol. 32, pp. 87-116, 2014.

Breitung, K., "Asymptotic Approximations for Multinormal Integrals," *Journal of Engineering Mechanics*, Vol. 110, No. 3, pp. 357-366, 1984.

Burton, T., Jenkins, N., Sharpe, D., and Bossanyi, E., *Wind Energy Handbook, 2nd Ed*., John Wiley & Sons, Ltd., West Sussex, UK, 2011.

Carta, J.A., Ramirez, P., and Velazquez, S., "A Review of Wind Speed Probability Distributions Used in Wind Energy Analysis Case Studies in the Canary Islands," *Renewable and Sustainable Energy Reviews*, Vol. 13, No.5, pp. 933-955, 2009.

Cho, H., Choi, K.K., Lee, I., and Gorsich, D., "Design Sensitivity Method for Sampling-Based RBDO with Fixed COV," *41st ASME Design Automation Conference*, August 02-05, 2015, Boston, MA.

Corecell™ M-Foam the Marine Foam [online database]. URL: http://www.gurit.com/gurit-corecell-m.aspx

Drela, M., and Youngren, H., "XFOIL 6.9 User Guide," Massachusetts Institute of Technology, Cambridge, MA, 2001.

Fossum, P. K., FrØyd, L., and Dahlhaug, O. G., "Design and Fatigue Performance of Large Utility-Scale Wind Turbine Blades," *Journal of Solar Energy Engineering*, Vol.; 135, No. 3, pp. 1-11, 2013.

Found, M.S., and Quaresimin, M., "Two-stage fatigue loading of woven carbon fibre reinforced laminates," *Fatigue and Fracture of Materials Engineering and Structures*, Vol. 26, No. 1, pp. 17-26, 2003.

Fujii, T., and Lin, F., "Fatigue behavior of a plain-woven glass fabric laminate under tension/torsion biaxial loading," *Journal of Composite Materials*, Vol. 29, pp. 573-590, 1995.

Gamstedt, E. K., and Sjögren, B. A., "An experimental investigation of the sequence effect in block amplitude loading of cross-ply composite laminates," *International Journal of Fatigue*, Vol. 24, pp. 437-446, 2002.

Giovanni, P., Nicola, C., Quagliarella, D., Witteveen, J., and Iaccarino, G., "Wind Turbine Performance Analysis Under Uncertainty," *49th AIAA Aerospace Science Meeting including the New Horizons Forum and Aerospace Exposition*, 4-7 January 2011, Orlando, Florida.

Germanischer Lloyd, "Guideline for the Certification of Wind Turbines Edition 2010," Hamburg, Germany, 2010.

Glauert, H., *Airplane Propellers in Aerodynamic Theory (W.F. Durand, ed.), Division L, Chapter XI*, Springer Verlag, Berlin, 1935.

Griffith, D. T., Ashwill, T. D., "The Sandia 100-meter All-glass Baseline Wind Turbine Blade: SNL 100-00," SANDIA REPORT SAND2011-3779, Sandia National Laboratories, USA, 2011.

Grujicic, M., Arakere, G., Pandurangan, B., Sellappan, V., Vallejo, A., and Ozen, M., "Multidisciplinary Design Optimization for Glass-Fiber Epoxy-Matrix Composite 5 MW Horizontal-Axis Wind-Turbine Blades," *Journal of Materials Engineering and Performance*, Vol. 19, pp. 1116-1127, 2010.

Haldar, A., and Mahadevan, S., *Probability, Reliability and Statistical Methods in Engineering Design*, John Wiley & Sons, New York, NY, 2000.

Hansen, M. O. L., *Aerodynamics of Wind Turbines, 2nd Ed.*, Earthscan, London, UK, 2008.

Hansen, M. O. L., Sørensen, J. N., Voutsinas, S., Sørensen, N., and Madsen, H.A., "State of the art in wind turbine aerodynamic and aeroelasticity," *Progress in Aerospace Sciences*, Vol. 42, pp. 285-330, 2006.

Harris, B., *Fatigue in composites: Science and technology of the fatigue response of fibre-reinforced plastics*, CRC Press, Boca Raton, FL, USA, 2003.

Hashin, Z., Rotem, A., "A fatigue failure criterion for fibre-reinforced materials," *Journal of Composite Materials*, Vol. 7, pp. 448-464, 1973.

Hasofer, A. M., and Lind, N. C., "Exact and Invariant Second-Moment Code Format," *Journal of the Engineering Mechanics Division, ASCE*, Vol. 100, No. 1, pp. 111-121, 1974.

Hohenbichler, M., and Rackwitz, R., "Improvement of Second-Order Reliability Estimates by Importance Sampling," *Journal of Engineering Mechanics*, Vol. 114, No. 12, pp. 2195-2199, 1988.

Hoog, R.V., McKean, J. W., and Craig, A. T., *Introduction to Mathematical Statistics, 6th Ed.*, Pearso Prentice Hall, Upper Saddle River, NJ, 2005.

Hu, W., Choi, K. K., Gaul, N. J., Cho, H., and Zhupanska, O., "Reliability Analysis of Wind Turbine Blades for Fatigue Life Under Wind Load Uncertainty," *14th AIAA/ISSMO Multidisciplinary Analysis and Optimization Conference*, Indianapolis, Indiana, September 17-19, 2012a.

Hu, W., Han, I., Park, S. C., and Choi, D.H., "Multi-objective Structural Optimization of A HAWT Composite Blade Based on Ultimate Limit State Analysis," *Journal of Mechanical Science and Technology*, Vol. 26, No. 1, pp. 129-135, 2012b.

Hu, W., Park, D., Choi, D.H., "Structural optimization procedure of a composite wind turbine blade for reducing both material cost and blade weight," *Engineering Optimization*, Vol. 45, pp. 1469-1487, 2013a.

Hu, Z., Li, H., Du, X., and Chandrashekhara, K., "Simulation-based time-dependent reliability analysis for composite hydrokinetic turbine blades," *Structural and Multidisciplinary Optimization*, Vol. 47, pp. 765-781, 2013b.

HyperWorks 11.0, HyperWorks Desktop User's Guide, Altair Engineering, Inc., 2012.

IEC 61400-1, "Wind Turbines - Part I: Design Requirements, 3rd Ed.," International Electrotechnical Commission, 2005.

Jones, R.M., *Mechanics of Composite Materials 2nd Ed.*, Taylor & Francis, Inc., Philadelphia, 1999.

Jonkman, B. J., "TurbSim User's Guide: Version 1.50," NREL/TP-500-46198, Golden, CO, National Renewable Energy Laboratory, 2009a.

Jonkman J., Butterfield, S., Musial, W., and Scott, G., "Definition of a 5-MW Reference Wind Turbine for Offshore System Development," NREL/TP-500-38060, Golden, CO, National Renewable Energy Laboratory, 2009b.

Jonkman, J. M., and Buhl, M.L., "FAST User's Guide," NREL/EL-500-38230, Golden, CO, National Renewable Energy Laboratory, 2005.

Kong, C., Bang, J., and Sugiyama, Y., "Structural Investigation of Composite Wind Turbine Blade Considering Various Load Cases and Fatigue Life," *Energy*, Vol. 30, pp. 2101-2114, 2005.

Kong, C., Kim, T., Han, D., and Sugiyama, Y., "Investigation of Fatigue Life for A Medium Scale Composite Wind Turbine Blade," *International Journal of Fatigue,* Vol. 28, pp. 1382-1388, 2006.

Lee, I., Choi, K. K., and Gorsich, D., "System reliability-based design optimization using the MPP-based dimension reduction method," *Structural and Multidisciplinary Optimization*, Vol. 41, No. 6, pp. 823-839, 2010.

Lee, I., Choi, K. K., and Zhao, L., "Sampling-Based RBDO using the Stochastic Sensitivity Analysis and Dynamic Kriging Method," *Structural and Multidisciplinary Optimization*, Vol. 44, No. 3, pp. 299-317, 2011a.

Lee, I., Choi, K. K., Noh, Y., Zhao, L., and Gorsich, D., "Sampling-Based Stochastic Sensitivity Analysis using Score Functions for RBDO Problems with Correlated Random Variables," *Journal of Mechanical Design*, Vol. 133, No. 2, pp. 021003, 2011b.

Leishman, J. G., and Beddoes, T. S., "A semi-empirical model for dynamic stall," *Journal of the American Helicopter Society,* Vol. 34, No. 3, pp. 3-17, 1989.

Li, Y., Paik, K. J., Xing, T., Carrica, P. M., "Dynamic overset CFD simulations of wind turbine aerodynamics," *Renewable Energy*, Vol. 37, pp. 285-298, 2012.

Li, Y., Castro, A. M., Sinokrot, T., Prescott, W., Carrica, P. M., "Coupled multi-body dynamics and CFD for wind turbine simulation including explicit wind turbulence," *Renewable Energy*, Vol. 76, pp. 338-361, 2015.

Liu, Y., and Mahadeva, S., "A unified multiaxial fatigue damage model for isotropic and anisotropic materials," *International Journal of Fatigue,* Vol. 29, pp. 347-359, 2007.

Liu, Y., and Mahadevan, S., "Probabilistic fatigue life prediction of multidirectional composite laminates," *Composite Structures*, Vol. 69, pp. 11-19, 2005.

Madsen, H. O., Krenk, S., and Lind, N. C., *Methods of Structural Safety*, Prentice-Hall, Englewood Cliffs, NJ, 1986.

Mandell, J.F., Samborsky, D.D., SNL/MSU/DOE Composite Material Fatigue Database Mechanical Properties of Composite Materials for Wind Turbine Blades Version 23.0, Montana State University – Bozeman, 2014.

Manuel, L., Veers, P.S., and Winterstein S.R., "Parametric Models for Estimating Wind Turbine Fatigue Loads for Design," *2001 ASME Wind Energy Symposium, 20th, Aerospace Sciences Meeting and Exhibit, 39th*, Reno, NV, January 11-14, 2001.

Manwell, J. F., Mcgowan, J. G., and Rogers, A. L., *Wind Energy Explained: Theory, Design and Application 2nd Ed.*, John Wiley & Sons, Ltd., West Sussex, UK, 2009.

MATLAB R2012a, Matlab Help, The MathWorks, Inc., February 2012.

Messac, A., Chowdhury, S., and Zhang, J., "Modeling the Uncertainty in Farm Performance Introduced by the Ill-predictability of the Wind Resource," *6th AIAA Theoretical Fluid Mechanics Conference*, Honolulu, Hawaii, June 27-30, 2011.

Mishnaevsky, L. J., Brøndsted, P., Nijssen, R., Lekou, D. J., and Philippidis, T. P., "Materials of large wind turbine blades: recent results in testing and modeling," *Wind Energy*, Vol. 15, pp. 83-97, 2012.

Moriarty, P. J., and Hansen, A. C., "AeroDyn Theory Manual," NREL/EL-500-3881, Golden, CO, National Renewable Energy Laboratory, December 2005.

Moriarty, P. J., Holley, W. E., and Butterfield, S. P., "Extrapolation of Extreme and Fatigue Loads Using Probabilistic Methods," NREL/TP-500-34421, Golden, CO, National Renewable Energy Laboratory, 2004.

Noda, M., Flay, R.G.J., "A simulation model for wind turbine blade fatigue loads," *Journal of Wind Engineering and Industrial Aerodynamics*, Vol. 83, pp. 527-540, 1999.

Noh, Y., Choi, K. K., and Du, L., "Reliability-Based Design Optimization of Problems with Correlated Input Variables using a Gaussian Copula," *Structural and Multidisciplinary Optimization*, Vol. 38, No. 1, pp. 1-16, 2009.

Noh, Y., Choi, K. K., and Lee, I., "Identification of Marginal and Joint CDFs Using Bayesian Method for RBDO," *Structural and Multidisciplinary Optimization*, Vol. 40, No. 1, pp. 35-51, 2010.

Nussbaumer, A., Borges, L., and Davaine, L., *Fatigue Design of Steel and Composite Structures*, European Convention for Constructional Steelwork, Berlin, 2011.

OPTIMAT BLADES, "Reliable optimal use of materials for wind turbine rotor blades," contract no. ENK6-CT-2001-00552, 2001-2006. URL: http://www.wmc.eu/optimatblades.php.

Philippidis, T. P., and Vassilopoulos, A. P., "Complex stress state effect on fatigue life of GRP laminates. Part II, Theoretical formulation," *International Journal of Fatigue*, Vol. 24, pp. 825-830, 2002.

Philippidis, T. P., and Vassilopoulos, A. P., "Life prediction methodology for GFRP laminates under spectrum loading," *Composites Part A: applied science and manufacturing*, Vol. 35, pp. 657-666, 2004.

Pro/ENGINEER Wildfire 5.0, Pro/E Help Manual, Parametric Technology Corporation, 2009.

Puck, A., Kopp, J., and Knops, M., "Guidelines for the determination of the parameters in Puck's action plane strength criterion," *Composites Science and Technology*, Vol. 62, pp. 371-378, 2002.

Ragan P., Manuel, L., "Comparing Estimates of Wind Turbine Fatigue Loads using Time-Domain and Spectral Methods," *Wind Engineering*, Vol. 31, pp. 83-99, 2007.

Rahman, S., "Stochastic Sensitivity Analysis by Dimensional Decomposition and Score Functions," *Probabilistic Engineering Mechanics*, Vol. 24, No. 3, pp. 278-287, 2009.

Rahman, S., and Wei, D., "A Univariate Approximation at most Probable Point for Higher-Order Reliability Analysis," *International Journal of Solids and Structures*, Vol. 43, No. 9, pp. 2820-2839, 2006.

Ronold, K. O., Jakob, W. H., and Christensen, C. J., "Reliability-Based Fatigue Design of Wind-Turbine Rotor Blades," *Engineering Structure*, Vol. 21, pp. 1101-1114, 1999.

Ronold, K. O., and Christensen, C. J., "Optimization of a design code for wind-turbine rotor blades in fatigue," *Engineering Structure*, Vol. 23, pp. 993-1004, 2001.

Rubinstein, R. Y., and Shapiro, A., *Discrete Event Systems: Sensitivity Analysis and Stochastic Optimization by the Score Function Method*, Wiley, New York, NY, 1993.

Saka, Y., Gunzburger, M. and Burkardt, J., "Latinized, Improved LHS, and CVT Point Sets in Hypercubes," *International Journal of Numerical Analysis and Modeling*, Vol. 4, No. 3-4, pp. 729-743, 2007.

Shinozuka, M. and Jan, C. M., "Digital Simulation of Random Processes and Its Applications," *Journal of Sound and Vibration*, Vol. 25, No. 1, pp. 111-128, 1972.

Shokrieh, M. M., and Rafiee, R., "Simulation of Fatigue Failure in A Full Composite Wind Turbine Blade," *Composite Structures*, Vol. 74, pp. 332-342, 2006.

Söker, H., and Kensche, C., "Introducing Low Cycle Fatigue in IEC Standard Range Pair Spectra," *Proceeding of the German Wind Energy Conference DEWEK*, Wilhelmshaven, Germany, 2004.

Spera, D. A., *Wind Turbine Technology Fundamental Concepts of Wind Turbine Engineering*, ASME, New York, 1998.

Sun, X. S., Haris, A., Tan, V. B. C., Tay, T. E., Narasimalu, S., and Della, C.N., "A multi-axial fatigue model for fiber-reinforced composite laminates based on Puck's criterion," *Journal of Composite Materials*, Vol. 46, pp. 449-469, 2012.

TPI Composites, Inc., "Innovative Design Approaches for Large Wind Turbine Blades," Sandia Report SAND2003-0723, March 2003.

Tu, J., Choi, K. K., and Park, Y. H., "A New Study on Reliability-Based Design Optimization," *Journal of Mechanical Design*, Vol. 121, No. 4, pp. 557-564, 1999.

Tu, J., Choi, K. K., and Park, Y. H., "Design Potential Method for Robust System Parameter Design," *AIAA Journal*, Vol. 39, No. 4, pp. 667-677, 2001.

Van Paepegem W., and Degrieck, J., "Effects of Load Sequence and Block Loading on the Fatigue Response of Fibre-reinforced Composites," *Mechanics of Advanced Materials and Structures*, Vol. 9, No. 1, pp. 19-35, 2002.

Vassilopoulos, A. P., *Fatigue life prediction of composites and composite structures*, CRC Press, Boca Raton, FL, USA, 2010.

Vassilopoulos, A. P., and Keller, T., *Fatigue of Fiber-reinforced Composites*, Springer, London, 2011.

Veers, P.S., "Three-Dimensional Wind Simulation," SANDIA Report SAND88-0152 UC-261, Sandia National Laboratories, USA, 1988.

Veers, P. S., Winterstein, S. R., "Application of Measured Loads to Wind Turbine Fatigue and Reliability Analysis," *ASME Wind Energy Symposium-Held in conjunction with the AIAA Aerospace Sciences Meeting*, Reno, Nevada, January 1997.

Veers, P. S., Ashwill, T. D., Sutherland, H. J., Laird, D. L., Lobitz, D. W., Griffin, D. A., Mandell, J. F., Musial, W. D., Jackson, K., Zuteck, M., Miravete, A., Tsai, S. W., and Richmond, J. L., "Trends in the design, manufacture and evaluation of wind turbine blades," *Wind Energy*, Vol. 6, pp. 245-259, 2003.

Veldkamp, D., "Chances in Wind Energy A Probabilistic Approach to Wind Turbine Fatigue Design," Ph.D. thesis, DUWIND Delft University Wind Energy Research Institute, 2006.

Wei, Z., and Forte, T. P., "Multi-axial fatigue life assessment of wind turbine structural components," *Proceedings of the ASME 2010 4th International Conference on Energy Sustainability ES2010*, Phoenix, Arizona, May 17-22, 2010.

Winterstein, S. R., and Veers, P. S., "A Numerical Analysis of the Fatigue and Reliability of Wind Turbine Components," SANDIA REPORT SAND94-2459, Sandia National Laboratories, Printed February 2000.

Wind Data from Anemometer Loan Programs, Wind Powering America. URL: http://apps2.eere.energy.gov/wind/windexchange/anemometerloans/

Wind Data from the UMass Wind Energy Center. URL: http://www.umass.edu/windenergy/resourcedata

Wind Data from IAWind and Iowa EPSCoR Data Download Site. URL: https://epscor2.cgrer.uiowa.edu/html/download.html

Zhao, L., Choi, K. K., and Lee, I., "Metamodeling Method Using Dynamic Kriging for Design Optimization," *AIAA Journal*, Vol. 49, No. 9, September 2011.